A FINITE ELEMENT NUMERICAL STUDY OF THE OCEAN CIRCULATION OFF THE NEWFOUNDLAND AND LABRADOR SHELF

ZHAOSHI LU

A finite element Numerical study of the ocean circulation off the Newfoundland and Labrador Shelf

by

©Zhaoshi Lu
B.Sc. (2003) Ocean University of China

A thesis submitted to the
School of Graduate Studies
in partial fulfillment of the
requirement for the degree of
Master of Science

Department of Physics and Physical Oceanography
Memorial University of Newfoundland
November 2008

St.John's Newfoundland

Contents

Abstract

QUODDY, a 3-D finite element numerical ocean model, is used to study the ocean circulation variability over the Labrador Shelf and Newfoundland Shelf, and the evolution patterns of the model temperature, salinity and currents. The effects of two different nudging schemes on the model solution are examined. One approach is to restore the model temperature and salinity toward their initial values (for the first M_2 cycle) or toward evolving immediately preceding M_2 cycle mean values (for the second and subsequent M_2 cycle). The other approach is to fix the density but allow dynamical evolution of temperature and salinity. The moored measurements are used to evaluate the model circulation results and harmonic tidal analysis is used to analyze the simulated tidal results. The model simulated circulations are generally consistent with observations. The current comparison statistics indicate good qualitative agreement and approximate quantitative agreement with moored measurements. The comparison of two different schemes shows that the nudging approach of T/S is conceptually and dynamically more realistic than the pure diagnostic one. Tidal model results are consistent with those from previous studies.

Acknowledgements

I would like to thank my supervisors, Dr. Guoqi Han and Dr. Brad de Young, for their guidance and support throughout the writing of this thesis and during my Masters program. The School of Graduate Studies and Department of Physics and Physical Oceanography in Memorial University also made helpful contributions.

Thanks also go to Chris Stevenson for the continuous computer support and assistance. Also thanks to my fellow graduate students, Charlie, Dave, Grieg, Ming, and many others.

Finally I would like to thank my wife, Shanshan Liu, for her accompanying, support and helping throughout this degree program and always.

List of Tables

List of Figures

Chapter 1

Introduction

The Labrador Current off Labrador and Newfoundland is a southward flowing component of the North Atlantic subpolar gyre (Figure 1.1). It carries cold fresh polar water, sea ice, and icebergs along the Labrador and Newfoundland Shelf to the Grand Banks region, playing a key role in the heat and freshwater balance of the North Atlantic [*Lazier and Wright*, 1993]. The oceanographic climate on the continental shelf off eastern Newfoundland and Labrador is strongly influenced by the Labrador Current. Since the pioneering work by the International Ice Patrol [*Smith, et al.*, 1937], numerous studies on the Labrador Current system have been carried out [*Greenberg and Petrie*, 1988; *Lazier and Wright*, 1993; *Petrie and Anderson*, 1983].

1.1 Labrador Current system

1.1.1 Circulation

Originating at the Davis Strait, the equatorward flowing Labrador Current moves southeastward from Hudson Strait (60°N), along the continental slope off Labrador and Newfoundland to the Tail of the Grand Banks (43°N) [*Smith, et al.*, 1937]. The "traditional" Labrador Current [*Lazier and Wright*, 1993] is concentrated over the break and upper slope of the Labrador Shelf but has a small branch on the inner shelf [*Smith, et al.*, 1937], called the inshore branch of the Labrador Current. An additional current regime in the deep water was also reported by Lazier and Wright and this deep Labrador Current is strongly barotropic [*Lazier and Wright*, 1993]. Most of the inshore Labrador Current flows onto the northeast Newfoundland Shelf with a small net inflow into the Gulf of St. Lawrence through the Strait of Belle Isle [*Colboume, et al.*, 1997]. The speed of the shelf edge branch of Labrador Current is about 0.3-0.5 m/s [*Greenberg and Petrie*, 1988; *Reynaud, et al.*, 1995], while the inshore currents are up to 0.2 m/s [*Colboume, et al.*, 1997; *Lazier and Wright*, 1993; *Smith, et al.*, 1937]. In general, the inshore branch is not well defined but appears as a broad weak flow. The inshore branch is an obvious coastal jet only in the places where the bathymetric effects intensify the currents, such as Bonavista Saddle and Avalon Channel. The offshore branch is warmer, deeper and more rapid than the inshore one. Interannual changes of the offshore branch are common and associated with variations in the West Greenland Current [*Heywood, et al.*, 1994].

Further south, near the northern Grand Bank, the current is divided into three branches:

a coastal branch, which is broader and less defined, flows through the Avalon Channel around the Avalon Peninsula and then flows westward along the Newfoundland south coast [Petrie and Anderson, 1983]; an offshore branch, which is the major portion of the current, follows the shelf break through Flemish Pass; and a small eastern branch clockwise passes around the Flemish Cap. The splitting of the Labrador Current around the Flemish Cap can be investigated by the satellite tracked drifters [*Lazier and Wright*, 1993; *Petrie and Anderson*, 1983]. Around the Flemish Cap, the Labrador Current narrows to 50 km with a speed of 0.25 m/s [*Petrie and Anderson*, 1983].

Off the southern Grand Bank, some part of the Labrador Current turns offshore along the southern Newfoundland Shelf break and then enters the Newfoundland Basin, some flows around the tail of the Grand Bank and then westward along the continental slope, interacting with the Gulf Stream [*Loder, et al.*, 1998].Those Arctic waters conveyed by Labrador Current can be traced as far south as the Middle Atlantic Ridge.

Lazier and Wright (1993) found the currents shoreward of the 3000-m isobath produced a 11 Sv transport associated with the barotropic component, based on the long-term current meter and CTD data across Hamilton Bank. Lazier and Wright (1993) also estimated that the annual variation of the currents over the upper slope has an annual cycle with a range of about 4 Sv.

1.1.2 Seasonal Variation

Although Smith *et al.* (1937) found no evidence for a systematic variation of the geostrophic transport, the seasonality of the Labrador Current system over the Newfoundland and Labrador Shelf has been studied with the use of observations and numerical models. Estimates from monthly winds and the topographic Sverdrup relationship [*Gill and Niiler*, 1973], suggest a seasonal transport variation range of 7 Sv from the coast to the 3000-m isobaths, with a maximum in February and a minimum in July and November [*Thompson, et al.*, 1986]. A seasonal cycle of 5 Sv in the total Labrador Current transport, with a maximum in January and a minimum in July, was obtained from a wind-driven North Atlantic model and very little of the seasonal cycle in the current is directly affected by local or remote wind forcing [*Greatbach and Goulding*, 1989]. Based on the CTD section at Hamilton Bank, Lazier and Wright (1993) reported that the velocity at 400m and 200 m varies by the factor of 2 and 3, respectively, with minima in March- April and maxima in October. A seasonal range of 5 Sv form 300-m to 1400-m isobath and 10 Sv from 300-m to 3600-m on the Hamilton Bank track near the Seal Island transect was estimated using altimetry and hydrography [*Han and Tang*, 1999]. Rather than wind forcing, the seasonal variation was due to the buoyancy forcing [*Greatbach and Goulding*, 1989; *Thompson, et al.*, 1986]. However, a recent high-resolution modeling study indicated the large-scale wind forcing had a significant impact on the shelf-edge Labrador Current [Han, 2005]. The seasonal cycle dominates shelf water

characteristics of this area, partly because of the formation and advection of sea ice.

Strong seasonal variability has also been identified in both the salinity and temperature of this current, consistent with that of the buoyancy sources [Petrie and Anderson, 1983]. Both temperature and salinity in this area are affected significantly by the surface heating, ice melting and freshwater runoff.

Sea ice is significant to both the physics and biology of this area. Ice formation increases the salinity of seawater. Annual surface salinity has a minimum in the south occurring in late summer. Ocean circulation in this region will be influenced by these thermodynamic processes of freezing and melting. Much of the seasonal variation in the temperature can be explained by local forcing, however advection also plays an important role as demonstrated from 1-D modeling of temperature and salinity data from Station 27, just offshore St. John's [*Mathieu and deYoung*, 1995].

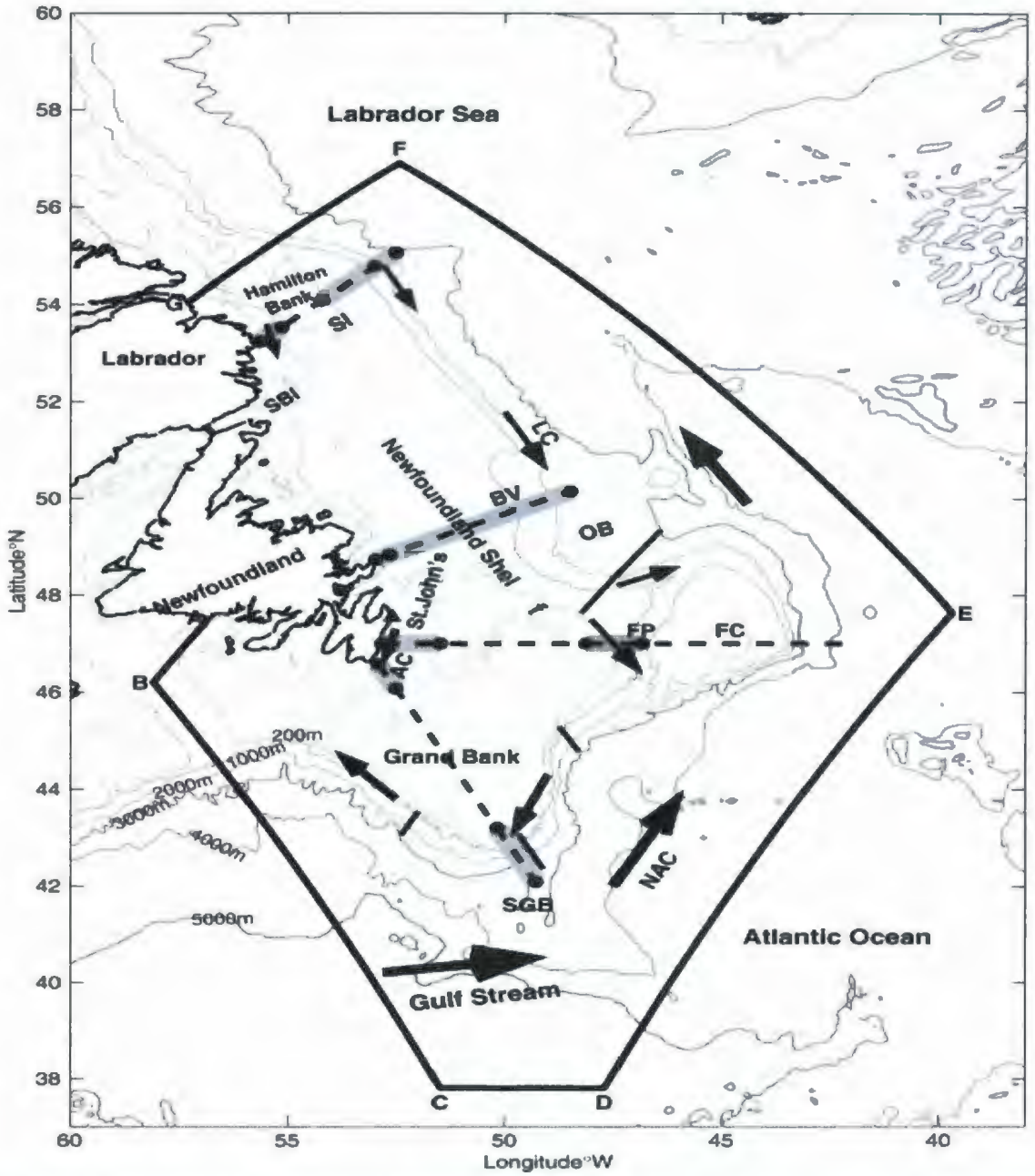

Figure 1.1: Map showing the Labrador and Newfoundland Shelf and adjacent NW Atlantic Ocean and the model open boundaries (thick solid lines). The isobaths displayed are 100, 200, 1000, 3000, 4000, and 5000 m. The Seal Island (SI), Bonavista (BV), Flemish Cap (FC) and Southeast Grand Bank (SGB) transects are shown as dashed lines (from north to south). The thick grey segments depict the nearshore and slope extents for the calculation of the volume transport. The four solid segments depict the width across which the Labrador Current transport was calculated from satellite altimetry data in Han and Li (2004). AC: Avalon Channel; FP: Flemish Pass; LC: the Labrador Current; NAC: the North Atlantic Current; OB: Orphan Basin; SBI: Strait of Belle Isle. The location of Station 27 is 8 km offshore of St. John's (solid triangle) [*Han*, 2005].

1.2 Research Objectives

Earlier model studies of circulation applied to this region were based on simpler dynamics and coarser resolutions. Greenberg and Petrie (1988) employed a barotropic, homogeneous model with additional inflows specified at the northern boundaries to represent remote barotropic forcing, and showed that ocean currents follow the bathymetry contours. Greatbatch *et al.* (1990) used a wind-driven North Atlantic model to study the seasonal sea level variation forced by the local and the North Atlantic wind forcing on the Newfoundland and Labrador Shelf. A linear, three-dimensional diagnostic model was employed to study the mean circulation of the Labrador Sea and the adjacent shelves, the summer circulation forced by a sea surface elevation applied on the northern boundary as well, and found that the transport of the Labrador Current are mainly determined from the density structure, topography, and boundary flows [*Tang*, 1996]. In addition, the Atlantic Zone Monitoring Program (AZMP) collects and analyzes biological, chemical, and physical data, both from *in situ* observation and remote sensing; and provides the multidisciplinary data sets to resolve the temporal and spatial variability of the Canadian Atlantic Ocean. The AZMP program provides environmental information along standard oceanographic transects and fixed stations across the entire Atlantic zone, providing important data for validating ocean models and improving models performance through

data assimilation.

To date, a density- and wind- driven circulation model, together with resolution sufficient to resolve the Labrador Current and large-scale North Atlantic forcing, has rarely been applied to this region. The main innovation of this work is the implementation of a high-resolution finite element circulation model that resolves the Labrador Current and accounts for the large-scale boundary forcing for the Newfoundland and Labrador Shelf to investigate seasonal wind-driven circulation. In this study, an attempt is made to improve the high-resolution 3D circulation/hydrographic fields associated with the M_2 tide in the region with new nudging schemes and better physics and also examine the effects of fixing the density field scheme and the nudging temperature and salinity method, with a particular focus on the latter. The simulated velocity, and transports at four selected standard transects (see Fig. 1.1 for locations) will be presented in Chapter 3.

The layout of this thesis is as follows: Chapter 2 presents the model, model setup and data used; Chapter 3 discusses the model simulated circulation, volume transport, and evaluate with moored current data; Chapter 4 deals with the evaluation of simulated circulation field against moored observation; Chapter 5 deals with the harmonic tidal analysis results of surface elevation and tidal current, and Chapter 6 has a brief summary and discussion on the result of this thesis.

Chapter 2

Methodology

2.1 Finite element ocean model description

The 3-D shelf circulation model QUODDY 4 [*Lynch and Werner*, 1991; *Lynch, et al.*, 1996] was used, which is a family of Fortran coded 3-D finite-element numerical model described in detail by Lynch and Werner (1991) and Lynch *et al.* (1996). Based on the linearized diagnostic harmonic models, this model has fully nonlinear hydrodynamics in the time domain and advanced turbulence closure. Using unstructured meshes of linear triangles in the horizontal and structured meshes in the vertical, both variable horizontal and vertical resolution can be facilitated (Figure 2.1).

To apply the finite element method, the study domain is divided into triangular, rather than square, computational elements. A 3-D mesh is constructed by QUODDY from the horizontal grid provided by the user. The mesh basically consists of a 2-dimensional horizontal mesh of triangles (Figure 2.2) and a 1-dimensional vertical mesh discretized into the same number of levels at each horizontal node. The grid is terrain-following with the lower level at the bottom and the upper level following the sea surface. The horizontal

mesh is projected downward to the bottom in vertical lines, and each line is discretized into the same number of vertical elements. These are then connected in the identical topology as the original 2-D mesh horizontally and the volume is filled with 6-node linear elements of prismatic shape.

The finite difference approach is easy to apply, but lacks resolution adaptability and geometrical flexibility. For ocean models with terrain following coordinates (σ-coordinates), it is preferable to maintain high spatial resolution on the steep bottom topography. If the grid size is constant and the resolution is high everywhere, it will cause unnecessary computation where the resolution is higher than necessary. For a variable grid size with finite element method, small triangles are used where a lot of detail is needed to achieve high local resolution and big ones where less is needed to maintain wide geographic coverage. Using the finite element method is efficient to represent the coasts smoothly.

The model uses the Reynolds-averaged, Navier-Stokes equations for an incompressible, hydrostatic fluid, making the Boussinesq approximation, and driven by rotation, wind, tide, and barotropic and baroclinic pressure gradients.

The Navier-Stokes equation is solved for the horizontal part of the velocity (momentum) and is expressed as:

$$\frac{d\vec{v}}{dt} + \vec{f} \times \vec{v} = -g\nabla_{xy}\zeta - \frac{g}{\rho_0}\int_z^{\zeta} \nabla_{xy}\rho dz + \nabla_{xy}(A_h \nabla_{xy} \cdot \vec{v}) + \frac{\partial}{\partial z}(N_m \frac{\partial \vec{v}}{\partial z}) \qquad 2.1$$

Where $\vec{v}$ is the velocity, $\vec{f}$ is the Coriolis parameter written as a vector pointing

upward, g is the gravity, ζ is the sea surface elevation, ρ is the density, A_h is the horizontal eddy viscosity coefficient, and N_m is the vertical turbulent mixing coefficient. ∇ is the gradient operator, ∇_{xy} is its horizontal part.

The free surface is calculated by depth integrating the continuity equation

$$\frac{\partial \zeta}{\partial t} + \frac{\partial}{\partial x}\int_h^{\varsigma} u dz + \frac{\partial}{\partial y}\int_h^{\varsigma} v dz = 0 \qquad 2.2$$

The vertical velocity is computed in terms of horizontal velocity using the continuity equation

$$\frac{\partial w}{\partial z} = -\nabla_{xy} \cdot \vec{v} \qquad 2.3$$

The sea surface elevation and vertically integrated momentum equation are rearranged to obtain the shallow water wave equation as in Lynch and Werner (1991) and can preserve the gravity wave performance on the simple elements [Lynch and Gray, 1979].

$$\frac{\partial^2 \varsigma}{\partial t^2} + \tau_0 \frac{\partial \varsigma}{\partial t} - \nabla_{xy} \cdot \left\{ -v\big|_{z=\varsigma} \frac{\partial \varsigma}{\partial t} + \int_h^{\varsigma} \left[v \cdot \nabla v + \frac{g}{\rho_0} \int_z^{\varsigma} \nabla_{xy} \rho dz' - F_m \right] dz \right. \qquad 2.4$$
$$\left. + gH\nabla_{xy}\varsigma + f \times H\overline{v} - \tau_0 H\overline{v} - N_m \frac{\partial v}{\partial z}\big|_{z=\varsigma} + C_d |v_b| v_b \right\} = 0$$

where τ_0 is a numerical constant [*Kinnmark*, 1986], C_d is bottom stress coefficient, *Vb* is the bottom velocity, F_m is the non-advective horizontal exchange of momentum, H is the total fluid depth. The conservation of heat and salt conservation are applied in the original model.

An equation of state is needed to close the system of equations as in the models the salinity and the temperature are prognostic variable. The density is calculated as a function

of salinity and temperature according to the one atmosphere international equation of state of sea water [*UNESCO*, 1981].

In the vertical, the Mellor-Yamada level 2.5 turbulent closure scheme (MY25) [*Mellor and Yamada*, 1982] with CP88 improvements [*Blumberg and Galperin*, 1992] is employed and a linearized partial-slip condition is enforced at the bottom. In the horizontal, mixing is represented by Smagorinsky horizontal viscosity parameterization [*Smagorinsky*, 1963]. The minimum value of vertical eddy viscosity for momentum, vertical diffusivity for temperature, salinity and turbulent kinetic energy and mixing length scale were set to 0.0002 m^2/s.

The original horizontal coordinate system is Cartesian. The wind and bottom shear stresses are calculated in horizontal. A conventional quadratic slip condition relating the shear stress was applied to the bottom velocity at the bottom.

2.2 Model Setup

Figure2.2 shows the fixed horizontal computational mesh, which consists of 10927 variably spaced nodes [*Xu and Loder*, 2004]. In the horizontal, the node spacing is typically 5 km over the shelf, less than 1 km around the shelf edge and upper continental slope, and 10–20 km offshore. In the vertical, the mesh has 21 variably spaced nodes with

minimum spacing of 1 m near the sea surface and the seabed. The Southern Labrador Shelf (SLS), the Newfoundland Shelf, and adjacent deep oceans were covered in the mesh, with high resolution in shallow areas and those with small topographic length scale ($h/|\nabla h|$ where h is the local water depth). The mesh has the ability to have a varying resolution, high resolution in areas of interest, both necessary for good model results, and coarse resolution in deeper water to avoid unnecessary computations. It is preferable to have high resolution in areas of steep bottom slopes due to topographic steering of barotropic currents and therefore high resolution was applied at the shelf break and over the continental slope. As well, the resolution depends on the bathymetry with high resolution near coast region to decrease the error sources near this boundary and coarse resolution in deeper water to achieve a better use of the time step.

The topography used in the model (Figure 2.2) comes from two resources: the shelf part from a database with a 7-km resolution archived at the Canadian Hydrographic Service and the deep oceans part comes from the ETOPO5 bathymetry database [*NGDC*, 1988] which has a global coverage of 5 x 5 minutes. The minimum depth in the model domain was set at 10 m.

2.3 Model forcing data, open boundary conditions

The regional wind forcing specified in the model runs are the spatially varying wind stresses computed from 6-hourly wind data of NCEP–NCAR reanalysis data from 1990 to 1999 and averaged by month for the period. NCEP–NCAR wind speed were found to be less than high-quality research vessel observations in all the latitude bands ([*Smith, et al.*, 2001]). Seasonal variations in both magnitude and direction are found in monthly mean wind stresses, e.g., with the stress in December being stronger and directed more in the cross-shelf direction (offshore) than that in July. The typical mean of the wind stresses used in the model domain is 0.1 Pa in December and 0.02 Pa in July. The model is forced with monthly-mean steric height and wind-induced sea level, monthly-mean temperature and salinity climatology on the open boundary.

An additional open-boundary inflow was applied on the northern boundary estimated from observation of sensity. The additional inflow was calculated based on observational estimates of the Labrador Current transport and assuming a geotropic balance. We linearly distribute an additional transport of 7.5 Sv across the continental slope segment (from the 500-m isobath 140 km away from the coast to the 2400-m isobath) and 52.5 Sv across the deep-ocean segment from the 3000-m isobath to the location F (see Fig 1.1 for location). The additional inflows were linearly distributed for easy applying purpose. The additional open-boundary inflow along the northern boundary was also applied in Tang's (1996) model simulation studying the circulation of Labrador Current.

The determination of the open boundary conditions is discussed and justified in Han *et*

al. (2008). To represent the influence of the wind forcing in the North Atlantic, elevations data from a wind-driven barotropic North Atlantic model [Han, 2005] are specified on all the regional open boundaries (Figure 2.3), except that geostrophy is applied on the Strait of Belle Isle boundary. Temperature and salinity at the open boundary were fixed to the climatological values interpolated from Geshlin *et al.* (1999). Figure 2.4 shows surface temperature and salinity at the boundary of several selected months. The remote forcing is obtained from a North Atlantic model with the same model dynamics and the same frictional parameters driven by the concurrent NCEP–NCAR wind stresses for the entire North Atlantic. The grid and bathymetry of this North Atlantic model are the same as Greenberg *et al* (1998). Significant seasonal variability in the sea surface slope on the northern boundary FG (see Figure. 1.1 for location) can be found. On the northern boundary FG, the sea surface slope toward the coast is much larger in November than in July (Figure 2.3). The total wind-driven circulation field is the sum of the regional and remote forced solutions.

The model is also forced by M_2 tidal elevation applied at the open boundary (Figure 2.5), unless specified otherwise. The tidal elevation data were derived from satellite altimetry and tidal-gauge data.

Monthly mean wind stresses are specified on the surface. On the land boundaries, the condition of no normal depth-integrated flow is implemented, and zero normal gradients of temperature and salinity are enforced at the lateral land boundaries as well.

2.4 Solution procedures

The climatologically monthly-mean temperature and salinity fields are used as initial condition. Initial condition also contains sea level and currents from diagnostic linear FUNDY5 solutions forced by the same NCEP/NCAR wind, density taken from Geshelin *et al.* (1999), and M_2 tide.

The time step was set to 43.66 s, so there were 1024 time steps for each M_2 tidal cycle simulation.

To improve the model result and obtain 3-D observationally based and dynamically consistent climatologically monthly-mean circulation fields, two methods are applied in the model: (1) nudging the temperature and salinity and (2) fixing the density field. All schemes allow for a spatially variable Coriolis parameter unless otherwise specified. In the following chapters of results and evaluation, we will focus on the solution of the T/S nudging scheme, but some results of the solution in which density is fixed will be shown as well.

The method of fixing density allows the dynamical evolution of temperature and salinity, but keeps the density field to the initial climatology. The method of restoring the temperature/salinity (density) fileds is similar to the semi-prognostic method suggested by

others to reduce the systematic model errors [*Greenberg*, 2004].

Equation 2.5 is the nudging scheme used in the model.

$$\varphi = \gamma * \overline{\varphi} + (1 - \gamma) * \varphi^{n} \qquad (2.5),$$

where φ is temperature or salinity, n is the number of time step, γ linearly decreases from 1 to 0 during each M_2 cycle, $\overline{\varphi}$ is the average during the preceding M_2 cycle, or the climatology for the first M_2 cycle. To restore the model result to the climatology, nudging is used during each M_2 tidal cycle (12.42 hours).

Although it may partially suppress the tidal evolution of the hydrographic field, the method of fixing the density field and restoring the temperature and salinity field to climatology can keep the model from drifting significantly away from the specified observationally based state (the diagnostic solution), but allows sufficient dynamical adjustment in the tidal time scale.

All of the monthly model runs were integrated for 60 simulation days, which is long enough to reach a dynamically equilibrium state. If not specified, all the circulation results in the paper are averaged over the M_2 tidal period.

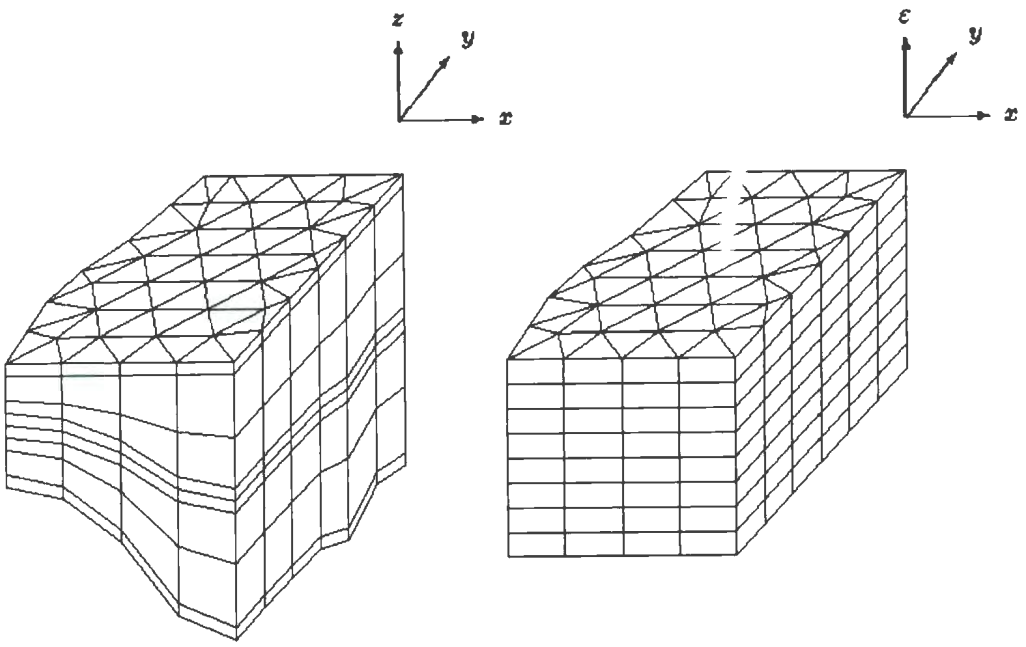

Figure 2.1: Main features of the 3-D layered mesh (this figure is adopted form Naime and Lynch, 1993): (1) element sides perfectly vertical, (2) variable vertical mesh spacing allows resolution of boundary and internal layers.

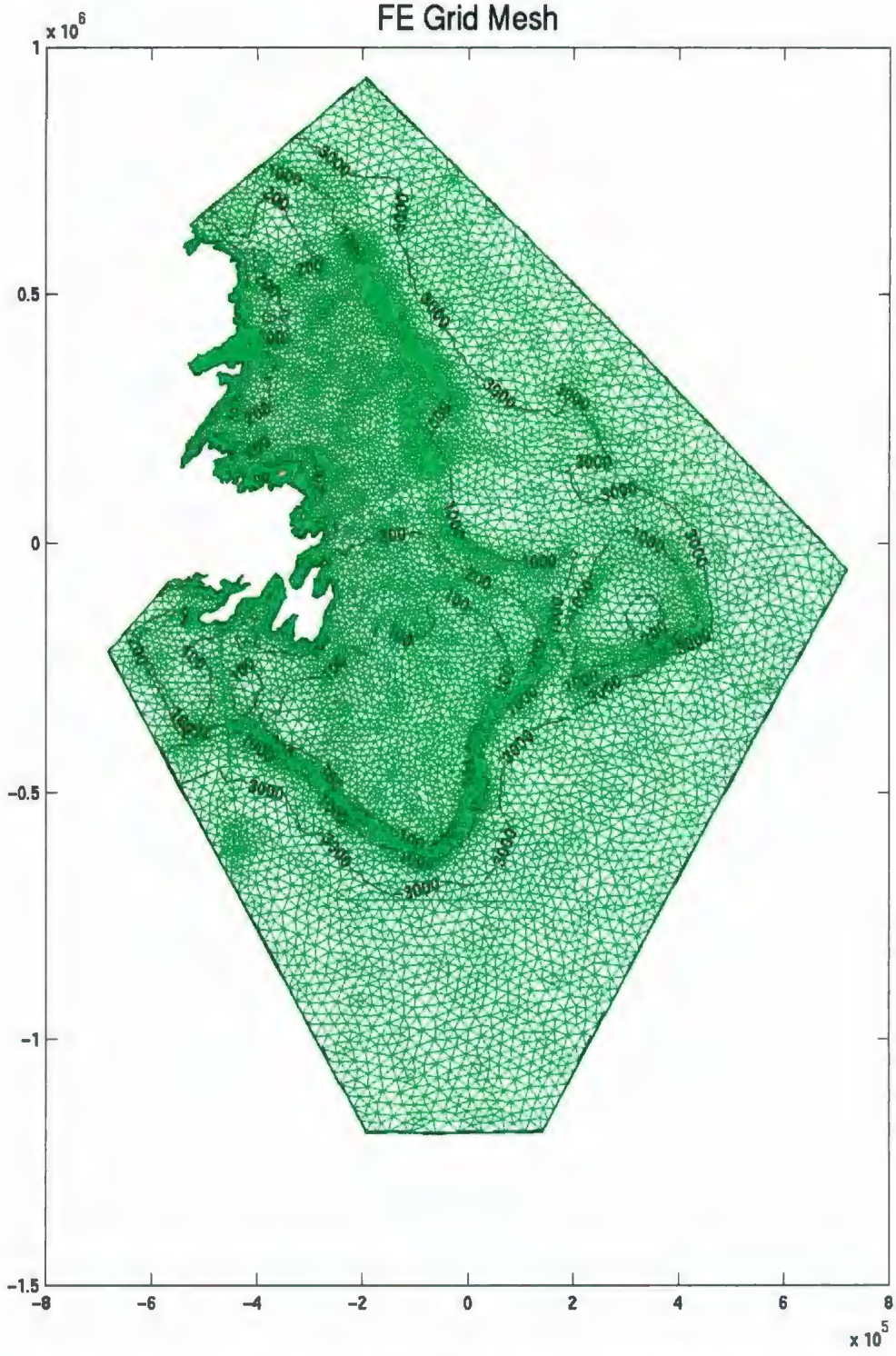

Figure 2.2: The horizontal finite-element grid (slns2) used in the numerical model. The depth contours are in meters

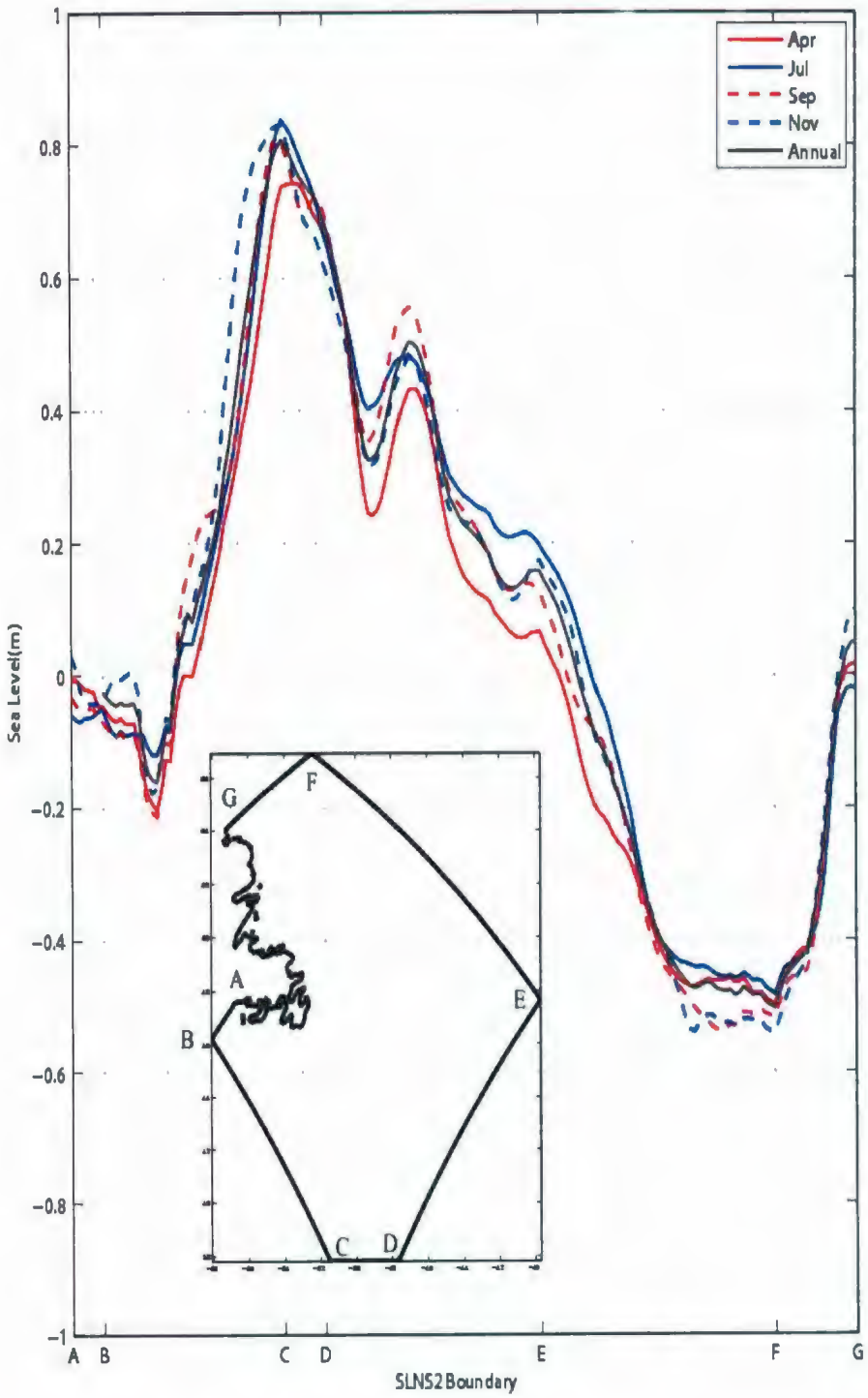

Figure 2.3: Sea level specified along the open boundary segments. Note that x axis is plotted against the node number, and is not at linear distance.

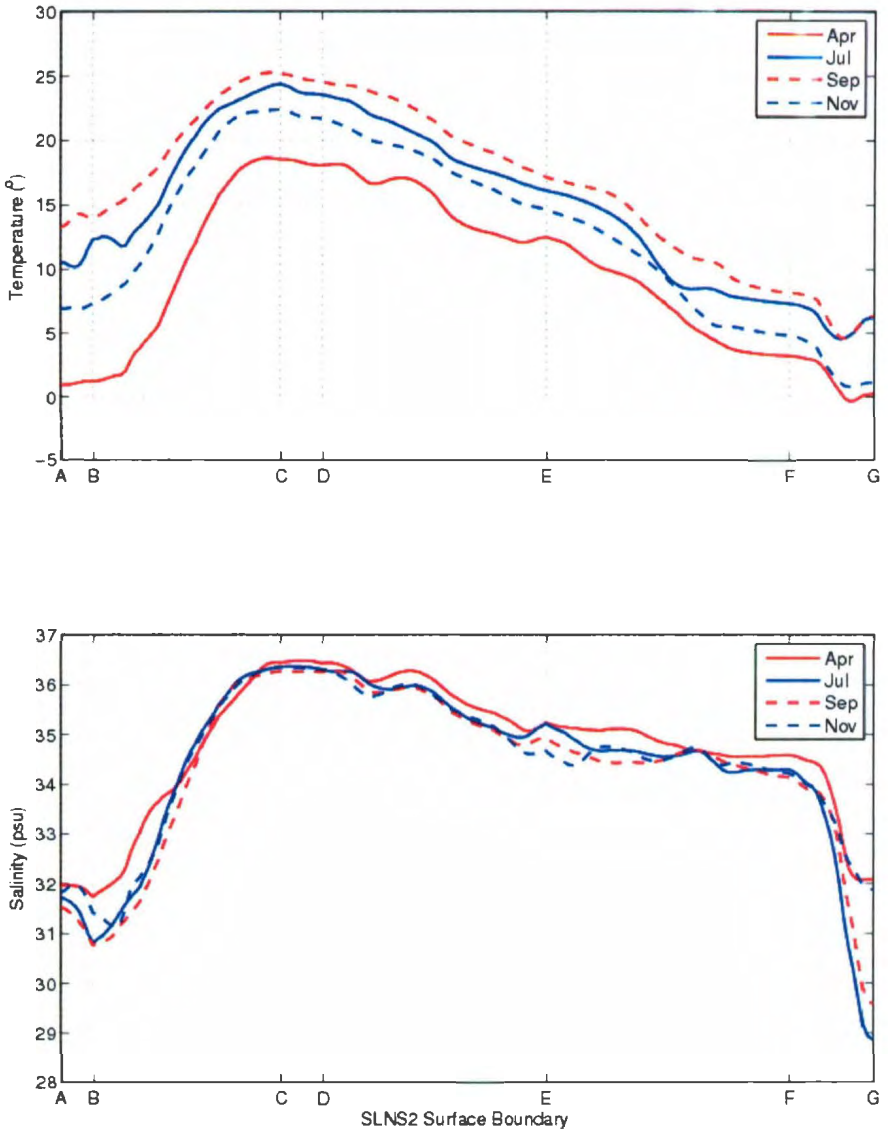

Figure 2.4: Surface temperature (upper panel) and salinity (bottom panel) specified along the open boundary segments. See Figure 1.1 or Figure 2.3 for locations of the boundary segments. Note that x axis is plotted against the node number, and is not at linear distance.

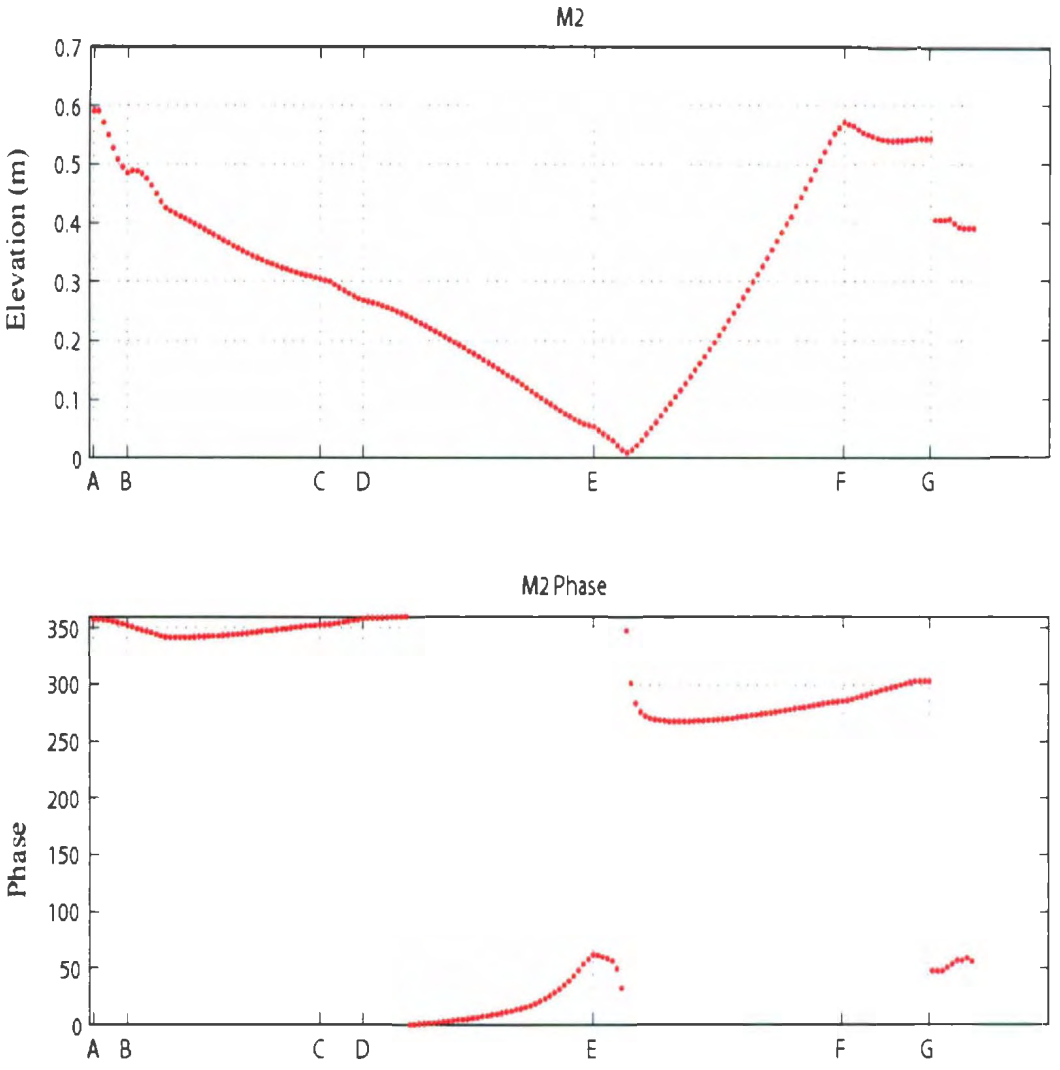

Figure 2.5: M_2 tidal forcing specified along the open boundary. See Figure 1.1 or Figure 2.3 for locations of the boundary segments. Note that x axis is plotted against the node number, and is not at linear distance.

Chapter 3

The simulated circulation

In this section, the 3-D structure of the monthly mean circulation with the T/S nudging for the Newfoundland and Labrador Shelf and Slope will be discussed with a focus on the nearshore and shelf-edge currents. Since the 3000-m isobath appears to be the boundary separating the equatorward shelf and slope current and the pole-ward deep currents, the present study will focus on the circulation inshore of the 3000-m isobath.

3.1 Monthly circulation

The modeled monthly mean velocity fields (Figure 3.1- Figure 3.8) show a representation of the strong and persistent equatorward current along the Newfoundland and Labrador shelf break and upper continental slope and the inshore current along the coastline. The model reproduces many well-known circulation features in the region with ocean currents generally following depth contour lines over the Labrador Shelf and Slope. The main branch of the Labrador Current follows the 400-1000m isobath with the greatest velocity from the north of the Hamilton Bank to the north of the Grand Bank, centered on the shelf

break. The weak inshore branch is developed just north of the Hamilton Bank and enters the domain close to the shore, and part of the eastward inshore branch rejoins the main branch at the northeast Grand Bank. The current diverges at the entrance to the Flemish Pass : one follows east around the northern Flemish Cap and the other flows southward through the Flemish Pass. The simulation also reproduces the relatively weak and spatially variable currents over the Grand Banks and the interaction of the Labrador Current and the Gulf Stream offshore of the Grand Bank. The overall circulation pattern is similar to that found in previous modeling studies [*Greenberg, et al.*, 1998; *Sheng and Thompson*, 1996]. Although not the focus of this paper, the Gulf Stream extension, the North Atlantic Current and the poleward current offshore of the 3000-m isobath off the south Labrador, and their seasonal variability, can be clearly found in all the simulations.

3.1.1 Monthly circulation at 30-m depth

From the model solutions at the 30-m depth (Figure 3.1-Figure 3.3), the dominant southward current along the Newfoundland and Labrador Shelf edge and the relative weak inshore branch of the Labrador Current are clearly presented, as described in detail by Han *et al.* (2008). In response to the effect of topography, the main branch of the Labrador Current basically follows the contour of depth and dominates from the model northern boundary to the southeast Grand Bank. The onshore steering of the shelf edge current is indicated south of the Hamilton Bank. The weak inshore branch is developed inshore of

the Hamilton Bank, continues along the southern Labrador and northeastern Newfoundland coast and rejoins the main branch at the northeast Grand Bank (at about 49°N). At the entrance to the Flemish Pass, the current splits into two branches: one flows southward though Flemish Pass and the other flows eastward around the northern Flemish Cap. Currents over the Flemish Cap and the Grand Bank are much smaller than the Labrador Current.

Significant seasonal variation is evident (Figure 3.1-3.4) in the model data. The predominant southeastward current is enhanced in fall/winter (e.g. Figure 3.1), slightly weakened in spring (Figure 3.2) and weakest in summer (Figure 3.3).

The shelf edge current is significantly reduced after passing the Flemish Pass. Much of its water mass is entrained into the northeastward flowing North Atlantic Current. The equatorward current along the southwest edge of the Grand Banks is much weaker year-round, and nearly disappears in July (Figure 3.3)

After passing through the Avalon Channel, a significant portion of the inshore Labrador Current moves offshore along a deep channel to join the much reduced shelf-edge Labrador Current. Substantial seasonal variations of the inshore branch through the Avalon Channel and the subsequent offshore cross-shelf flow are also found in the 30m results (Figure 3.4).

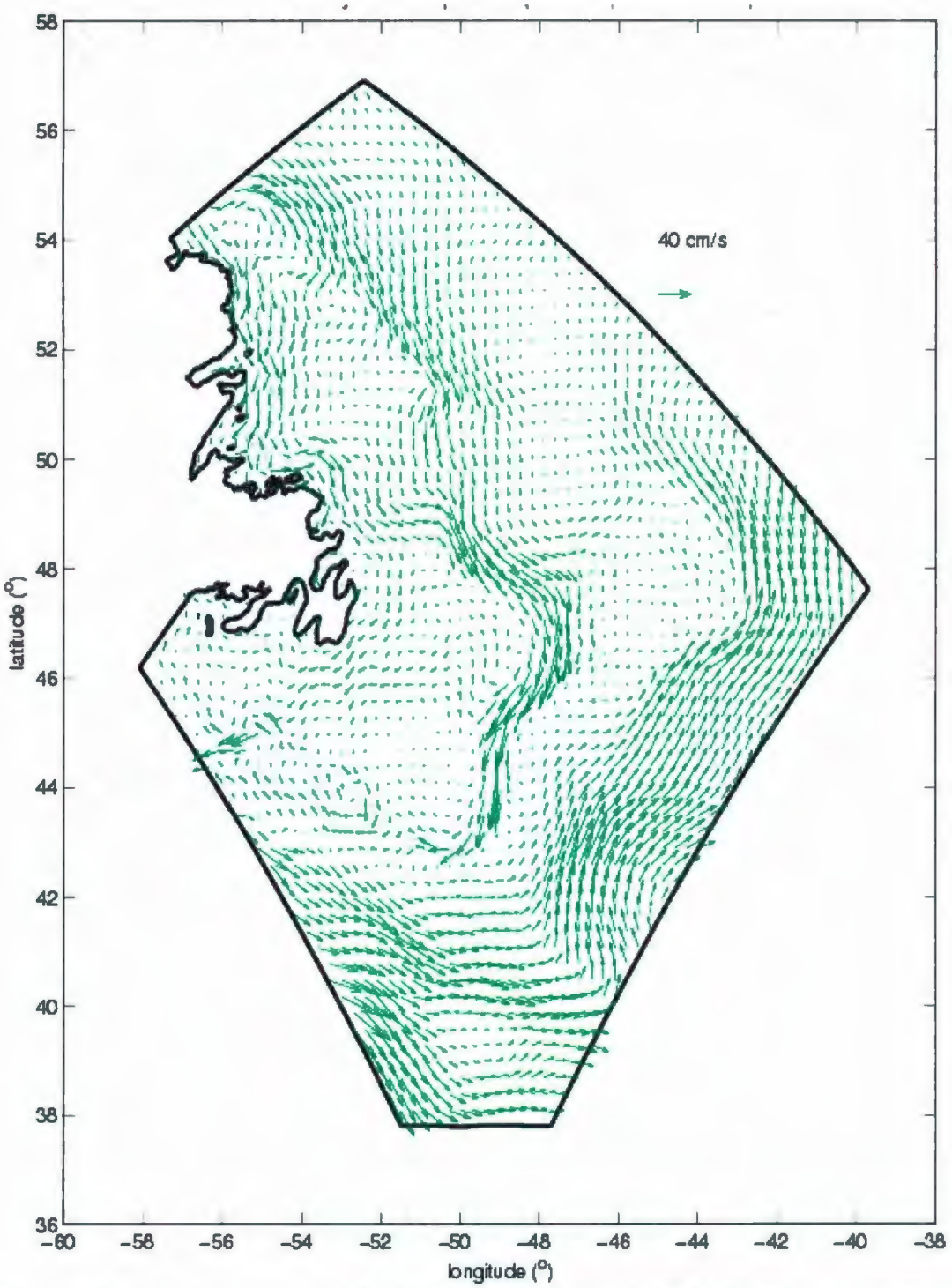

Figure 3.1 December current at the 30-m depth. The model field has been interpolated into regular grid for clarity.

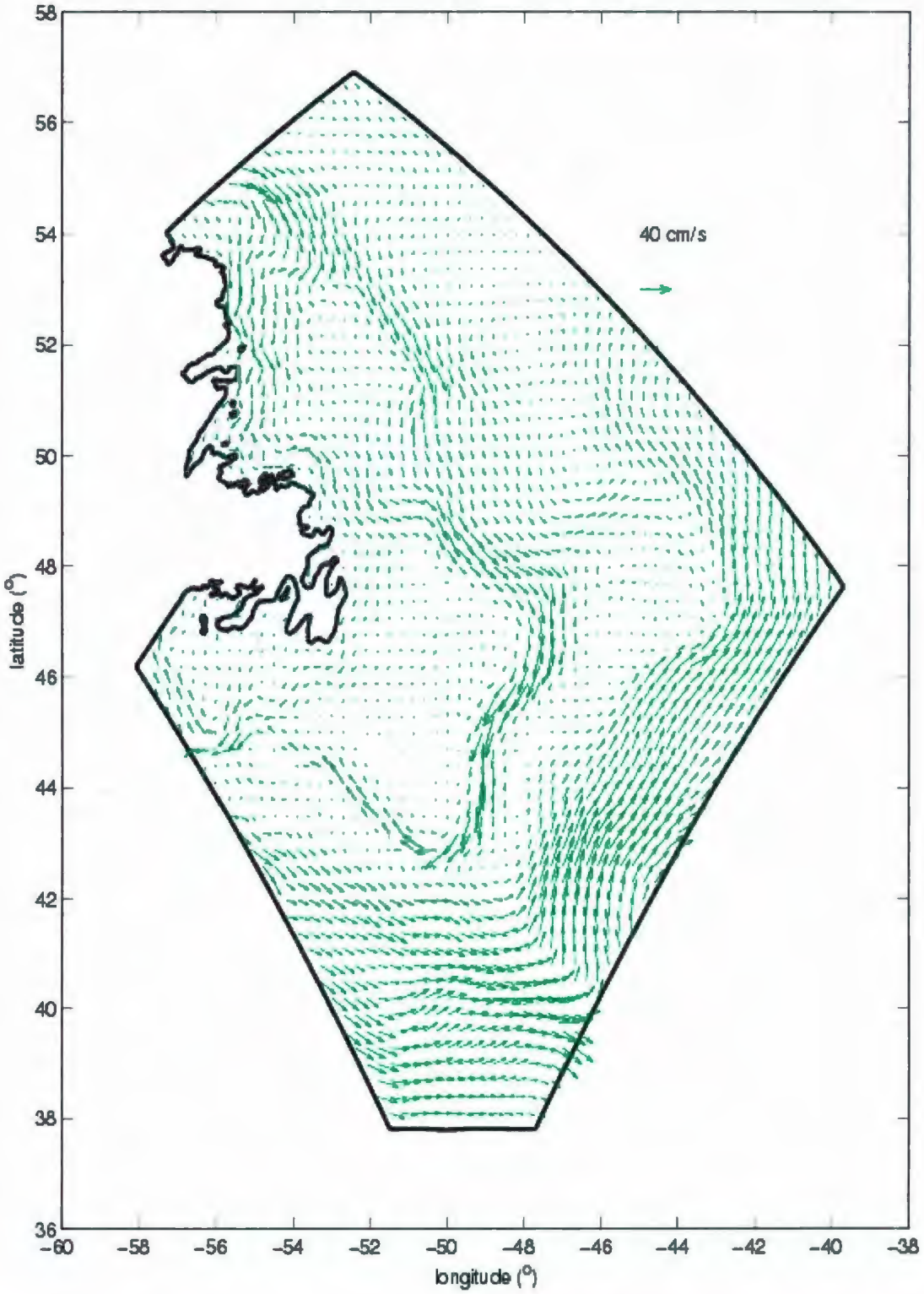

Figure 3.2 April current at the 30-m depth. The model field has been interpolated into a regular grid for clarity.

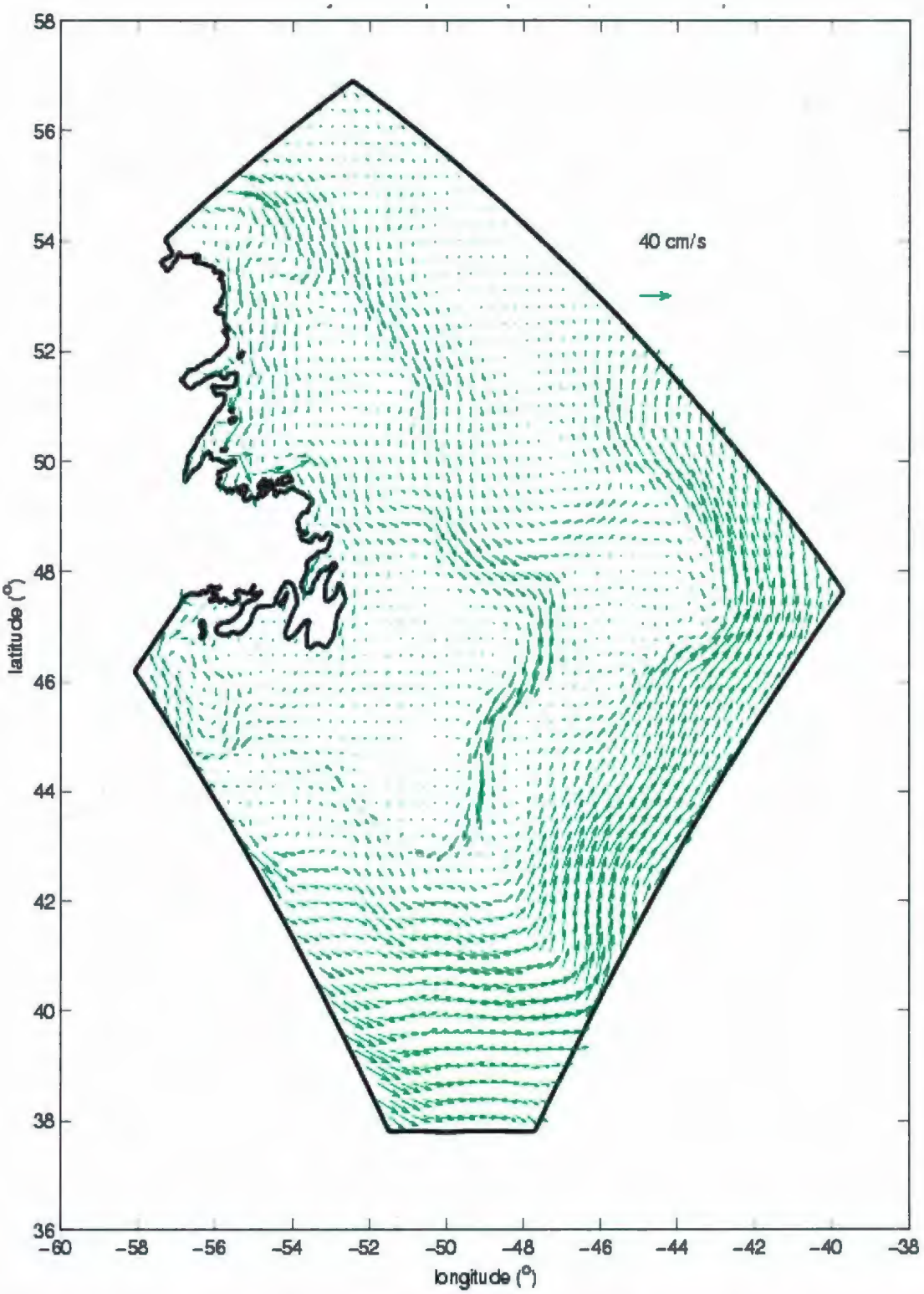

Figure 3.3 July current at the 30-m depth. The model field has been interpolated into regular grid for clarity.

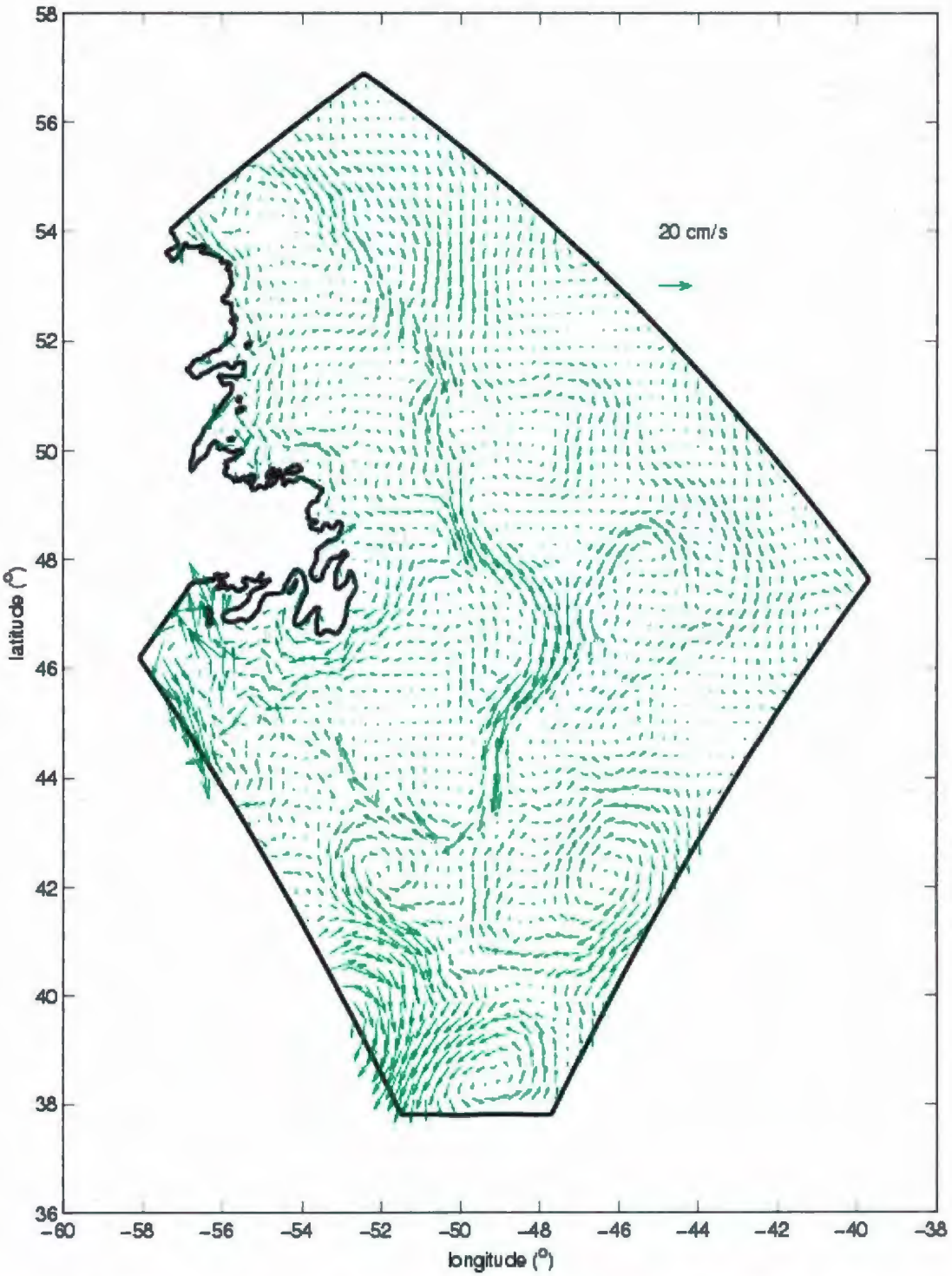

Figure 3.4 Difference between November and July circulation current at the 30-m depth. The model field has been interpolated into a regular grid for clarity. Note the scale is different from other figures.

3.1.2 Monthly circulation at the surface (1-m depth)

Compared to the solution at 30 m depth (Figures 3.1-Figures 3.3), the surface current at 1 m depth demonstrates stronger southeastward Ekman drift (Figures 3.5-Figures 3.7). The northwesterly wind induces a strong surface Ekman drift over the entire shelf and shelf break.

The typical magnitude of the wind stresses in the model domain is 0.1 Pa in December and 0.02 Pa in July. The model solutions indicate the significant influences of the wind-driven Ekman flow in the surface circulation (Fig. 3.5-3.7). In general the northwest/west winds in fall [Han, 2005] generate the surface Ekman current that reinforces the inshore and shelf-edge Labrador Current (Fig. 3.5). The southwest winds in summer generate the southeastward Ekman flow over the Grand Bank (Figure 3.7). Figure 3.8 shows the difference between December and July circulation at the 1-m depth, presenting an obvious winter enhancement in almost the whole model domain. The enhancement is attributed to both density and wind forcing.

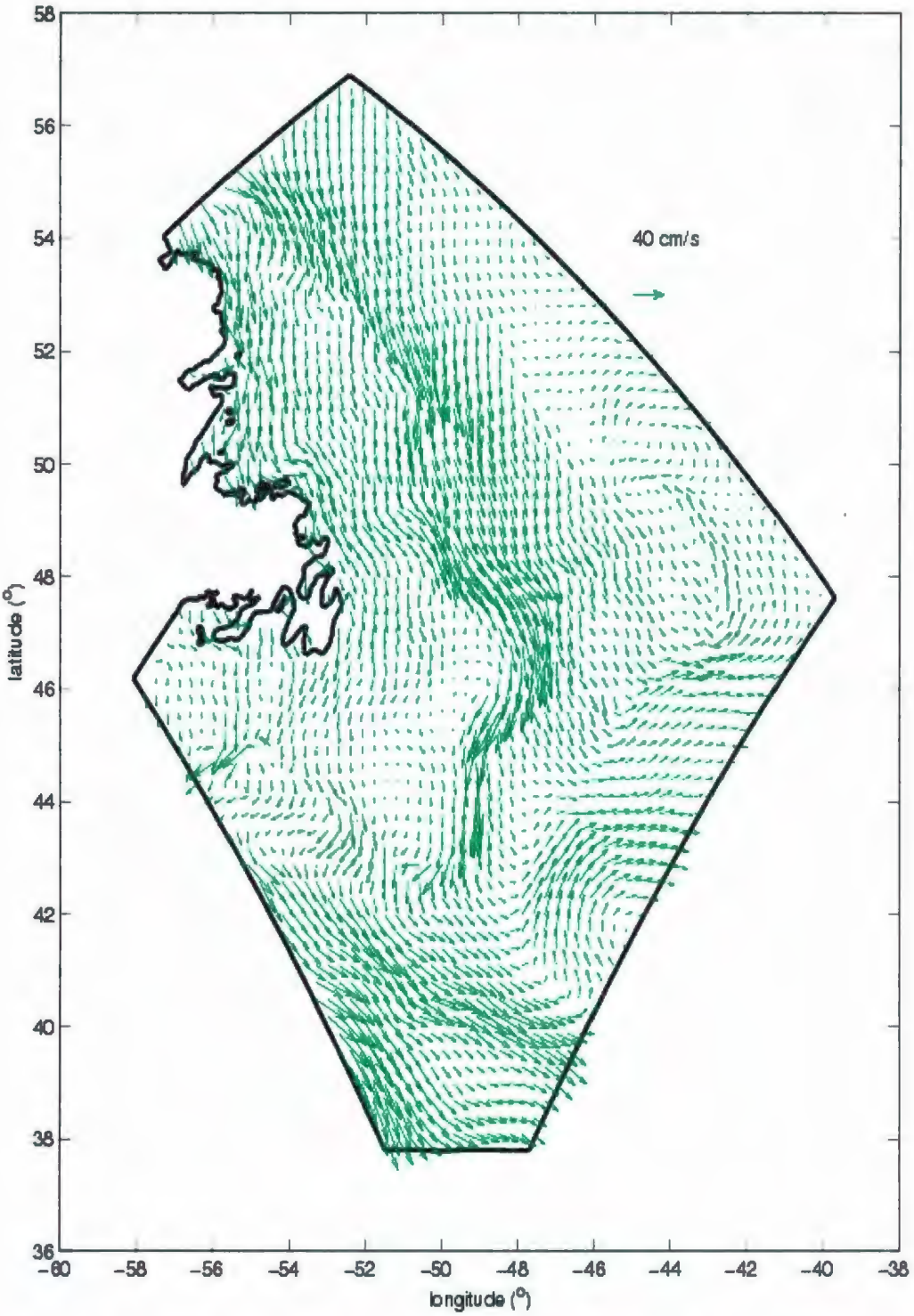

Figure 3.5 December current at 1-m depth. The model field has been interpolated into regular grid for clarity.

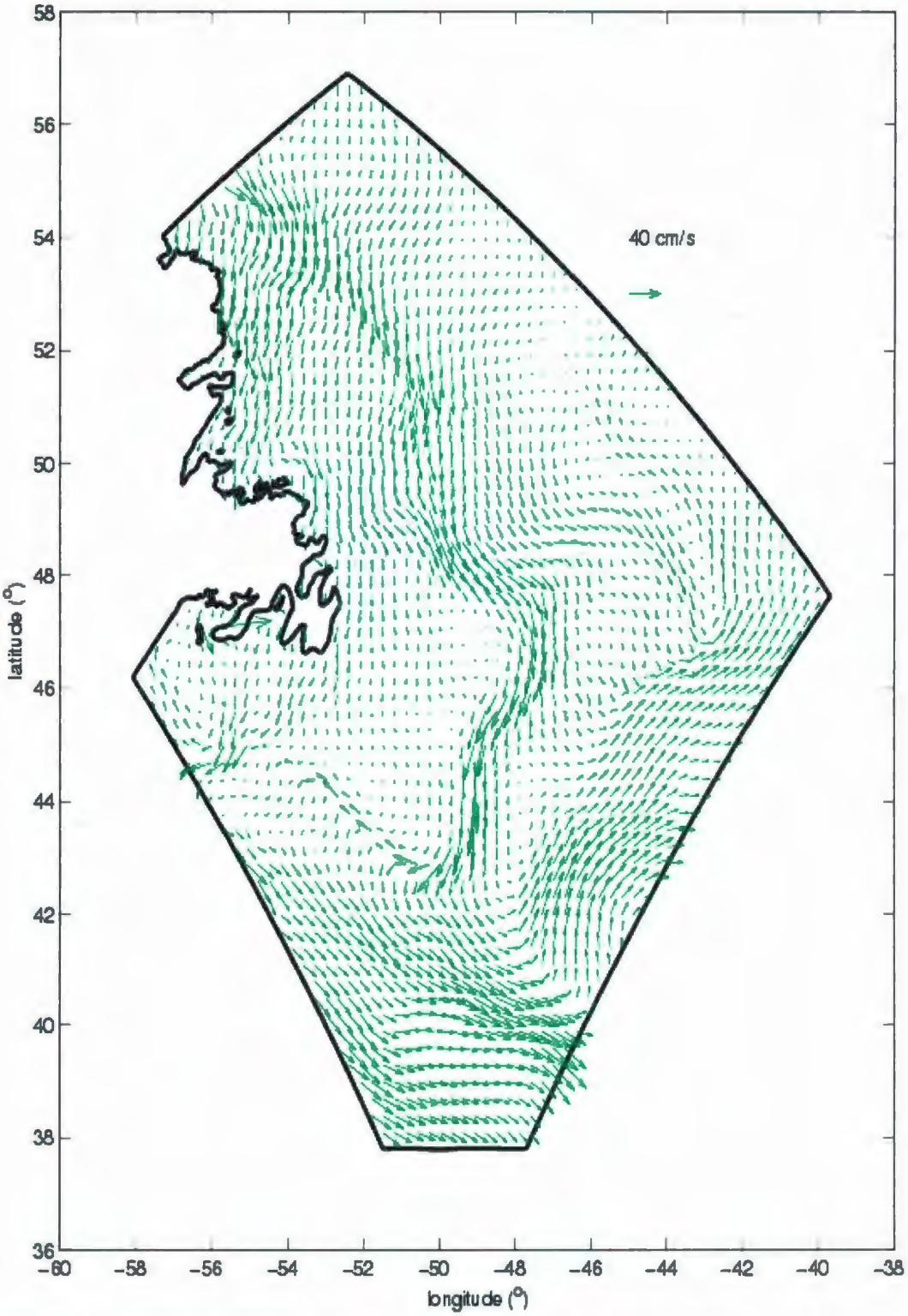

Figure 3.6 April current at the 1-m depth. The model field has been interpolated into a regular grid for clarity.

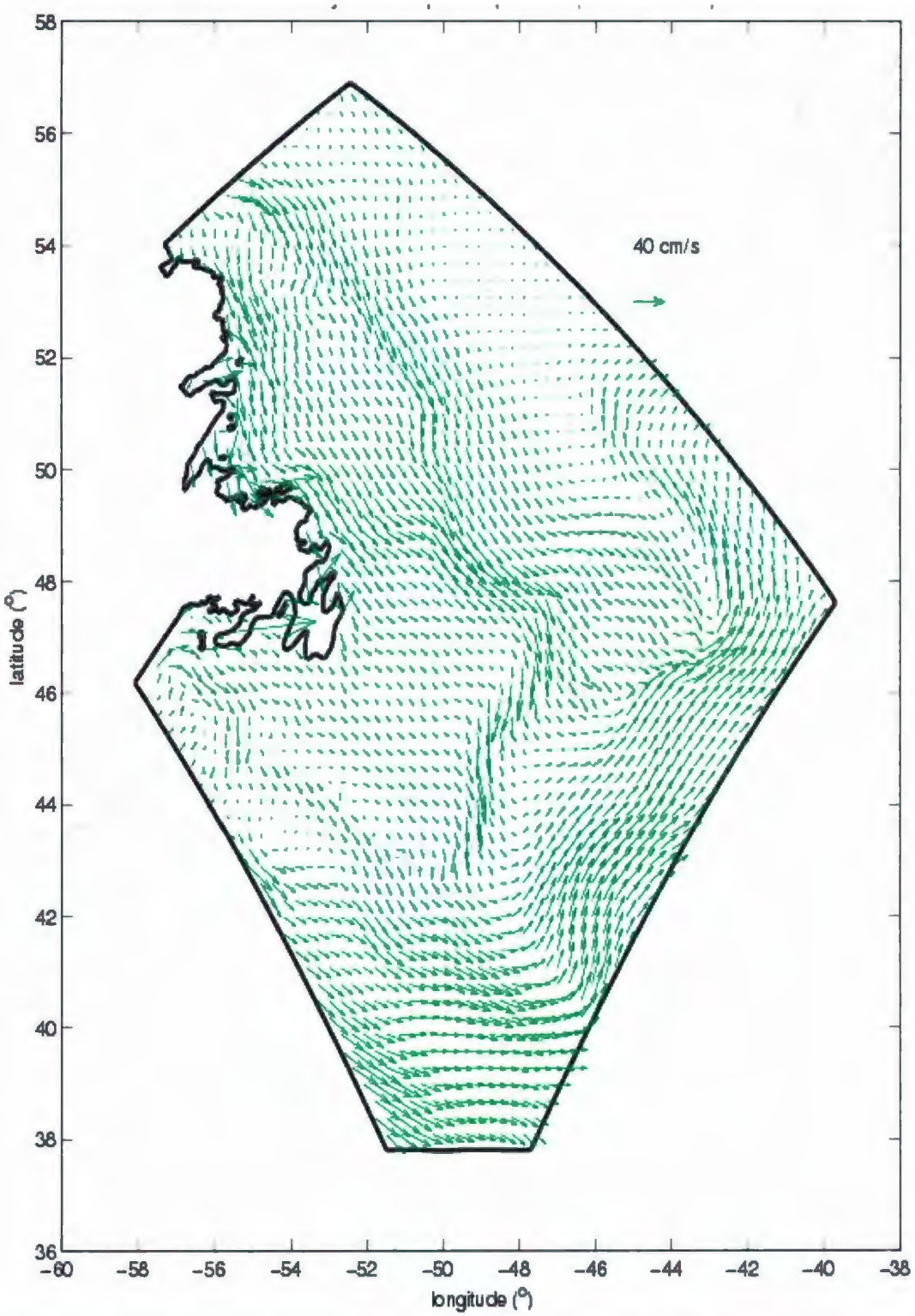

Figure 3.7 July current at the 1-m depth. The model field has been interpolated into a regular grid for clarity.

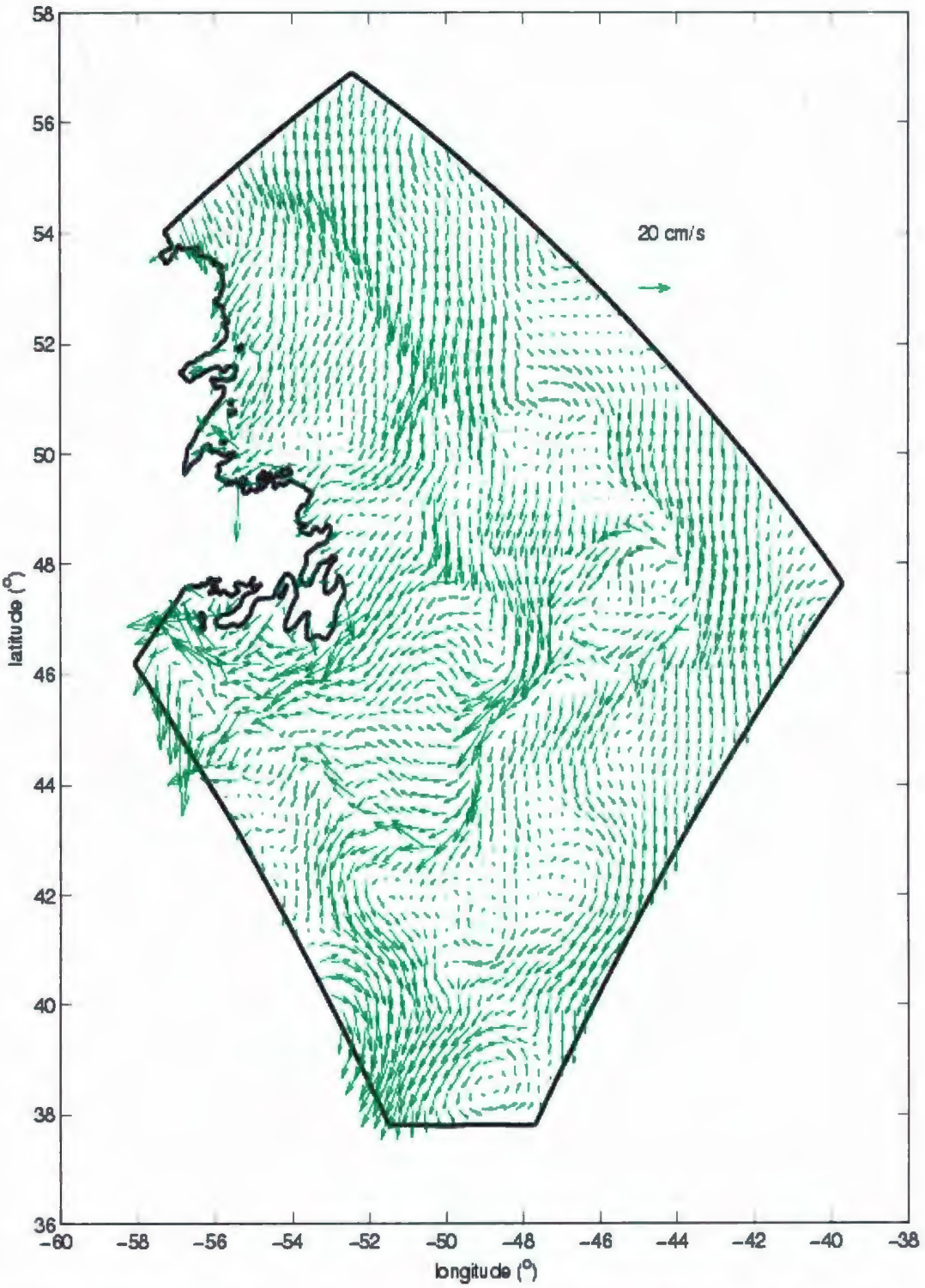

Figure 3.8 Differences between November and July circulation current at the 1-m depth. The model field has been interpolated into a regular grid for clarity. Note the scale is difference from other figures.

3.1.3 Vertical structure of velocity at the selected transects

The simulated currents for the Seal Island transect show the distinct inshore and offshore branches of the Labrador Current (Figure 3.9-3.10). The inshore branch is located within about 50 km from the shore. The offshore branch, which is typically less than 100 km wide, is centered at the shelf-edge and upper continental slope about 200 km offshore. The strong coastal jet off Labrador extends to the bottom (roughly 100–150 m depth). The speed of the inshore branch reaches about 0.40 m/s at the surface and 0.20 m/s near the bottom in November (Figure 3.9), in significant contrast to the current speed of about 0.15 m/s in summer (Figure 3.10). The shelf edge branch is centered along the 1000-m isobath and speeds range from 0.15 m/s at the 200-m depth to greater than 0.40 m/s at the centre of main Labrador Current. These model results are within the range of measurements collected from a long-term array and the hydrographic data of Lazier and Wright's (1993), which give a maximum surface current of 0.36±0.14 m/s at the 900-m isobaths and a coastal current of 0.13±0.14 m/s. Currents over Hamilton Bank are relatively weak. An onshore flow with a speed of over 0.10 m/s is evident in the surface layer.

Along the Bonavista transect, the cross-sectional distribution of the normal current is more uniform and generally reveals both an inshore branch and a relative strong offshore branch (Figure 3.11-3.12), however for some months (July for example) the current appears quite broad with no distinct separation between the inshore and offshore components. The speed of southward current in the upper 100-m of the water column

ranges from 0.05-0.15 m/s. A substantial flow is directed offshore and through the Bonavista Saddle combining with the offshore branch. The broader flow patterns are consistent with the significant cross-shelf component which is also indicated by tracks from the drifting buoys, current meter data and modeled results [*Han, et al.*, 2008; *Narayanan, et al.*, 1996].

The Labrador Current through the Flemish Pass is relatively strong in November (Figure 3.13), with a peak speed of 0.45 m/s at the surface, while the current is only 0.20 m/s in July (Figure 3.14). The southward current through Flemish Pass is concentrated near the east edge of the Grand Bank side as a bathymetrically trapped jet, an anticyclonic eddy is located over the Flemish Cap, and the North Atlantic Current flows northward east of the Cap. There is also a narrow coastal jet of over 0.10 m/s through Avalon Channel within 50 km of the coast. Currents over most of the Grand Bank are below 0.10 m/s in both November and July. The surface anticyclonic eddy over the Flemish Cap is intensified in November.

Along the Southeast Grand Bank transect, there is a narrow coastal jet with a speed of over 0.15m/s in the top 50 meter through Avalon Channel in November (Figure 3.15). The main path of the southward current is concentrated near the edge of the southeast Grand Bank with a maximum speed of 0.25 m/s at the surface.

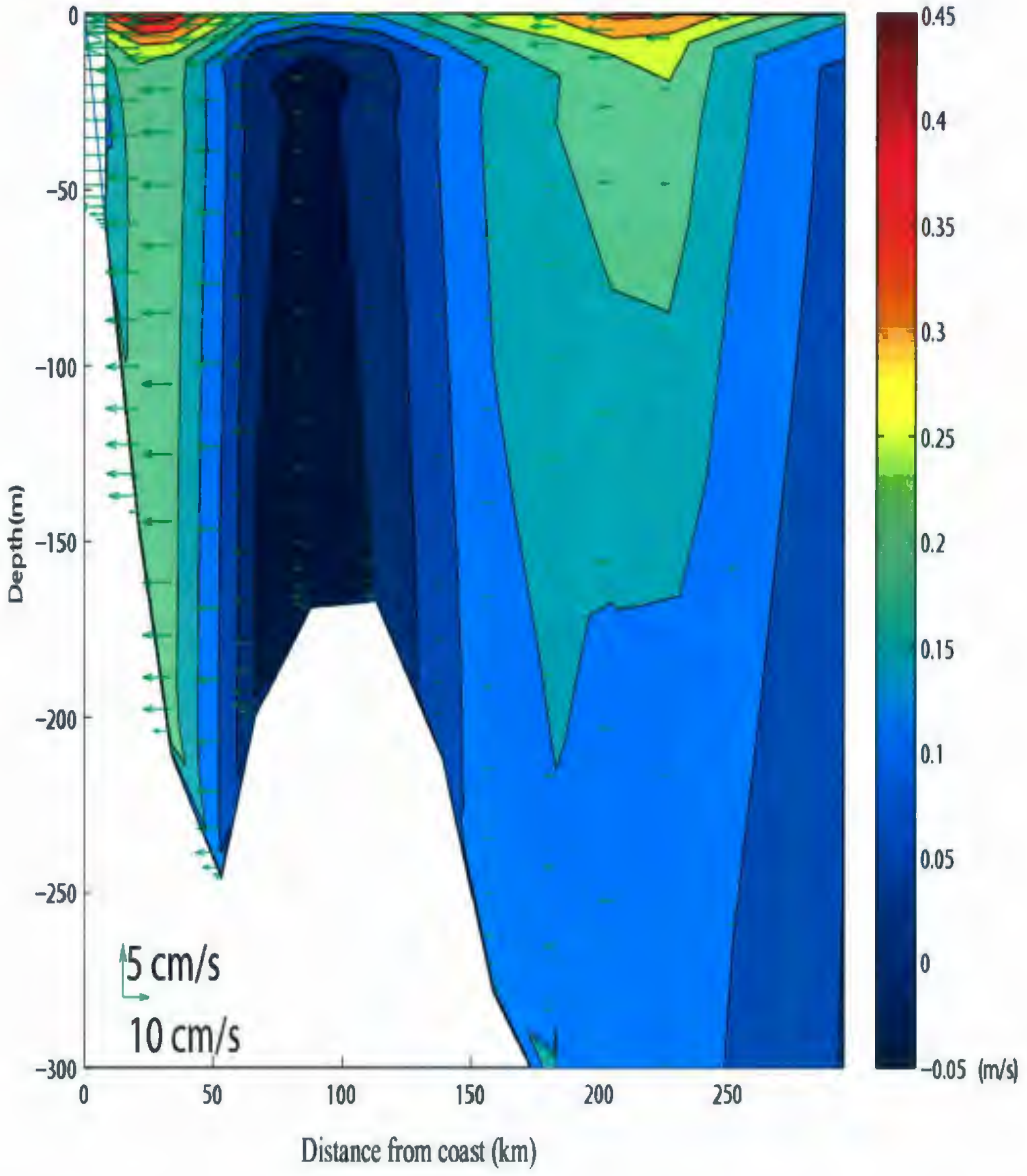

Figure 3.9: Velocity on the Seal Island transects in November from the model solutions. The color bands are for the normal currents (m/s), positive southward. The distance is measured from the coast.

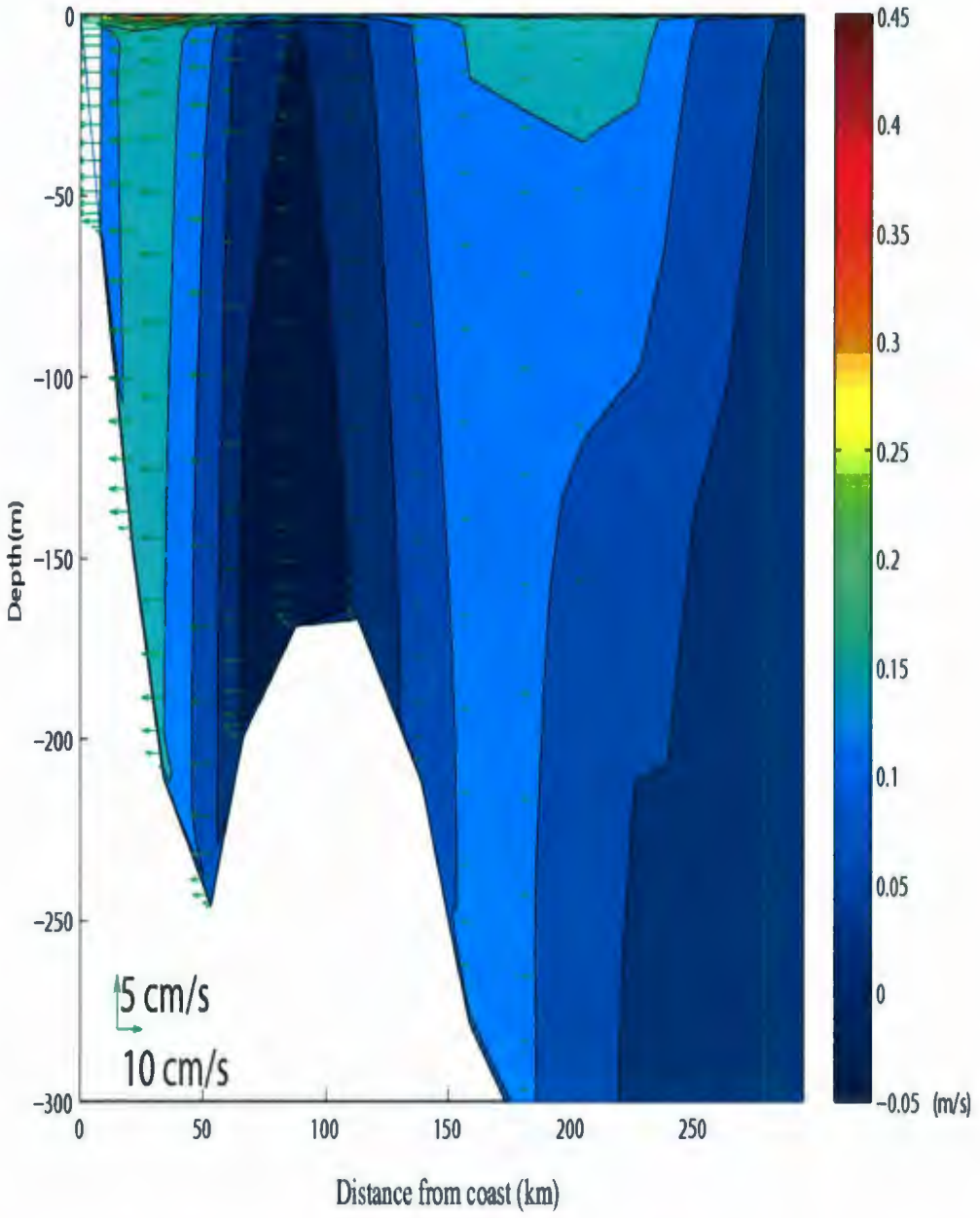

Figure 3.10: Velocity on the Seal Island transects in July from the model solutions. The color bands are for the normal currents (m/s), positive southward. The distance is measured from the coast.

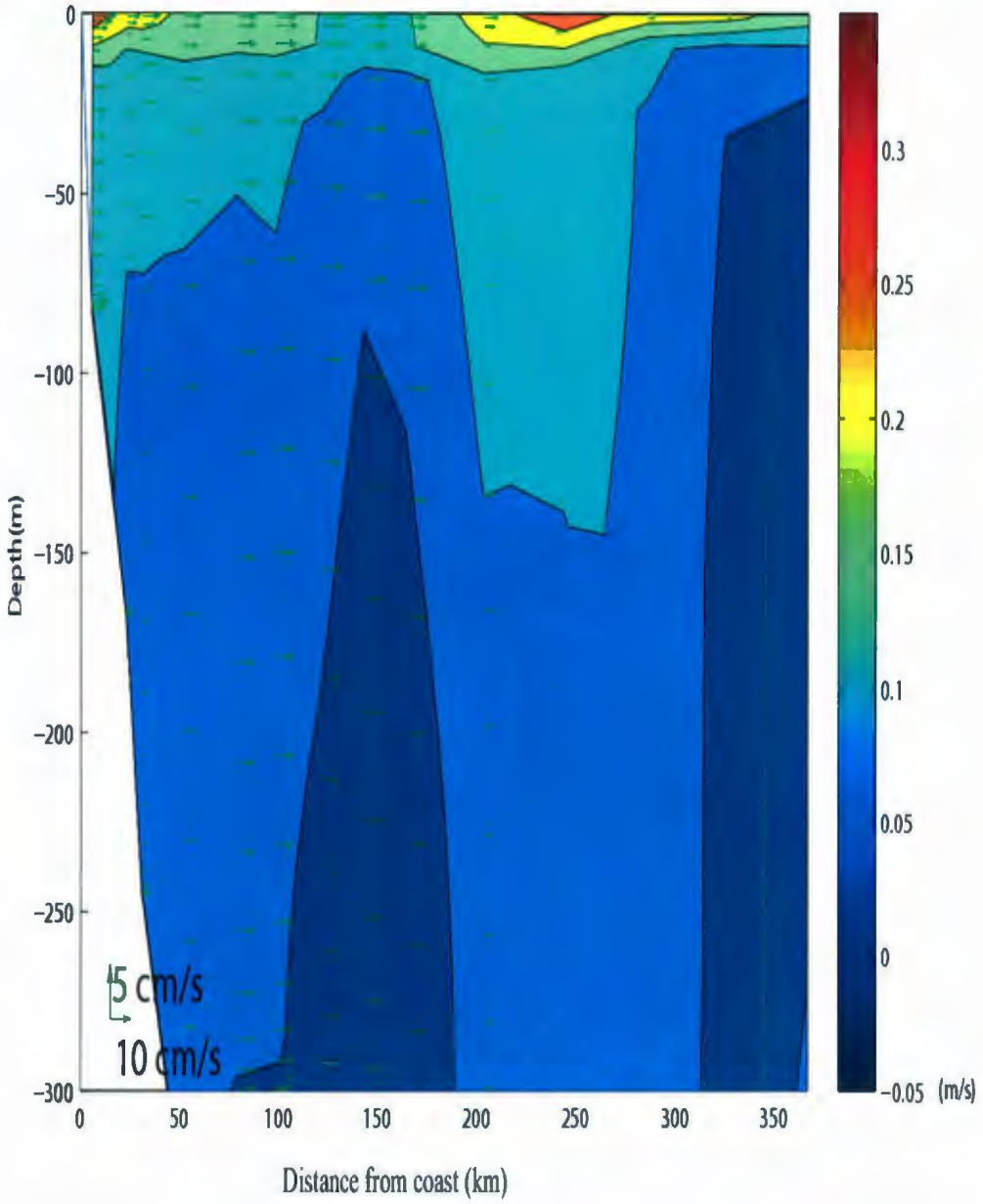

Figure 3.11: Velocity on the Bonavista transects in November from the model solutions. The color bands are for the normal currents (m/s), positive southward. The distance is measured from the coast.

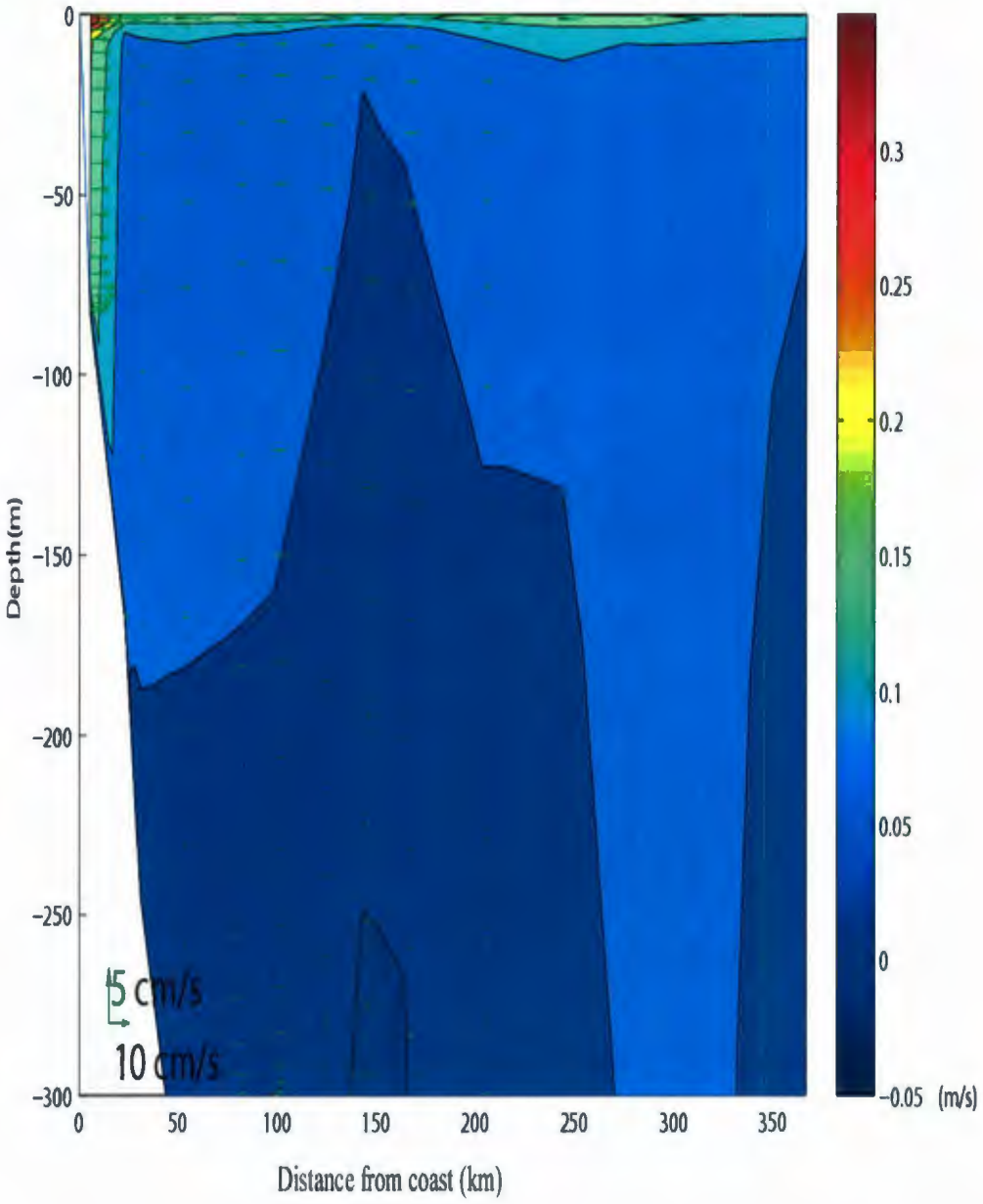

Figure 3.12: Velocity on the Bonavista transects in July from the model solutions. The color bands are for the normal currents (m/s), positive southward. The distance is measured from the coast.

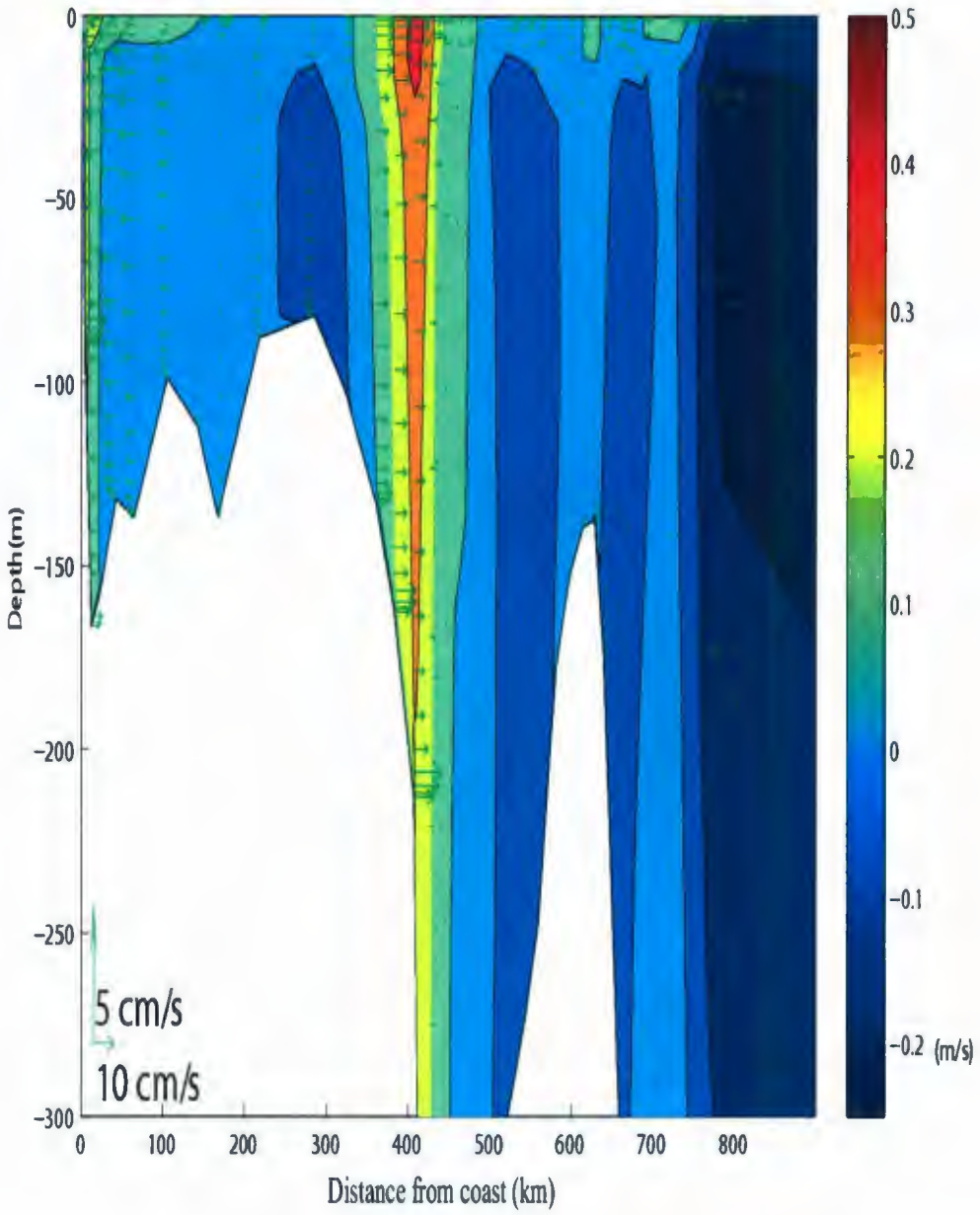

Figure 3.13: Velocity on the Flemish Cap transects in November from the model solutions. The color bands are for the normal currents (m/s), positive southward. The distance is measured from the coast.

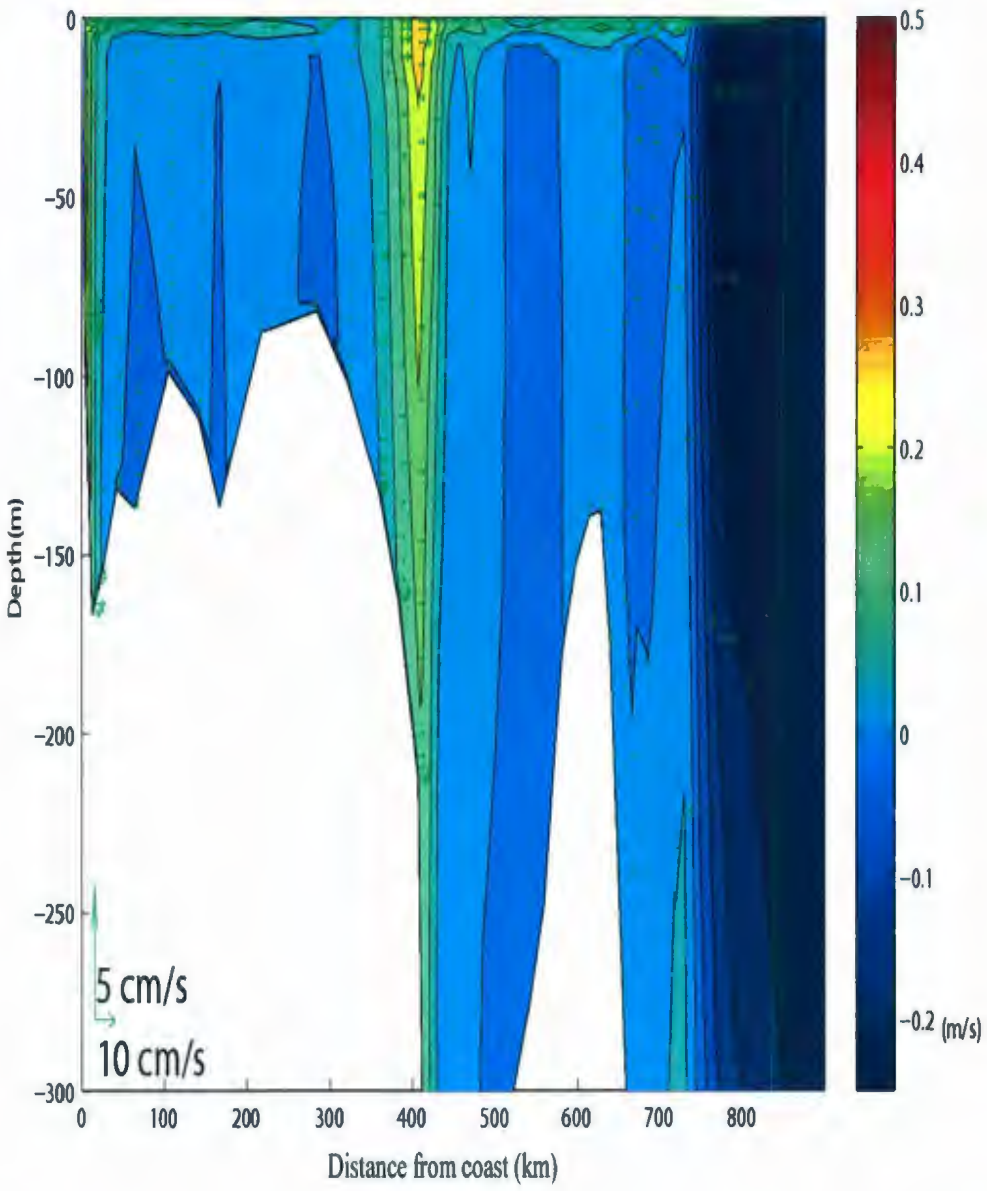

Figure 3.14: Velocity on the Flemish Cap transects in July from the model solutions. The color bands are for the normal currents (m/s), positive southward. The distance is measured from the coast.

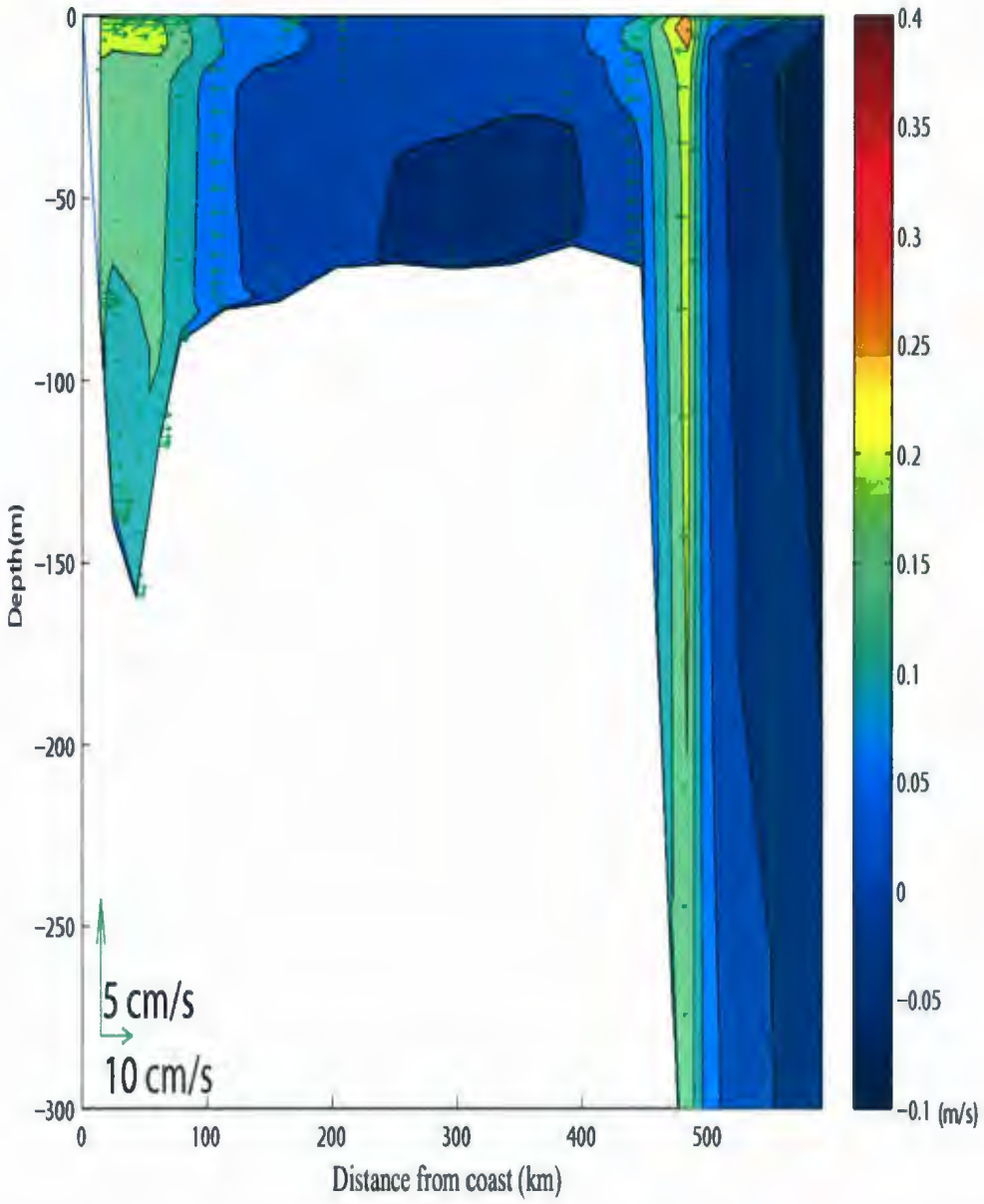

Figure 3.15: Velocity on the Southeast Grand Bank transects in November from the model solutions. The color bands are for the normal currents (m/s), positive southward. The distance is measured from the coast.

3.2 Monthly transport

3.2.1 Stream function

The depth-integrated stream function is calculated from the model solutions, with the stream function value set to zero along the coastline (Figures 3.16 and 3.17) and low values on the right looking downstream. From the contours of the stream function, we can also see important features of the Labrador Current: the strong shelf-edge branch and the weak inshore branch. The shelf-edge splits north of the Flemish Cap with one branch flowing eastward along the northern flank of Flemish Cap and the other southward through the Flemish Pass. A portion of the eastward branch circulates around the northern, eastern and southern flanks of the Flemish Cap and rejoins the shelf-edge current on the eastern Grand Bank edge. The inshore branch of the Labrador Current flows along the coastline of southern Labrador and northeastern Newfoundland, through the Avalon Channel, and then heads southwestward towards the shelf-edge. There are cyclonic gyres over the Orphan Basin and anti-cyclonic gyres over the Hamilton Bank and the Flemish Cap.

There is a strong seasonal cycle in the southward transport of the Labrador Current as well. Transport is larger in November and smaller in July. At places where the Labrador Current interacts with the Gulf Stream, such as in the vicinity of the Tail of the Grand

Bank, the shifting of the Labrador Current pathway and eddies are seen.

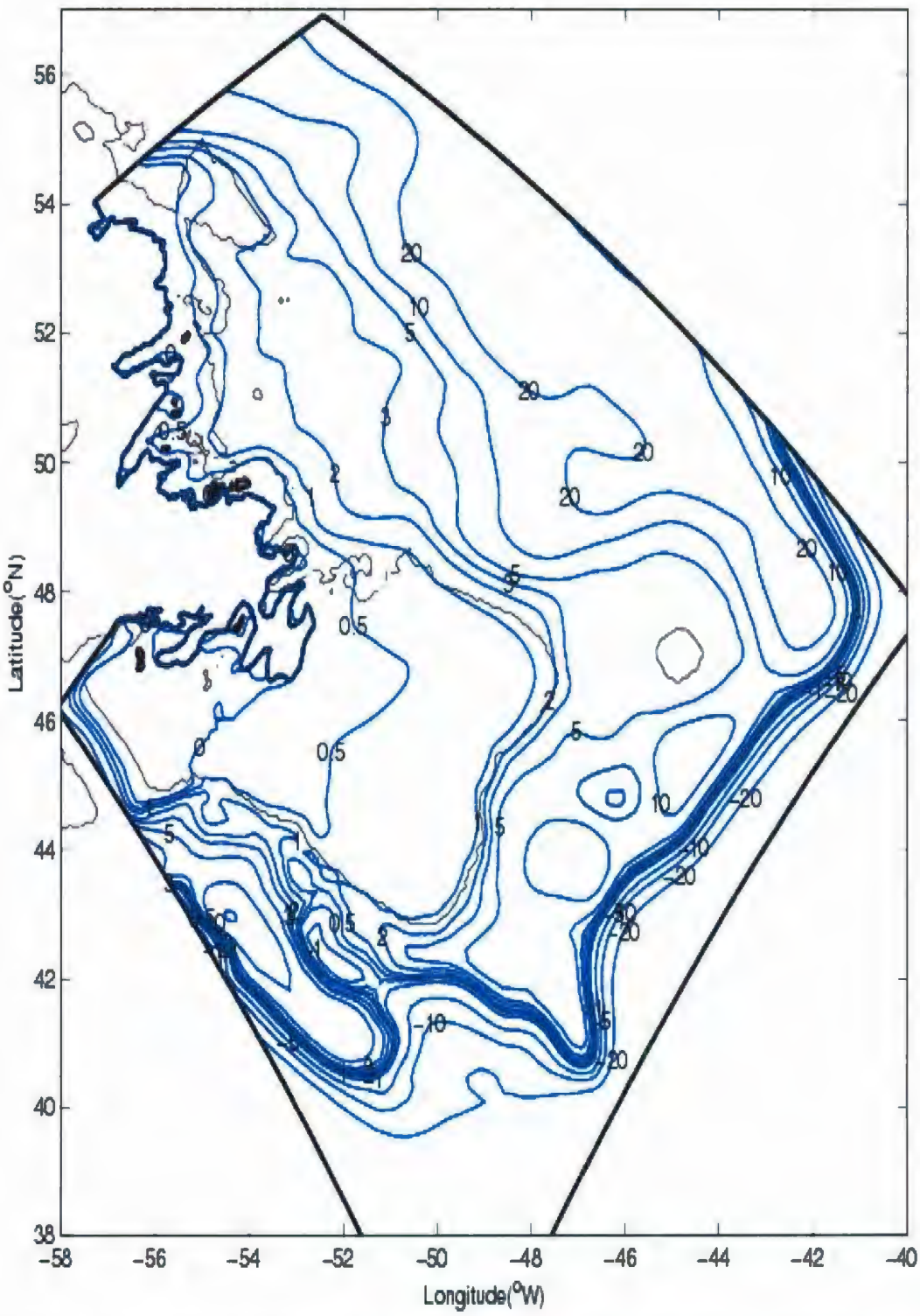

Figure 3.16: Monthly mean stream function in July from the model solutions. The contour unit is Sv.

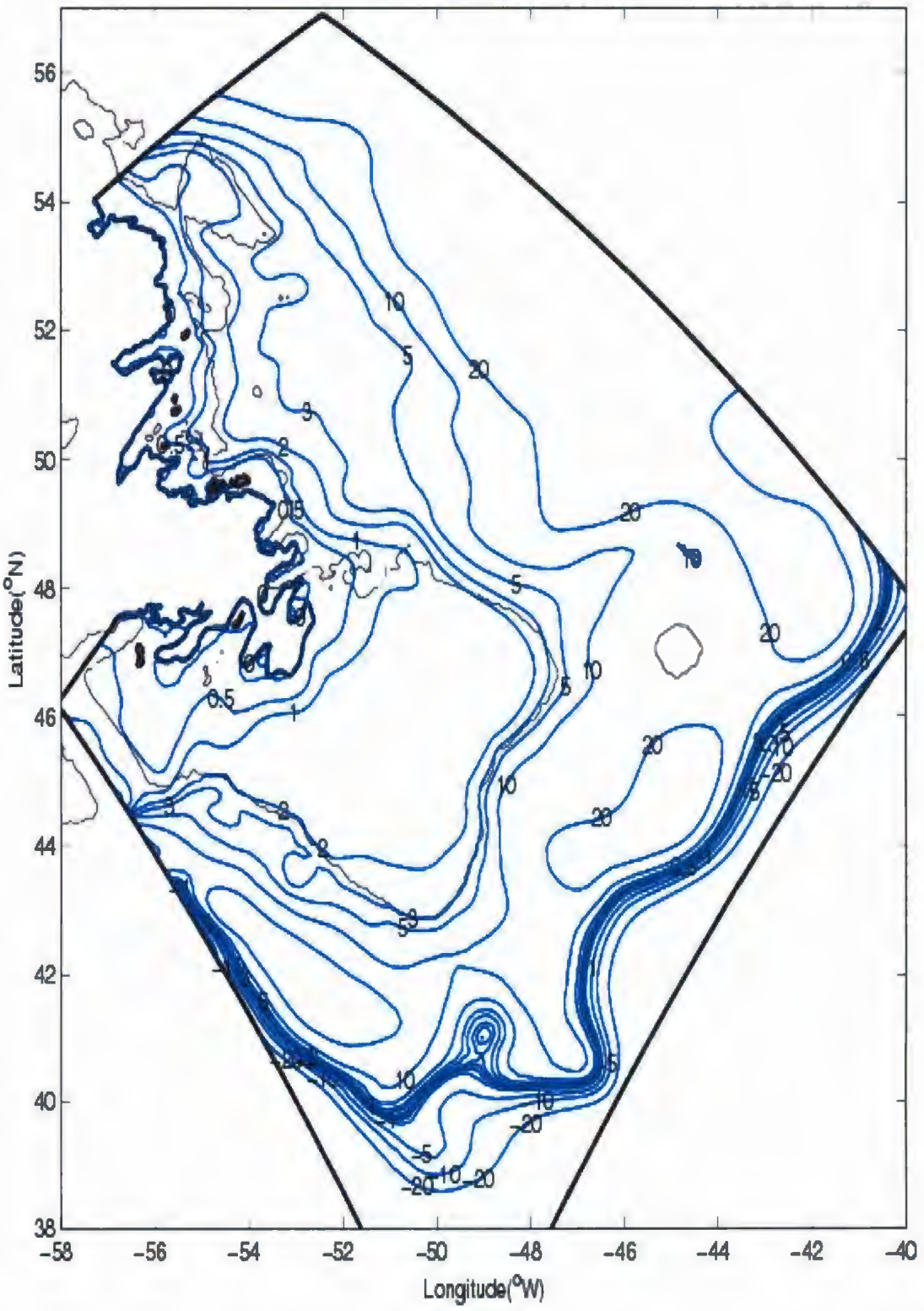

Figure 3.17: Monthly mean stream function in November from the model solutions. The contour unit is Sv.

3.2.2 Volume transport through 4 selected transects

In this subsection, we examine the volume transport of the Labrador Current through the four sAZMP transects (See Fig. 1.1 for locations). The volume transport through a segment was the difference of the stream function values at its two ending points. Two solutions using the T/S nudging method are presented in Figure3.18 to Figure 3.21: one with variable Coriolis parameters and the other with a constant Coriolis parameter at the central latitude of the region (47^{O}N).

The Seal Island transect is divided into three segments to facilitate a comparative discussion with previous studies. For solutions of both method, the inshore transport from the coast to the 250-m isobath at the Seal Island transect has a seasonal cycle of about 1.5 Sv associated with the inshore current, largest in December and smallest in May (Figure 3.18). Solutions from the two methods are very close for the inshore transport, but the solution using a variable Coriolis parameter is slightly weaker. For the shelf-edge current, the solution using a variable Coriolis parameter is about 1 Sv smaller than for the Constant Coriolis parameter solution throughout the year. The shelf-edge current has a seasonal change of about 3 Sv from the 200- to 1700-m isobaths, close to Han and Tang's (1999) estimate from altimetry and hydrography. The modeled seasonal cycle of transport from the 1700- to 3000-m isobaths is about 5.9 Sv for the variable Coriolis parameter solution and 6.9 Sv for the constant Coriolis parameter solution, both with maximum in November and minimum in July. The difference of transport at the Seal Island transect between the

two solutions is the direct effects of different Coriolis parameter applied in the model. At the Seal Island, which is close to our northern boundary, the Coriolis parameter applied in the variable Coriolis parameter run is bigger than the value of 47 °N, and a smaller current is expected according a geostrophic balance.

On the Bonavista transect, the transport of inshore current from variable Coriolis parameter run is about 0.5 Sv bigger than the transport from constant Coriolis parameter, but the currents of offshore branch of two methods are very close. On the Bonavista transect, the mean transport from variable Coriolis parameter run is 1.57 and 12.9 Sv for the inshore (depths < 300 m) and the slope current (300 to 2400 m) respectively (Figure 3.19). The mean transport from the variable Coriolis parameter run from the 300- to 1700-m isobaths is 9.1 Sv, which is greater than the result of 6.0 Sv from the 200 to 1700-m isobaths at Seal Island transect. This is consistent with the direct observation of the offshore flow through the Bonavista Saddle combining with the offshore branch (Figure 3.11-3.12). All currents are strongest in December and weakest in May.

On the Flemish Pass transect, the inshore transport from variable Coriolis parameter run is about 0.1 Sv bigger than the transport from constant Coriolis parameter, and the currents of offshore branch of two methods are very close as well. On the Flemish Cap transect, the mean modeled transport from the variable Coriolis parameter run is 0.68 and 5.6 Sv for the inshore Labrador Current through the Avalon Channel and the main branch through the Flemish Pass (from the 130-m isobath on the Grand Bank side to the 1140-m isobath on the Flemish Cap side), respectively (Figure 3.20). The maximum modeled

transport through the Flemish Pass from the variable Coriolis parameter run is about 7.75 Sv in November and December, and with a minimum is about 2.86 Sv in July and August. The transport through the Avalon Channel is estimated to be 0.39 Sv [Greenberg and Petrie, 1988] and the transport though Flemish Cap is estimated roughly to range between 6.3 and 9.8 Sv if archived current meter data are incorporated with the observations from current meter array [*Petrie and Buckley*, 1996]. The significantly reduced transport, both near-shore and through Flemish Pass, compared to the Bonavista transect is due to the splitting of the Labrador Current north of the Flemish Pass (*cf.* Han *et al.*, 2008).

On the Southeast Grand Bank transect, the inshore transport for the variable Coriolis parameter run is about 0.3 Sv greater than the transport from the run with a constant Coriolis parameter. There is a big discrepancy between the transport values of constant and variable Coriolis parameter runs. The discrepancy is associated with an eddy like feature over the southeast Newfoundland Slope in the constant Coriolis parameter solution. We are not sure if this feather is truly physical or not. On the Southeast Grand Bank transect, the modeled volume transport of inshore branch through the Avalon Channel is strong in winter and weak in summer. The mean transport for the variable Coriolis parameter run is 0.66 Sv (Figure 3.21), which is very close to the transport of 0.68 Sv through Avalon Channel at the Flemish Cap transect. The mean transport of the slope current (from the 70-m isobath on the outer Grand Bank edge to the 2400-m isobath) is 4.0 Sv for the variable Coriolis parameter run, which is close to the 3.2 Sv of geostrophic transport relative to 1000-m depth [Loder *et al.*, 1998]. For the variable Coriolis parameter run, the mean

transport from the 70- to 1700-m isobaths is 2.8 Sv. The transport is relatively highest in winter, and lowest in summer.

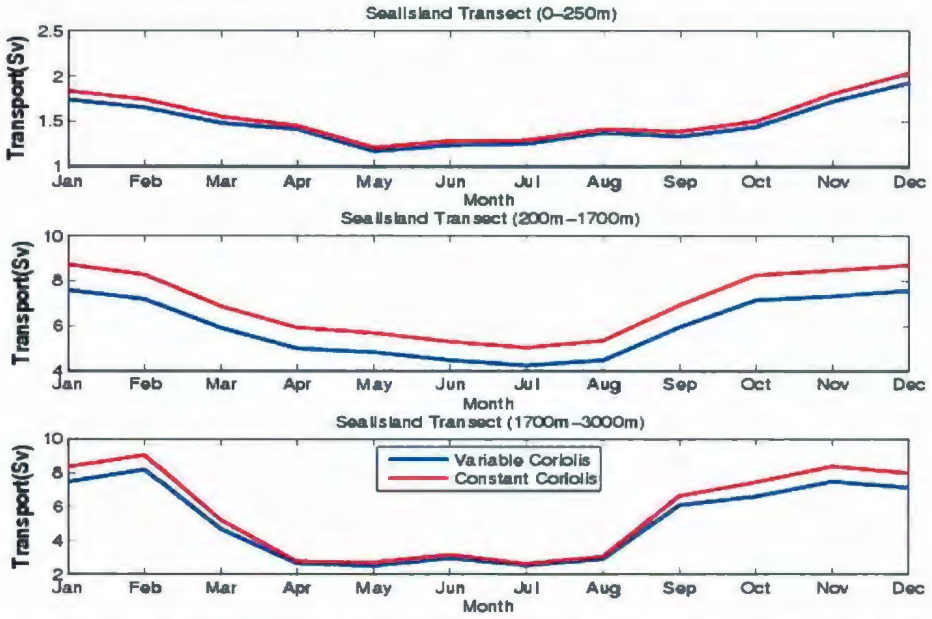

Figure 3.18: Monthly variations of volume transport (positive southward) through near shore and slope segments at the Seal Island transect. (Blue lines: solution with variable Coriolis parameters; Red line: Constant Coriolis parameters)

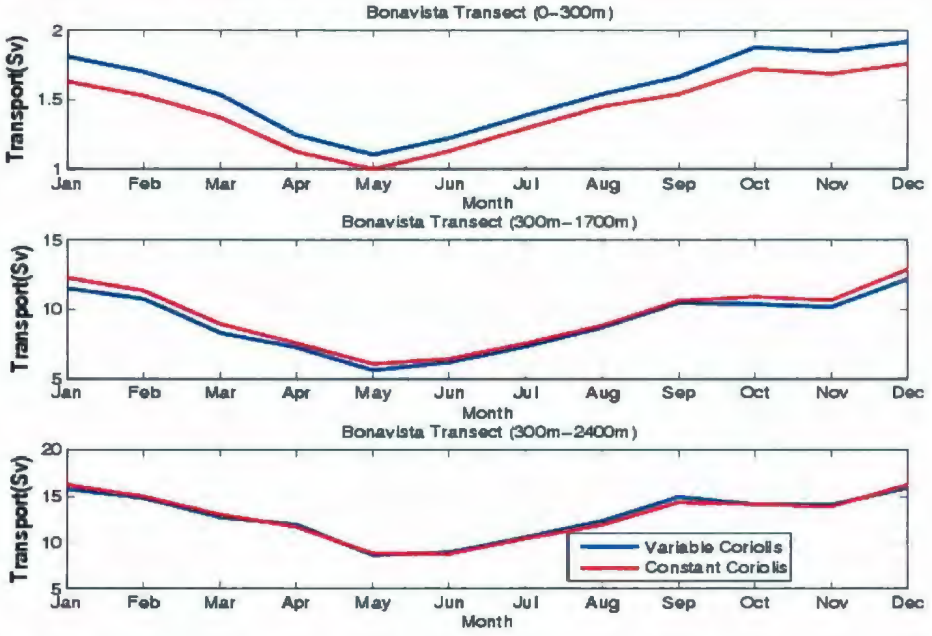

Figure 3.19: Monthly variations of volume transport (positive southward) through different segments at the Bonavista transect. (Blue lines: solution with variable Coriolis parameters; Red line: Constant Coriolis parameters)

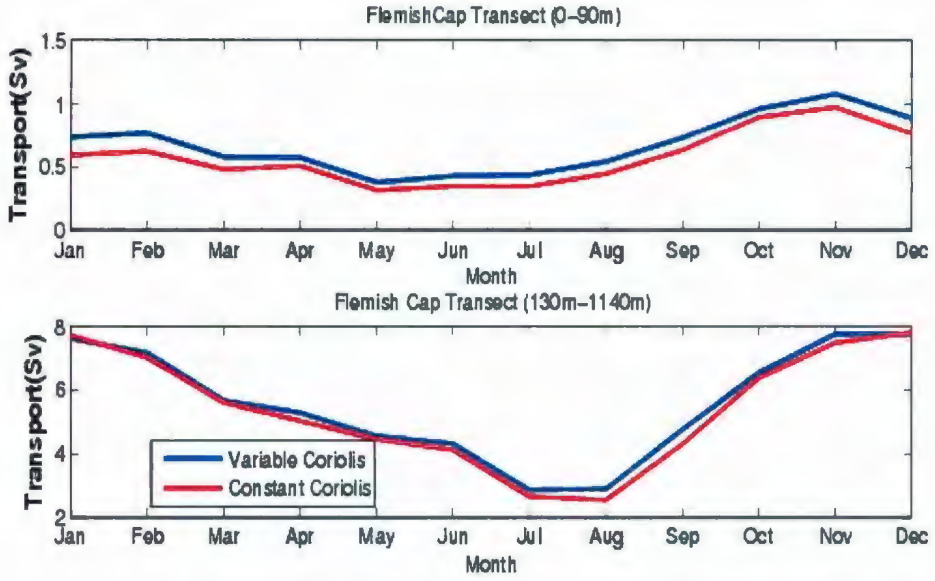

Figure 3.20: Monthly variations of volume transport (positive southward) through different segments at the Flemish Cap transect. (Blue lines: solution with variable Coriolis parameters; Red line: Constant Coriolis parameters)

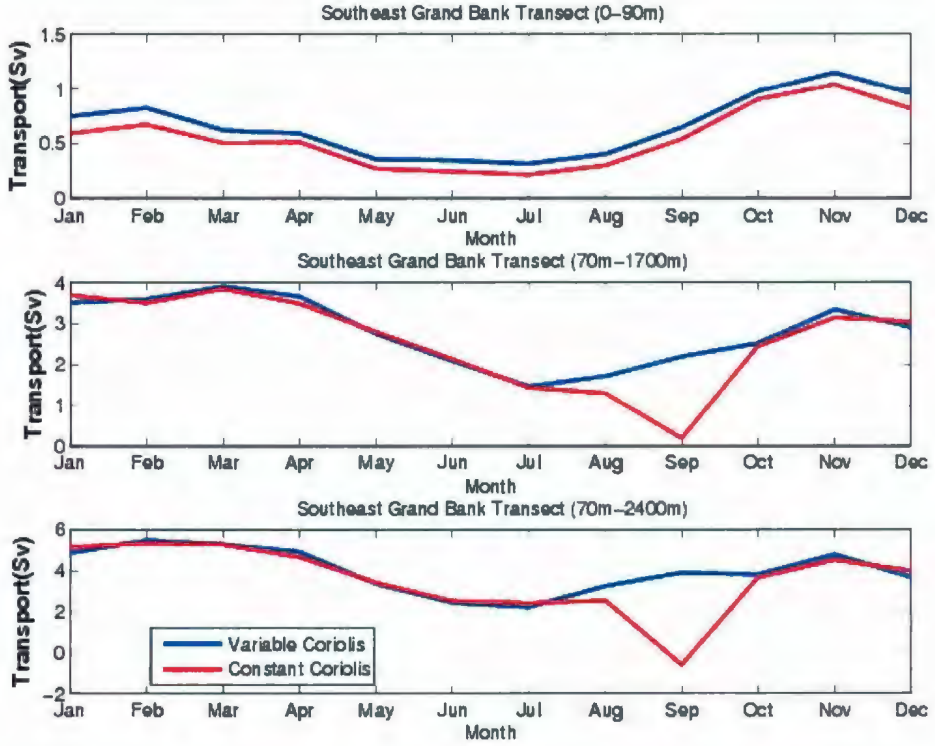

Figure 3.21: Monthly variations of volume transport (positive equatorward) through different segments at the Southeast Grand Bank transect. (Blue lines: solution with variable Coriolis parameters; Red line: Constant Coriolis parameters)

Chapter 4

Evaluation

In this chapter, monthly-mean model results from different nudging schemes are compared and evaluated against moored observations quantitatively. We will start with an examination of the temporal evolution of the proxy kinetic energy. We will focus on the solutions from the T/S nudging scheme with spatially variable Coriolis parameters. The results from the T/S nudging with the constant Coriolis parameter and from the diagnostic (density fixed) runs will be discussed as well.

4.1 Kinetic energy, temperature, salinity, and density

Figure 4.1 shows the temporal evolution of the mean squared, depth-averaged velocity obtained under T/S nudging schemes for November run. The velocity is also averaged for each M_2 cycle. For both runs with only the M_2 tidal constituent, rapid temporal evolution is found during the first 20 tidal cycles, with weak oscillations found after 40 tidal cycles. For the T/S nudging run with constant Coriolis parameter at the central latitude of the region (47^{O}N), there is an obvious oscillation at the synodical frequency of the M_2 and the

inertial wave (*cf.* Han *et al.*, 2008), which might be expected as the false numerical wave produced by the influence of constant Coriolis parameter. For the runs with the T/S nudging scheme and the variable Coriolis parameter, the oscillation in the constant Coriolis parameter hardly exists after the equilibrium state is reached at about 20 cycles, suggesting that the nudging scheme can effectively prevent the unrealistic model drift. The mean squared speed is slightly lower due to the reduced geostrophic inflow from the northern boundary. The results from cycle 58-61, when approximate dynamical equilibrium states are reached, are examined statistically against the observation in the following sections of the thesis.

Figure 4.2 shows time series of temperature and salinity from two different selected nodes, for the T/S nudging runs with the variable Coriolis parameter. Slight changes within each tidal cycle and between the tidal cycles are found. Figure 4.3 shows the vertical profiles of density after the dynamical equilibrium states are reached from T/S nudging runs, at selected nodes. The results from the solution with variable and constant Coriolis parameter are almost the same, and are very close to the initial vertical profiles as well. The advantage of the present T/S nudging scheme over the density fixed (diagnostic) approach is to allow some temporal adjustment of temperature and salinity under model dynamics, and to eliminate nonphysical features from the initial fields.

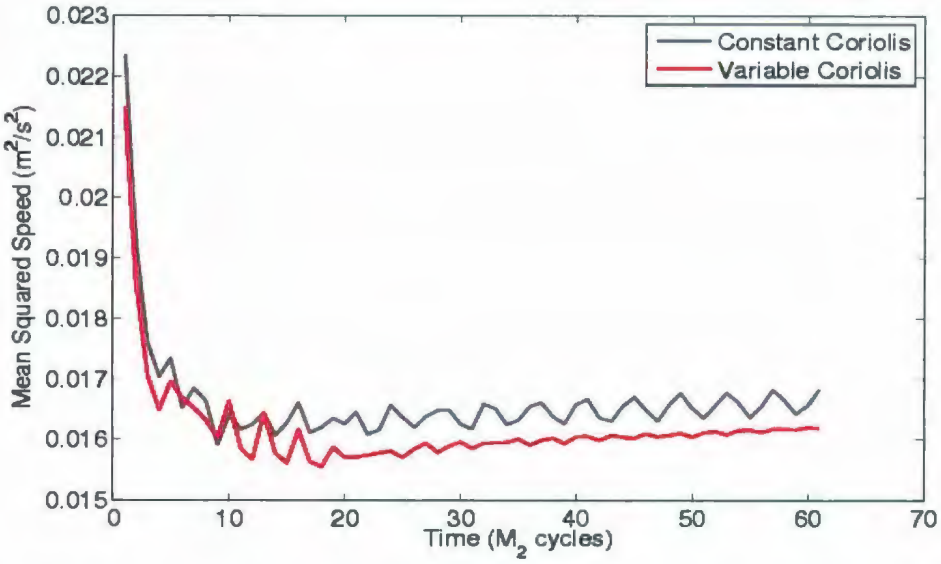

Figure 4.1: Mean squared speed of two different schemes in November, calculated based on the depth averaged and M_2 tidal cycle averaged model velocity.

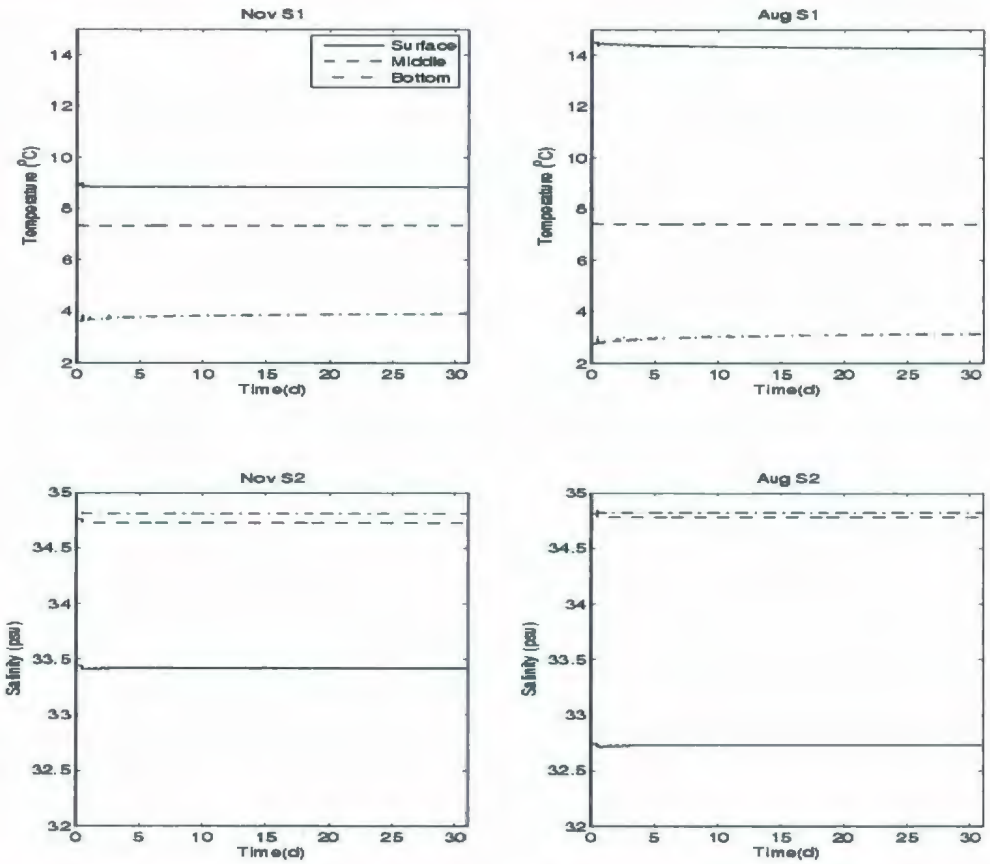

Figure 4.2: Time series of temperature and salinity from T/S nudging run with variable Coriolis parameters, for representative sites and months. (S1: at about 50 oW, 44 ON on the Grand Bank; S2: at about 50 oW, 52 ON, on the shelf edge.)

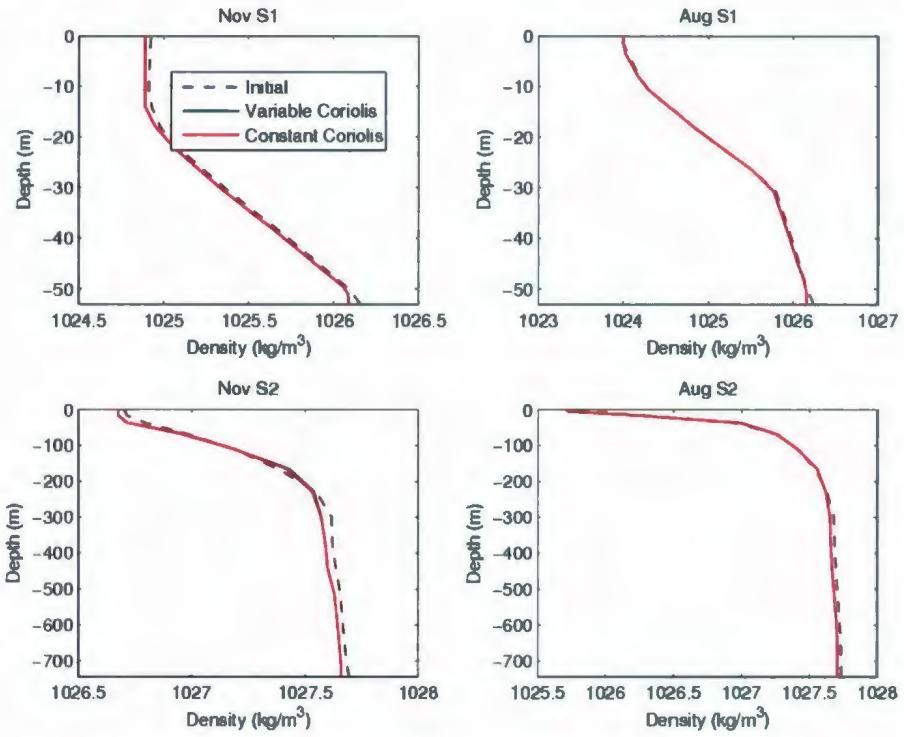

Figure 4.3: Vertical profiles of density from T/S nudging run with variable Coriolis parameters, for representative sites and months. (S1: at about 50 °W, 44 °N on the Grand Bank; S2: at about 50 °W, 52 °N, on the shelf edge.)

4.2 Evaluation of simulated currents

The model currents are evaluated against moored measurements. The moored current data are derived from the data base maintained at the Bedford Institute of Oceanography [*Gregory and Bussard*, 1996]. Monthly mean currents are derived from this data base for months with a minimum of 15 days of data. Typically, each mooring site has data from one to three vertical depths covering periods of one or two years (Figure 4.4).

The model current profiles are linearly interpolated to all moored sites for each

monthly mean circulation field. Figure 4.5 shows the vertical structures of simulation currents basically match the moored observation in those selected location and months, although in general the absolute value of model currents are smaller than their corresponding moored quantity. The primary features of the model-calculated circulation fields agree well with the moored observation in direction and vertical structure (Figure 4.5). Subsequently, the simulated vertical structures of both the variable and constant Coriolis parameters are very close to each other, at those selected locations. The simulated vertical profile in the upper water column can clearly explain the substantial portion of vertical shear, indicating the dominance of the baroclinic component of the Labrador Current.

For the vertical current profiles at the location north of the Grand Bank in April (A of Figure 4.6), the observed U and V components are slightly smaller than either of the simulated solutions. However, the simulated results at a nearby location in June agree well with the observed vertical profiles (B of Figure 4.6).

For the vertical profile on the Newfoundland Shelf (C of Figure 4.6), both simulated U and V components are close to the observed in the upper water column, but did not reproduce the relative strong U velocity of 0.10 m/s at the 300 m water depth.

The simulated vertical current profiles near Avalon Channel in August (D of Figure 4.6) are almost the same for the two methods, and basically agree with the observed weak inshore branch of the Labrador Current.

The amplitudes of simulated current profiles for the main branch of the Labrador

Current over the Newfoundland Shelf Slope in December (E of Figure 4.6) agree well with observations, except the observed relative weak V velocity of about 0.15 m/s at the 500 m depth. The amplitudes of both U and V from variable Coriolis parameters run are obviously smaller than the solutions from the constant Coriolis parameters run.

To evaluate the simulated result against moored observation quantitatively introduce a number of statistics for all observational sites for each monthly mean circulation field. The difference ratio (DR) is defined as the ratio of the sum of squared differences between the observed velocities ($\mathbf{v}_o$) and modeled velocities ($\mathbf{v}_m$) to the sum of squared observed currents, and is expressed as:

$$DR=\Sigma|\mathbf{v}_m-\mathbf{v}_o|^2/\ \Sigma|\mathbf{v}_o|^2. \qquad (4.1)$$

The vector velocity difference (VVD) is the magnitude of the difference vector between the observed and modeled velocities. The difference angle (DA) is the magnitude of difference in direction between the observed angles ($\boldsymbol{\alpha}_o$) and modeled angles ($\boldsymbol{\alpha}_m$), which is expressed as:

$$DA=\text{mean}\ (\ AbsDA)\ \pm\ \text{std}\ (AbsDA) \qquad (4.2),$$

where $AbsDA=\min(\text{mod}(|\boldsymbol{\alpha}_m-\boldsymbol{\alpha}_o|,360),360-\text{mod}(|\boldsymbol{\alpha}_m-\boldsymbol{\alpha}_o|,360))$, mean denotes an average of $AbsDA$, std denotes the standard deviation, min denotes the minimum mathematical function, and mod denotes the modulus mathematical function. Corr is short for the correlation coefficient for 95% confidence level in Table 4.1- Table 4.4.

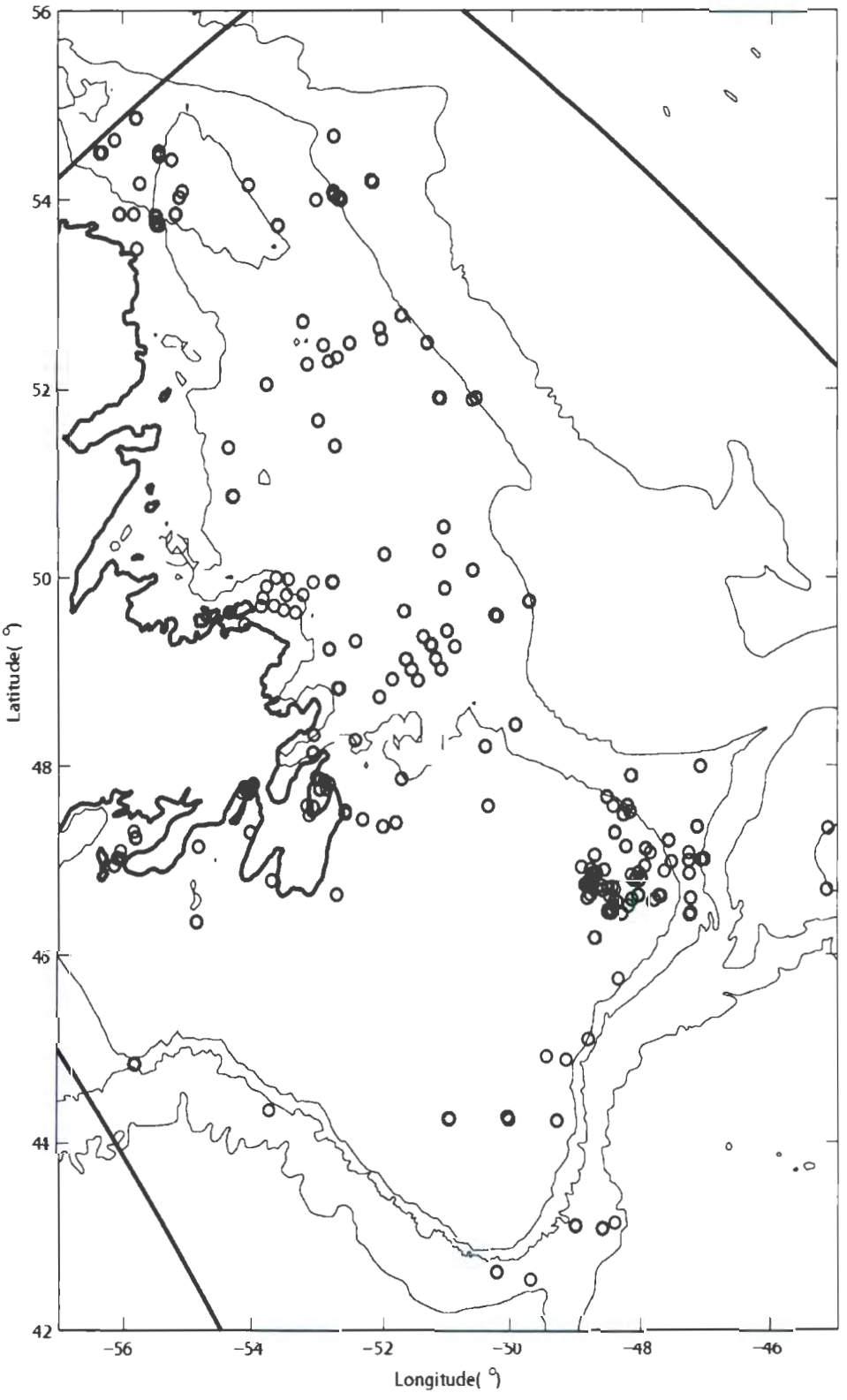

Figure 4.4: Historical moored measurements location for all months used to evaluate the model results. The 200, 1000, 3000 m isobaths are also shown.

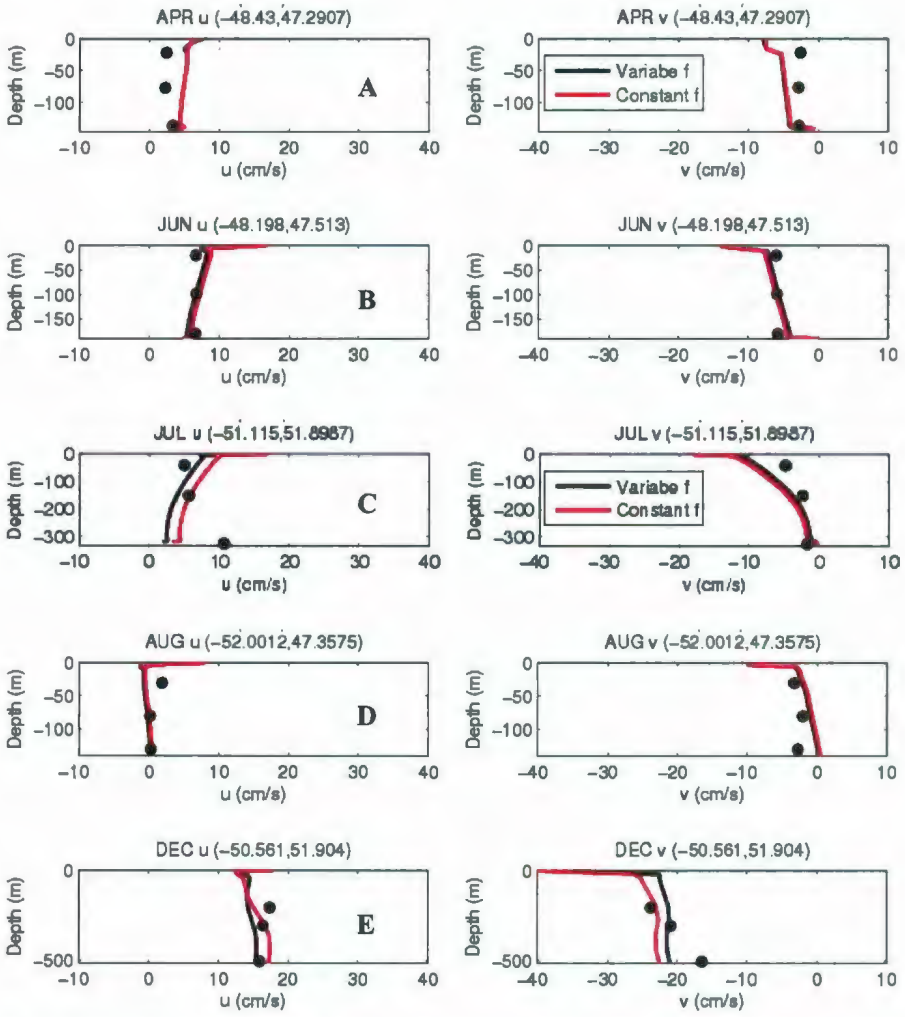

Figure 4.5: Simulated currents from T/S nudging method of variable Coriolis parameters (black solid curve), and constant Coriolis parameters (red solid curve), and moored measurements (dots) in different months. U and V are the eastward and northward components, respectively. See the titles for the months and locations.

Tables 4.1- 4.3 list the statistics of comparison between historical observed current and modeled mean currents and show very similar results produced by all methods.

For most months, the simulated current speed is overall less than that observed, except for January, February and April. In general, the average magnitudes of the model are similar to observed currents, but the average magnitudes of the vector velocity difference and difference angle indicate substantial model–observation discrepancies. The agreement

is usually better for the fall, when the current is strong and there is no ice present. With the T/S nudging scheme, the solutions from the variable Coriolis parameter show slightly better skills over those from the constant Coliolis parameter. The T/S nudging schemes can improve the model solutions in summer months (August-October).

The statistics of different frictional parameters applied in the November diagnostic runs (Table 4.4) are almost the same, indicating that the model simulated current and the volume transport are not sensitive to the vertical eddy viscosity.

Table 4.1 Statistics (means and standard deviations) of the comparison between observed and model simulated mean currents with the fixing density (diagnostic) method with variable Coriolis parameter at mooring sites.

		Average Speed cm/s				Velocity Deviations	
Month	No.Obs	Obs	Model	DR	Corr	VVD,cm/s	DA,deg
January	111	11.0±8.3	13.6±9.3	0.75	0.68	9.6±7.1	33±52
February	99	9.7±6.8	10.6±7.8	0.51	0.76	6.8±5.1	43±74
March	93	9.4±6.6	7.7±6.6	0.52	0.70	6.2±5.4	35±58
April	82	8.3±5.3	8.7±8.4	1.06	0.55	6.9±7.5	37±61
May	92	7.6±4.8	6.2±6.0	0.69	0.60	5.6±4.9	36±55
June	117	7.4±5.0	5.5±3.3	0.50	0.70	5.0±3.8	47±69
July	169	8.3±6.3	6.7±5.7	0.54	0.68	6.0±4.7	39±56
August	184	8.6±6.0	7.5±7.0	0.77	0.60	7.1±5.8	45±61
September	169	9.2±6.4	8.7±6.6	0.57	0.68	6.6±5.4	41±61
October	127	9.6±7.1	9.4±6.7	0.54	0.68	7.3±4.9	53±80
November	93	12.0±8.7	11.0±8.0	0.32	0.81	7.0±4.6	25±38
December	114	12.6±9.3	12.7±9.0	0.49	0.73	8.9±6.5	46±71

Table 4.2 Statistics (means and standard deviations) of the comparison between observed and model simulated mean currents with the T/S nudging approach with constant Coriolis parameter at mooring sites.

	Average Speed cm/s					Velocity Deviations	
Month	No.Obs	Obs	Model	DR	Corr	VVD,cm/s	DA,deg
January	111	11.0±8.3	14.1±9.5	0.76	0.69	9.8±6.9	32±49
February	99	9.7±6.8	11.2±8.2	0.56	0.76	7.2±5.2	45±78
March	93	9.4±6.6	8.2±7.2	0.52	0.71	6.4±5.3	35±61
April	82	8.3±5.3	9.2±8.7	1.11	0.57	7.1±7.6	36±61
May	92	7.6±4.8	6.7±6.5	0.7	0.63	5.5±5.1	37±50
June	117	7.4±5.0	5.7±3.4	0.47	0.73	5.0±3.5	48±65
July	169	8.3±6.3	7.1±5.9	0.56	0.68	6.1±4.7	43±56
August	184	8.6±6.0	7.5±6.3	0.71	0.61	7.0±5.5	47±61
September	169	9.2±6.4	8.4±6.1	0.48	0.73	6.2±4.7	43±65
October	127	9.6±7.1	9.2±6.7	0.51	0.7	7.1±4.7	52±77
November	93	12.0±8.7	11.3±8.2	0.35	0.79	7.3±4.8	28±44
December	114	12.6±9.3	13.2±9.3	0.49	0.75	9.0±6.3	44±67

Table 4.3 Statistics (means and standard deviations) of the comparison between observed and model simulated mean currents with the T/S nudging approach with variable Coriolis parameter at mooring sites.

	Average Speed cm/s					Velocity Deviations	
Month	No.Obs	Obs	Model	DR	Corr	VVD,cm/s	DA,deg
January	111	11.0±8.3	13.4±9.2	0.71	0.69	9.3±6.9	32±50
February	99	9.7±6.8	10.6±7.8	0.52	0.76	6.8±5.1	45±78
March	93	9.4±6.6	7.6±6.8	0.52	0.70	6.2±5.4	36±61
April	82	8.3±5.3	8.7±8.5	1.10	0.54	7.0±7.6	37±62
May	92	7.6±4.8	6.1±6.2	0.71	0.59	5.7±5.0	37±51
June	117	7.4±5.0	5.4±3.2	0.48	0.72	5.0±3.6	50±72
July	169	8.3±6.3	6.7±5.6	0.54	0.68	6.0±4.6	41±56
August	184	8.6±6.0	7.2±6.0	0.68	0.61	6.9±5.3	45±59
September	169	9.2±6.4	8.2±5.8	0.46	0.73	6.1±4.6	41±62
October	127	9.6±7.1	8.8±6.2	0.49	0.70	6.9±4.7	48±71
November	93	12.0±8.7	10.7±7.9	0.33	0.80	7.0±4.9	31±51
December	114	12.6±9.3	12.5±9.0	0.48	0.74	8.7±6.4	44±66

Table 4.4 Statistics (means and standard deviations) of the comparison between observed and model simulated mean currents fixing density with different viscosity parameter for November at mooring sites.

	Average Speed cm/s					Velocity Deviations	
Viscosity(m^2/s)	No. Obs	Obs	Model	DR	Corr	VVD,cm/s	DA,deg
0.0001	93	12.0±8.7	11.5±8.2	0.34	0.80	7.3±4.6	29±47
0.00005	93	12.0±8.7	11.5±8.2	0.34	0.80	7.3±4.6	29±47
0.00001	93	12.0±8.7	11.5±8.2	0.34	0.80	7.3±4.6	29±47

4.3 Monthly mean sea level at St. John's

Sea level data at the St. John's tide-gauge station for 1961 to 2001 are obtained from the World Ocean Circulation Experiment Data Information Unit (free access from NASA's website). The original hourly residuals data are averaged for each month. To compare with observations, the model simulated monthly mean sea level at the nearest node, which is about 2.7 km away, is extracted from the density fixed runs (Figure 4.6). The modeled sea levels match the observations very well. Significant seasonal variations are found in the modeled sea level at St. John's and in observation as well. The seasonal variation of sea levels, transport, and Labrador Current speed are in phase. The maximum sea level can be found in December, while the minimum happens in May, for both simulated and observed. The seasonal variation is about 18 cm in range and the correlation coefficient between the model and the tide-gauge data is about 0.99, which suggests that the model simulated sea level accounts for the almost all portion of the seasonal sea level variability as measured by the tide gauge. The missing component could be the sea level variations associated with non-modeled processes.

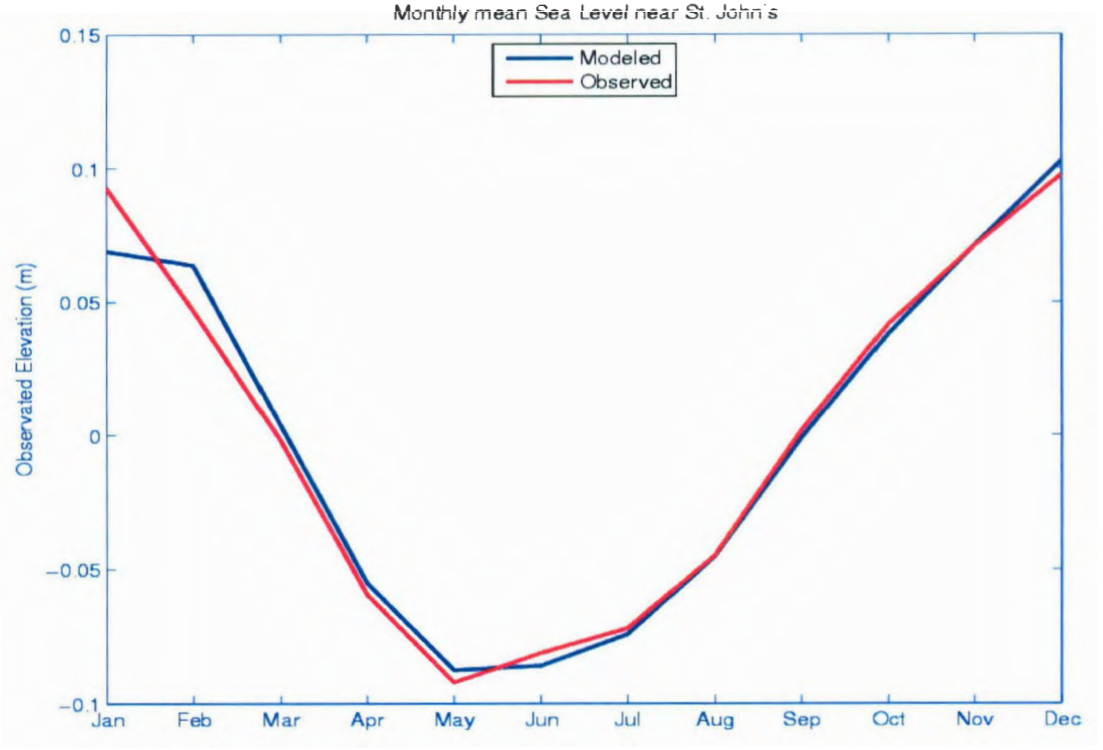

Figure 4.6: Observed monthly long time mean sea level changes at St. John's fixed tide-gauge station (Red) and model simulated monthly mean sea level at the nearest node to St. John's (Blue), which is about 2.7 km away. Note the two original heights have been referred to the different places and the long time means were removed from both modeled and observed, for easy comparison.

Chapter 5

Harmonic tidal analysis results

5.1 Introduction

In this section, tidal harmonic analysis of the simulated sea surface elevation and current from the November run with 5 tidal constituents are discussed. The aim of this chapter is to determine quantitatively tidal elevations, 3-D currents for the major three leading semi-diurnal (M_2, S_2 and N_2) and two diurnal (K_1 and O_1) constituents.

In the coastal and shelf regions, tides strongly influence the circulation associated with vertical mixing, horizontal exchange and other small scale processes such as high frequency internal waves. Ocean tides over the Newfoundland Shelf are mainly forced by adjacent deep ocean tides. The tidal elevation and currents are intensified as the tidal waves approach the shallow shelf areas. The tidal wave over the shelf area generally travels as a trapped Kelvin wave against coastline, as the Coriolis effects induced a trapping mechanism. On the Grand Banks, where the depth is less than 200 m, tidal components account for about 91% of the total variance of the sea surface elevation

[*Petrie, et al.*, 1987]. Over the outer Grand Banks, the tidal band account for 51% of the total current variance for periods longer than 12 hours [*Petrie, et al.*, 1987]. Tidal models have been applied in the area and improved the tidal charts [*DuPont, et al.*, 2002; *Han*, 2000].

It is important for short-term forecasts of passive drifter trajectories response to the significant tidal currents. The simulated tidal elevation is also crucial to detide altimetric height [*Han*, 1995; *Han, et al.*, 1993], and the simulated tidal currents are important to detide ADCP current data.

In the Chapter, an extra November run of the fixing density method was set up, with 3 leading semi-diurnal (M_2, S_2 and N_2) and 2 diurnal (K_1 and O_1) applied along the open boundary, instead of M_2 only in the preceding two chapters.

5.2 Tidal Analysis Method

The harmonic method, developed by Lord Kelvin in 1876, is commonly used for analyzing tides. The principle of the harmonic analysis is that the ocean tides can be decomposed into a series of tidal constituents in the form of a combination of sine (or cosine) functions with specified frequency and initial phase. If applied to tidal current data with both U and V components, it is called Harmonic Tidal Currents Analysis. The least squares fit approach was used to implement the harmonic method to decompose the amplitude and phase for the

five tidal constituents. Interference between different tidal constituents in shallow was not considered. The harmonic tidal analysis is applied to the surface elevation time series at all nodes, and harmonic tidal currents analysis is applied to all current time series as well.

The model was integrated for 60 simulated days and the elevation and current field (U and V components) were output hourly. The model outputs of the last 30 days were used in the harmonic analysis to derive the five tidal constituents. The period of 30 simulated days is long enough to distinguish the five tidal constituents and the period of the first 30 simulated days is enough for the model to reach a state of dynamical equilibrium.

5.3 Surface Elevation

5.3.1 Co-amplitude and Co-phase charts

Figure 5.1 shows the model computed co-tidal charts of M_2 tidal constituents, the most energetic constituent of the semidiurnal band. The amplitude increases when propagating from the deep ocean toward the coastline. From the co-phase chart, an overall anticlockwise propagation can be found. An amphidromic point occurs in the deep North Atlantic [*Schwiderski*, 1980], at 48° N, 41° W, near or outside the eastern boundary of the model domain. The tidal wave propagates westward over the southwestern Newfoundland

Shelf. Along the Newfoundland coastline, form north to west of Avalon Peninsula, the amplitude increases from 0.4 m to above 0.6 m. The amplitude is over 0.6 m in Placentia Bay, consistent with previous descriptions of the regional M_2 tide [Petrie *et al.*, 1987; Han, 2000]. The amplitude increases from 0.2 m to 0.3 m after the tidal wave reaches the southeastern Grand Banks and there is a change in the phase direction as the co-phase line follows the isobath near the Grand Bank edge. Rapid amplitude and phase shifting can be found in the Strait of Belle Isle as well. The distributions of co-amplitude and co-phase can be characterized by a coastal Kelvin wave, in general.

The K_1 tidal wave off the Canadian Atlantic coast propagates along the continental margin equatorward, with a mid-ocean amphidrome. Generated by the irregular coastline with various inland sea and embayments, local amphidromes on the Canadian Atlantic Shelf are also observed. Associated with an estuarine interaction between the shelf diurnal regime and the diurnal response in the Gulf of St. Lawrence, amphidromes west of the southwestern Newfoundland Shelf can also be found [*Godin*, 1980; *Han, et al.*, 1996]. Figure 5.2 shows the modeled co-tidal chart of K_1, the most energetic constituents at the diurnal bands. The simulated K_1 tide propagates southward with the amplitude decreases southward from about 0.12 m in the northern boundary to 0.06 m at 46°N. South of the Grand Bank, the amplitude is quite uniform. The presence of an amphidromic point can be found west of the Newfoundland Shelf (Figure 5.2), is consistent with other North Atlantic modelling [*Egbert, et al.*, 1994; *Han, et al.*, 1996]. Rapid shifts of amplitude and phase can be found in the Strait of Belle Isle as well. In Figure 5.2, some diurnal intensification over

the outer shelf and shelf break can be found, due to a shelf wave resonance. Overall, the simulated K_1 pattern shows significant differences compared with the M_2 co-tidal chart over the Newfoundland Shelf.

Figure 5.3 shows the model computed co-tide charts of the S_2 tidal constituent. The spatial distribution of S_2 is similar to that for M_2, but with much smaller amplitudes overall. The maximum amplitude of S_2 is 0.2 m near the northern boundary. The co-tidal chart of N_2 (Figure 5.4) is especially similar to the M_2 chart and the maximum of N_2 amplitude is 0.12 m near the northern boundary.

Figure 5.5 shows the model computed co-tide charts of O_1 diurnal tidal constituent. The simulated O_1 tide propagates southward with the amplitude decreases southward from about 0.07 m in the northern boundary to 0.04 m at 46°N, and then travels westward along the shelf with increasing amplitude toward the coastline.

Overall, the semidiurnal constituents are significantly stronger than the diurnal constituents. Tides on the outer Newfoundland Shelf can be categorized as mixed, but mainly semidiurnal. Near the Newfoundland coast, tides can be characterized by semidiurnal. The spatial features of those five tidal constituents are consistent with results from previous studies in general [Godin, 1980; Petrie 1987; Han *et al.*, 1996].

5.3.2 Evaluation with observations

The tidal elevation data are from 44 coastal tidal gauge and bottom pressure gauge (Figure 5.6). The observations of tidal constituents are extracted from the database maintained by

the Canadian Hydrographic Service, bottom pressure gauges in the Labrador Sea and on the Labrador Shelf are obtained from Wright *et al* (1988), and TOPEX/Poseidon altimetry (Han, 1996). The phases were adjusted to Greenwich Mean Time.

The model solutions were interpolated to the observation points for evaluation. Three measures were employed to obtain a quantitative assessment of the model solutions: the Root Mean Square (RMS) difference between the observed and simulated, for amplitude and phase of each constituent; the average absolute RMS error (AbsErr) and the relative RMS error (RelErr).

The RMS difference over a tidal cycle is defined as:

$$D = [\frac{1}{2}(A_o^2 + A_m^2) - A_0 * A_m * \cos(\phi_o - \phi_m)]^{1/2} \tag{5.1}$$

Where A_o and A_m are the amplitudes of observation and model, ϕ_o and ϕ_m are the phases of observation and model.

The *AbsErr* is defined as:

$$AbsErr = L^{-1}\sum\nolimits_L D \tag{5.2}$$

And *RelErr* is defined as

$$RelErr = L^{-1}\sum\nolimits_L D / A_o \tag{5.3}$$

Figure 5.7 shows the scatter diagrams of the modeled elevation against observed for each tidal constituent. The modeled results of the M_2 agree well with the observations for both amplitude and phase. The model produced the elevations of the semidiurnal constituents better than those of the two diurnal elevations. For the two diurnal

constituents, there are obvious phase discrepancies between the model and observation on the southwest Newfoundland coast, which is close to the amphidrome and west boundary.

The detailed comparison between simulated and observed elevation, amplitude and phase is given in Table 5.1. The M_2 constituent has the biggest RMS amplitude difference of 3.3 cm, the smallest RMS phase difference of 2.4°, and the smallest RelErr of 7.7%. The S_2 and N_2 constituents have similar results to M_2 constituent. The K_1 constituent has the poorest RelErr of 28.4%. The results show that the diurnal constituents have smaller absolute amplitude differences but larger relative differences, compared to semidiurnal constituents, suggesting that our model is not sensitive enough to reproduce the relative weak diurnal tidal constituents near the Newfoundland coast.

5.4 Tidal Currents

5.4.1 Tidal current ellipses

Figure 5.8 shows the model simulated M_2 tidal currents ellipses at the surface. The simulated M_2 tidal current is weak on the outer Labrador shelf, and is relatively stronger on the inner shelf region, where the maximum can reach 0.10 m/s. A rectilinear tidal current is found along the Avalon Peninsula and in the Avalon Channel with the major axis aligned along the channel. Over the Grand Bank, the tidal flow pattern is more circular. The maximum current occurs in the outer shelf and shelf break areas, with an amplitude of over 0.2 m/s. Near the Southeast shoal where the water depth is less than 100 m, the tidal current can reach 0.3 m/s. Relatively strong tidal current can be found over the Flemish Cap as well, with a magnitude of about 0.10 m/s. The M_2 tidal currents in the deep ocean are much weaker, as expected. Off the Labrador and Newfoundland Shelf, the current ellipses are generally oriented in the along-shelf direction. A particularly large linearly rectilinear tidal flow can be found in the Strait of Belle Isle, with major axis aligned along the strait.

The model simulated K_1 tidal current ellipses at the surface show (Figure 5.9) that compared to the M_2 constituent, the K_1 tidal current is generally weak. Strong currents are

found over the northeast part of the Grand Bank near Flemish Pass, over the Flemish Cap, southwestern part of the Grand Bank near Gulf of Lawrence, and southern Labrador Sea near the Hamilton Bank. The currents over the Banks or shelf break can reach 0.10 m/s. The strongest tidal current is on the southwestern outer Newfoundland Shelf, with a magnitude of over 0.2 m/s. According to Kelvin wave theory, the K_1 current is estimated to be 0.01-0.02 m/s from the simulated K_1 elevation amplitude. The localized diurnal current intensification might be explained by the continental shelf waves with large currents and small elevation [*Crawford and Thomson*, 1982; *Huthnance, et al.*, 1986; *Proctor and Davies*, 1996]. Since the occurrence of a first-mode shelf wave at the K_1 frequency is allowed by the dispersion relationship for the western and northern Grand Banks sections crossing the intensification areas [Han, 2000], the intensification is probably induced by the resonance between a first-mode continental shelf waves and the K_1 tidal wave.

Figures 5.10 and 5.11 show the model simulated surface S_2 tidal currents ellipses and N_2 ellipses, respectively. Both tidal currents patterns of S_2 and N_2 are very similar to the results from M_2, with much smaller amplitudes and slight difference in ellipse semi-major directions. Though the amplitude of S_2 tidal elevations is bigger than N_2 tidal elevations, the amplitude of S_2 tidal currents is slightly smaller than N_2 currents.

The model simulated O_1 tidal currents ellipses at the surface (Figure 5.12) are similar to K_1 as well, except for a slightly smaller amplitude and direction differences. Moreover, there is no strong O_1 tidal current in the Labrador Sea near Hamilton Bank, compared to the K_1 one. The significant localized intensification on the southwestern and northeastern

outer shelf and Flemish Cap can be found as well. The intensification can also be explained by resonance between first mode continental shelf wave and O_1 tidal wave.

5.4.2 Evaluation with observations

The observed tidal current data are extracted from the Northwest Atlantic tidal current database [*Drozdowski, et al.*, 2002]. For demonstrative purpose, 176 *in situ* positions were selected based on the criterion of excluding M_2 tidal current magnitude smaller than 2 cm/s, K_1 tidal current magnitude smaller than 1 cm/s and locations too close to the open boundary (Figure 5.13).

Figures 5.14-5.17 show the comparison of the observed tidal ellipses and the modeled ones, for three sites with multi level observations --- stations LS22 in the Labrador See, station NFLD21 on the northeastern the Grand Banks, station SESC2 on Southeast Shoal, and station AVAL3 inside the Avalon Channel [Drozdowski *et al.* 2002]. Multiple observations at the same vertical depths and same stations are overlaid together to highlight the variability of the tidal ellipses. For station LS22 (Figure 5.14), the simulated amplitudes quantitatively agree with the observation for both M_2 and K_1 constituents, but the phases have significant differences. The model can almost reproduce the rectilinear with peak amplitudes of about 5 cm/s for M_2 constituent in station AVAL3 at the 30m depth (Figure 5.15), but the amplitudes of the simulated K_1 constituent is about twice that observed. At station NFLD21, on the northeastern the Grand Banks, where K_1 is stronger

than M_2 constituent, there is good agreement for the K_1 amplitude of about 4 cm/s at 34.7m depth (Figure 5.16), but poor representative of the reduced ellipse size of K_1 constituent with depth. A clockwise rotation and peak amplitudes of over 15 cm/s in station SESC2 on the Southeast Shoal of the Grand Banks is found in both simulated and observed M_2 constituent at different depths (Figure 5.17). The modeled amplitudes are slightly greater than the observed for both M_2 and K_1 constituents. The same observation locations have significantly different tidal currents when observed at different time (Figure 5.14-5.17). Overall, the model is not sensitive enough to represent the observed vertical reduction in ellipse size with depth.

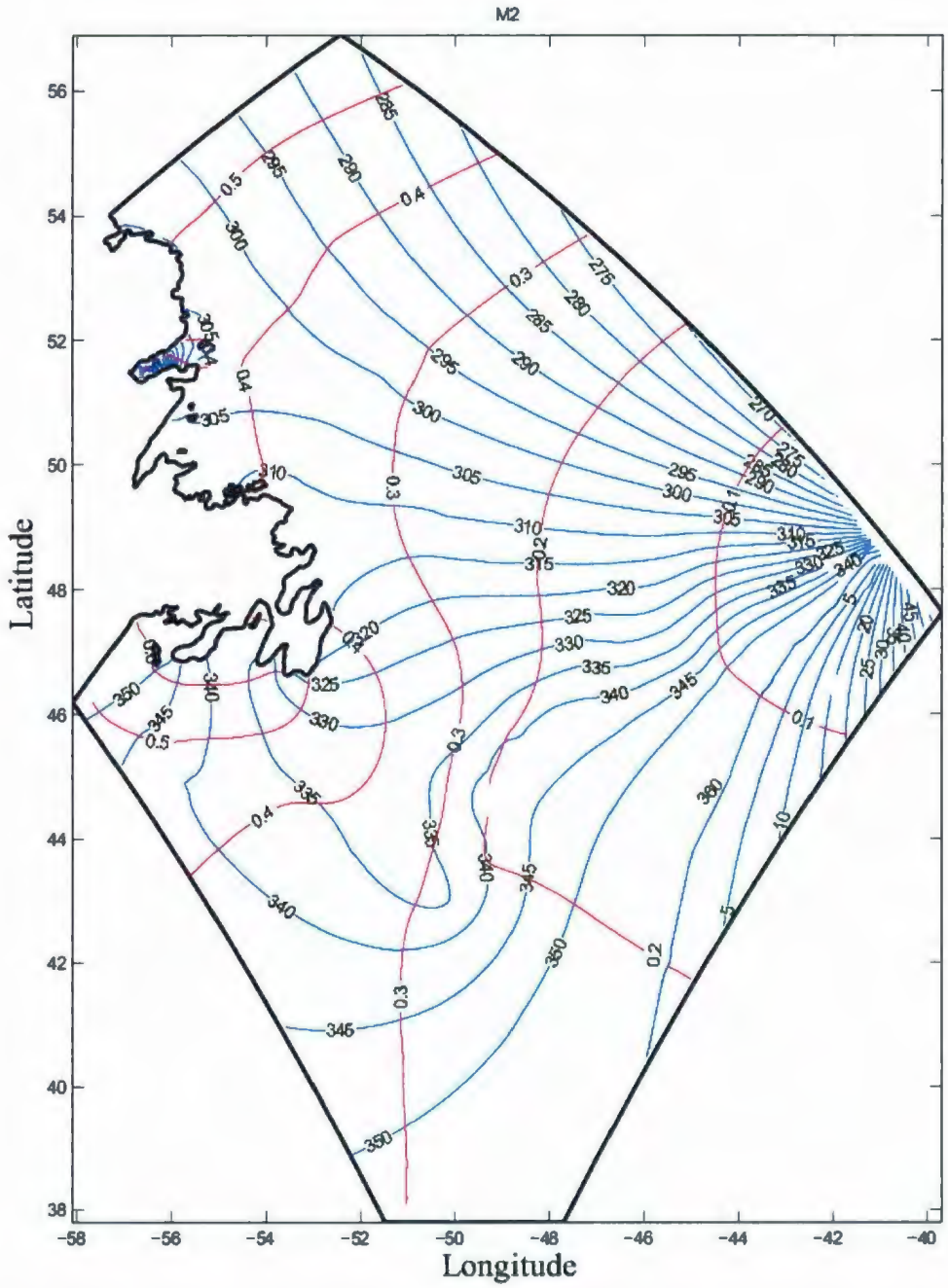

Figure 5.1: Model computed Co-tide charts for M_2 tidal constituent (Blue line: amplitude; Red line: phase). The amplitude is in meters and the phase is in degrees.

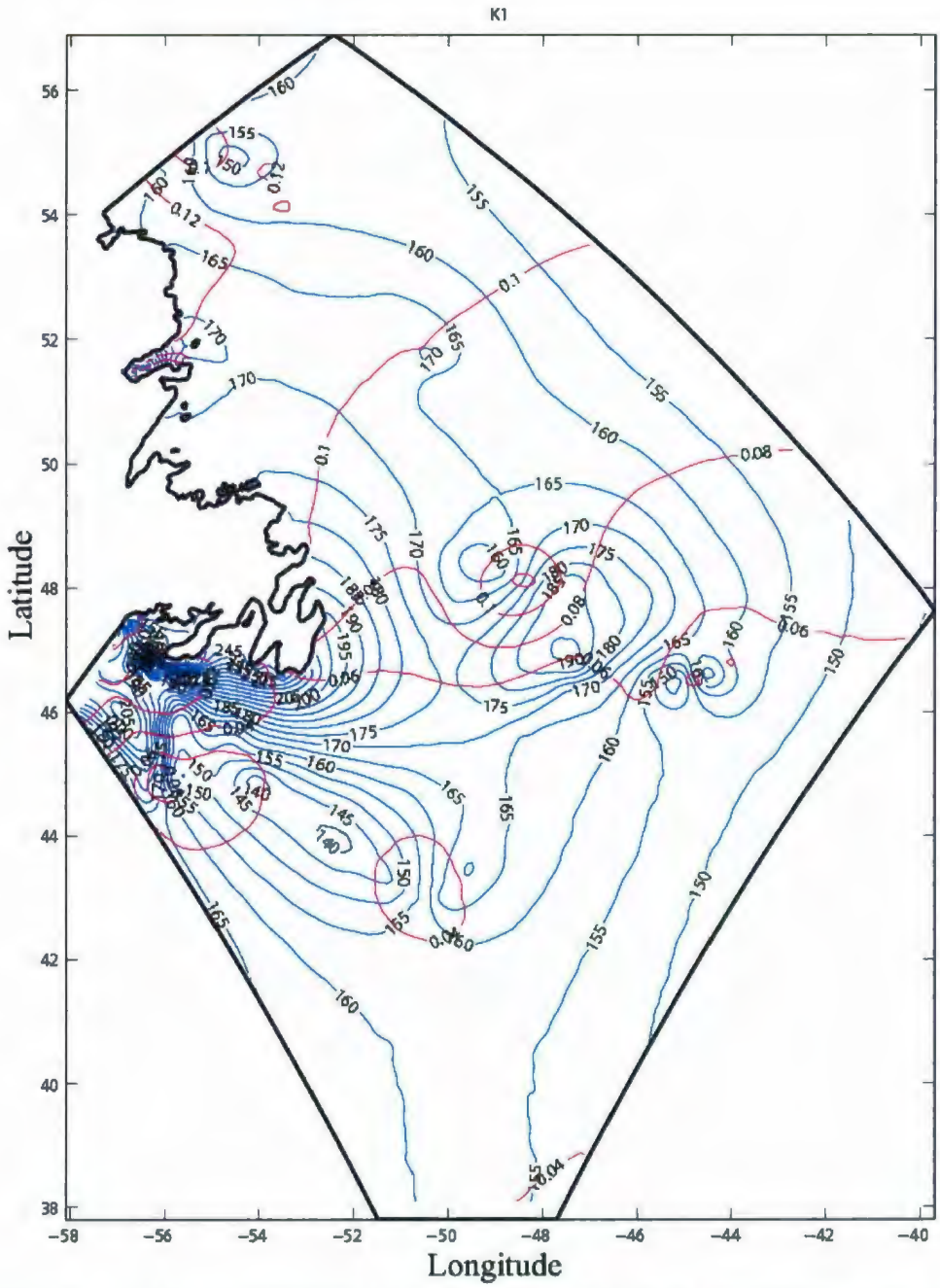

Figure 5.2: Model computed Co-tide charts for K_1 tidal constituent (Blue line: amplitude; Red line: phase). The amplitude is in meters and the phase is in degrees.

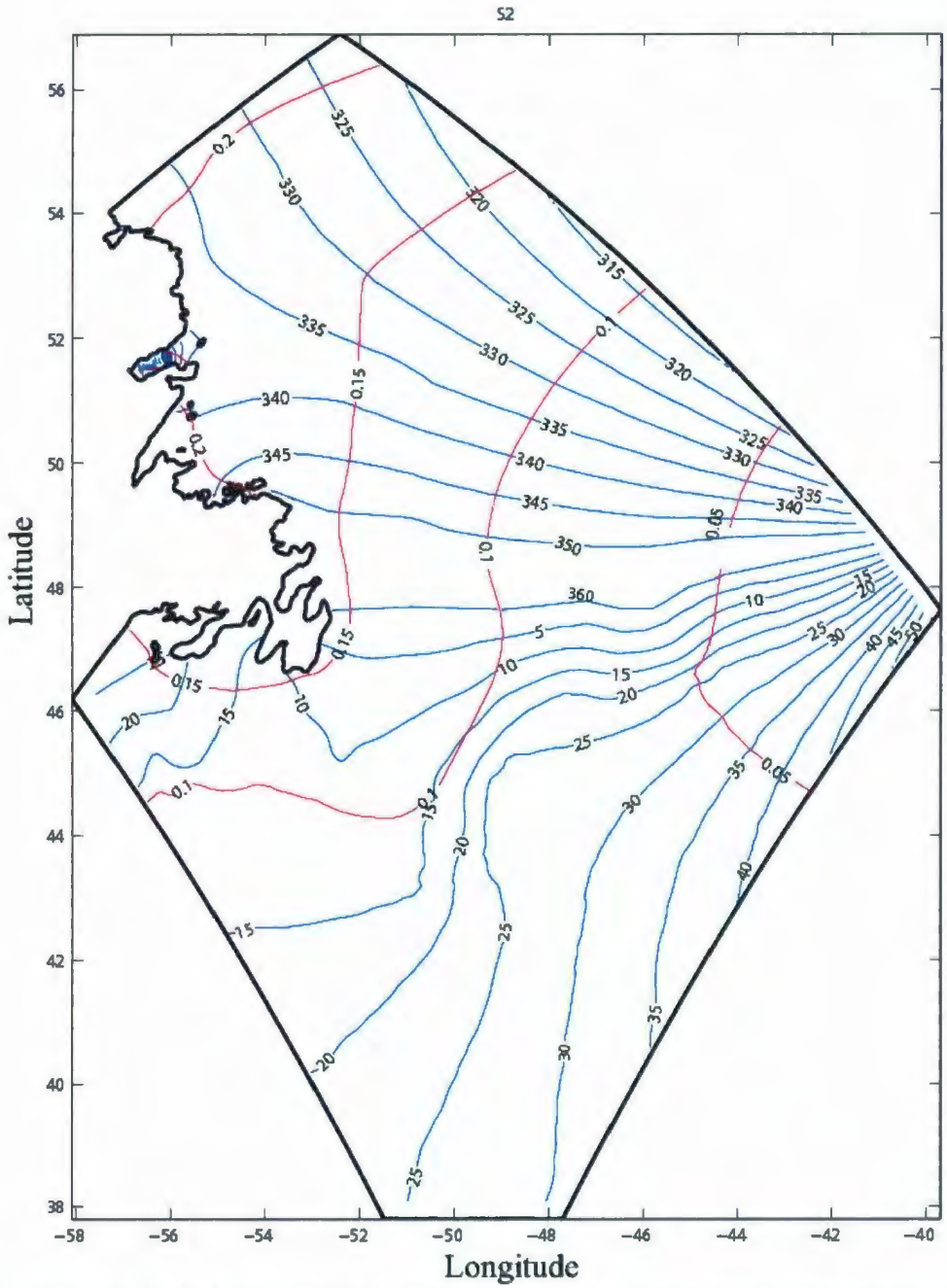

Figure 5.3: Model computed Co-tide charts for S_2 tidal constituent (Blue line: amplitude; Red line: phase). The amplitude is in meters and the phase is in degrees.

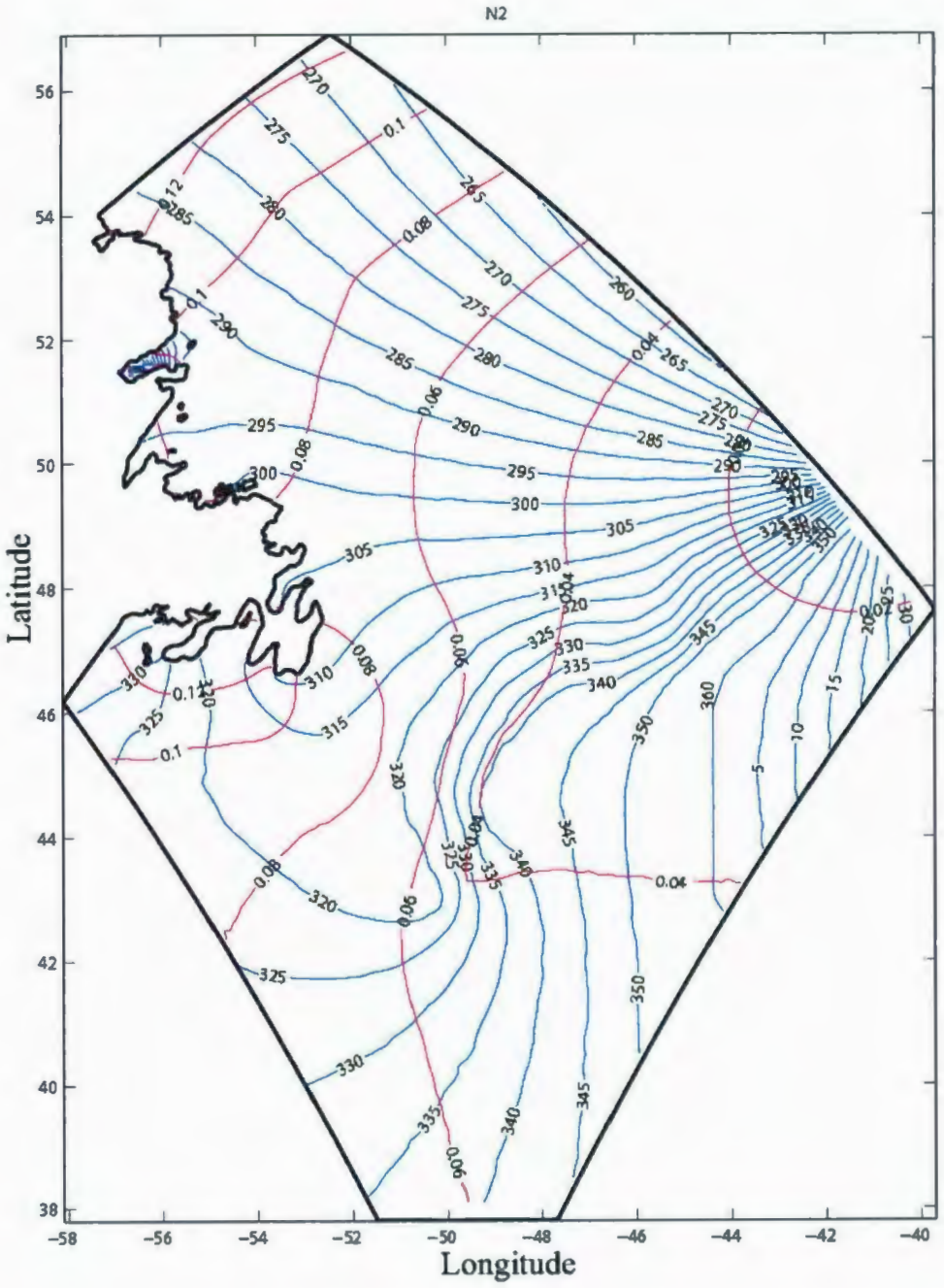

Figure 5.4: Model computed Co-tide charts for N_2 tidal constituent (Blue line: amplitude; Red line: phase). The amplitude is in meters and the phase is in degrees.

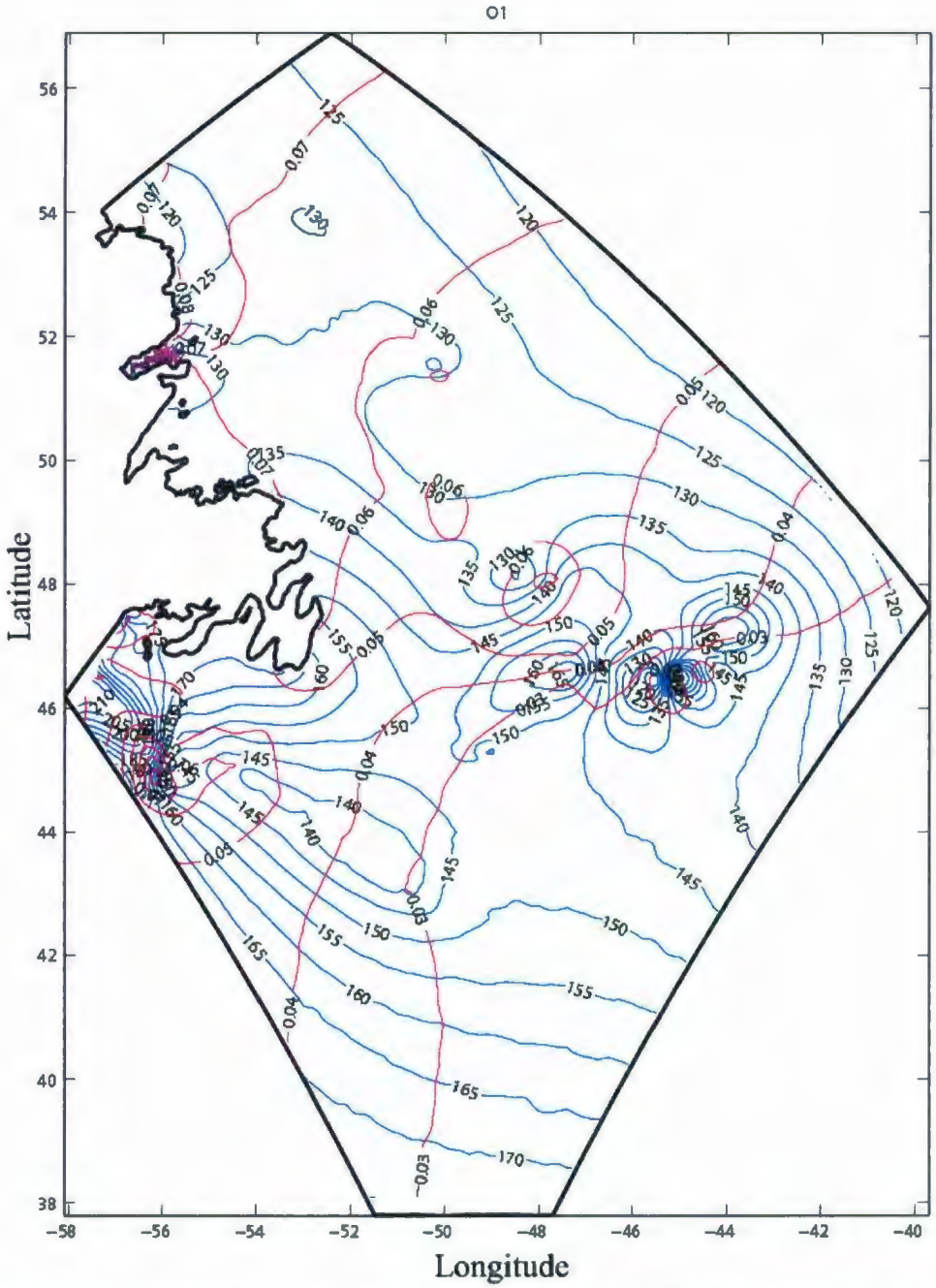

Figure 5.5: Model computed Co-tide charts for O_1 tidal constituent (Blue line: amplitude; Red line: phase). The amplitude is in meters and the phase is in degrees.

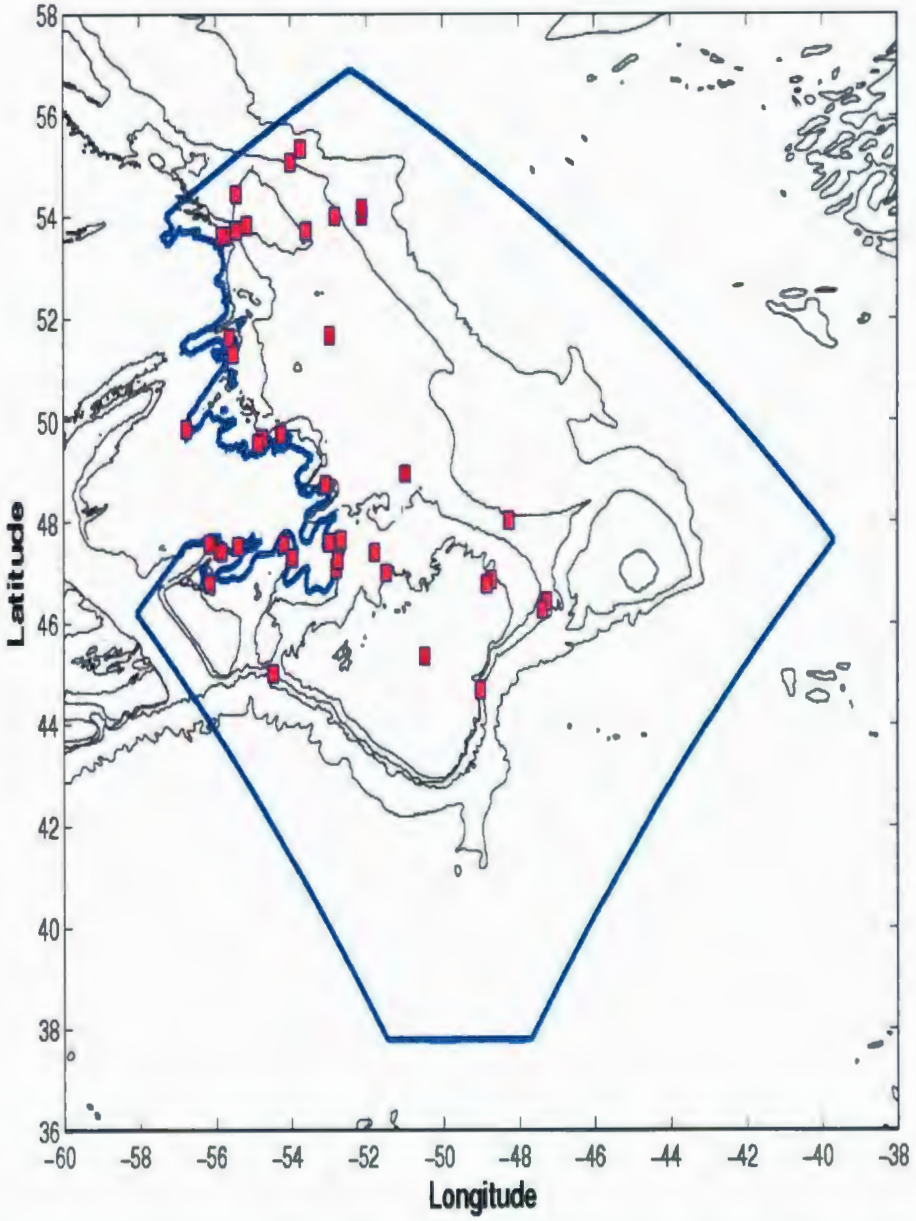

Figure 5.6: Locations of the tide and bottom pressure gauges with isobaths (black lines).

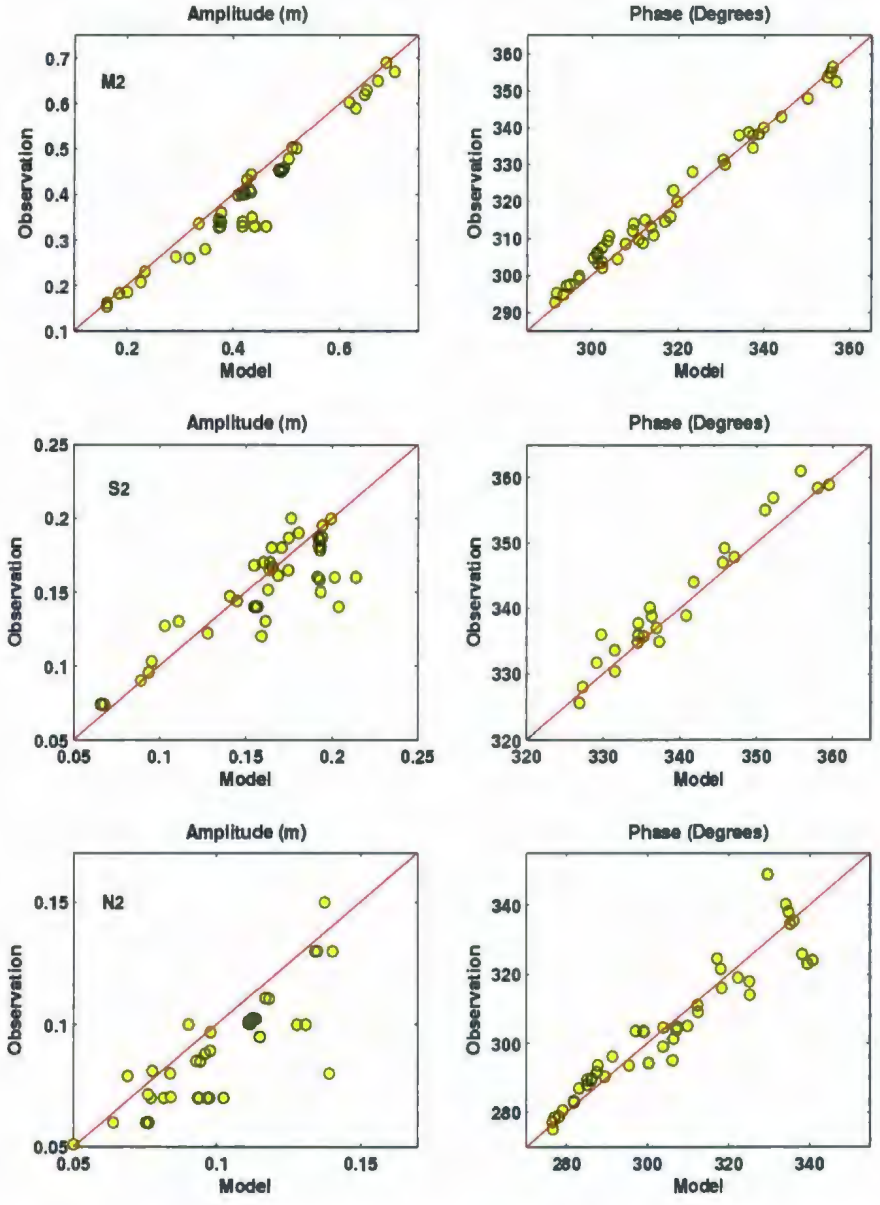

Figure 5.7: Scatter diagrams of amplitudes and phase of the model computed elevation (horizontal) and observation (vertical) for the Semi-diurnal and diurnal constituents. The red solid line along the centre of each graph indicates where scatters should lie when the agreement were perfect. Amplitudes are in centimeters and the phases are in degrees.

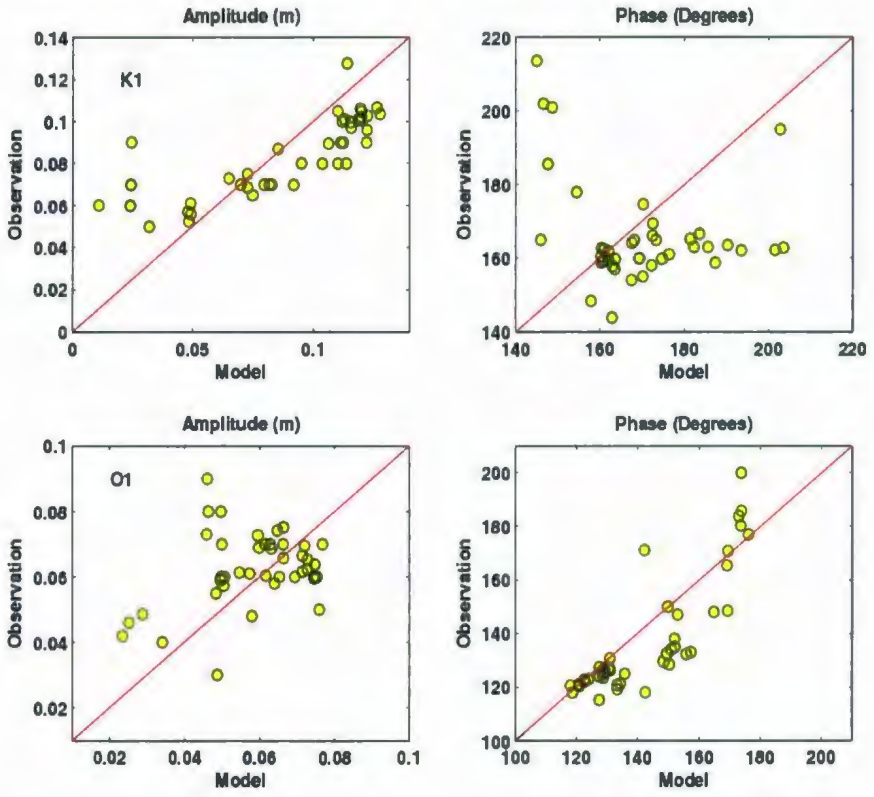

Figure 5.7: Continued.

Table 5.1: Statistics of model simulated elevation for semi-diurnal and diurnal constituents compared with observations at tide and pressure gauge sites.

Constituent	RMS amplitude Difference (cm)	RMS phase Difference	AbsErr (cm)	RelErr (%)
M_2	3.3	2.4	2.9	7.7
S_2	1.5	3.2	1.4	9.6
N_2	1.2	4.8	1.1	14.1
K_1	1.9	18.5	2.2	28.4
O_1	1.2	9.9	1.2	20.7

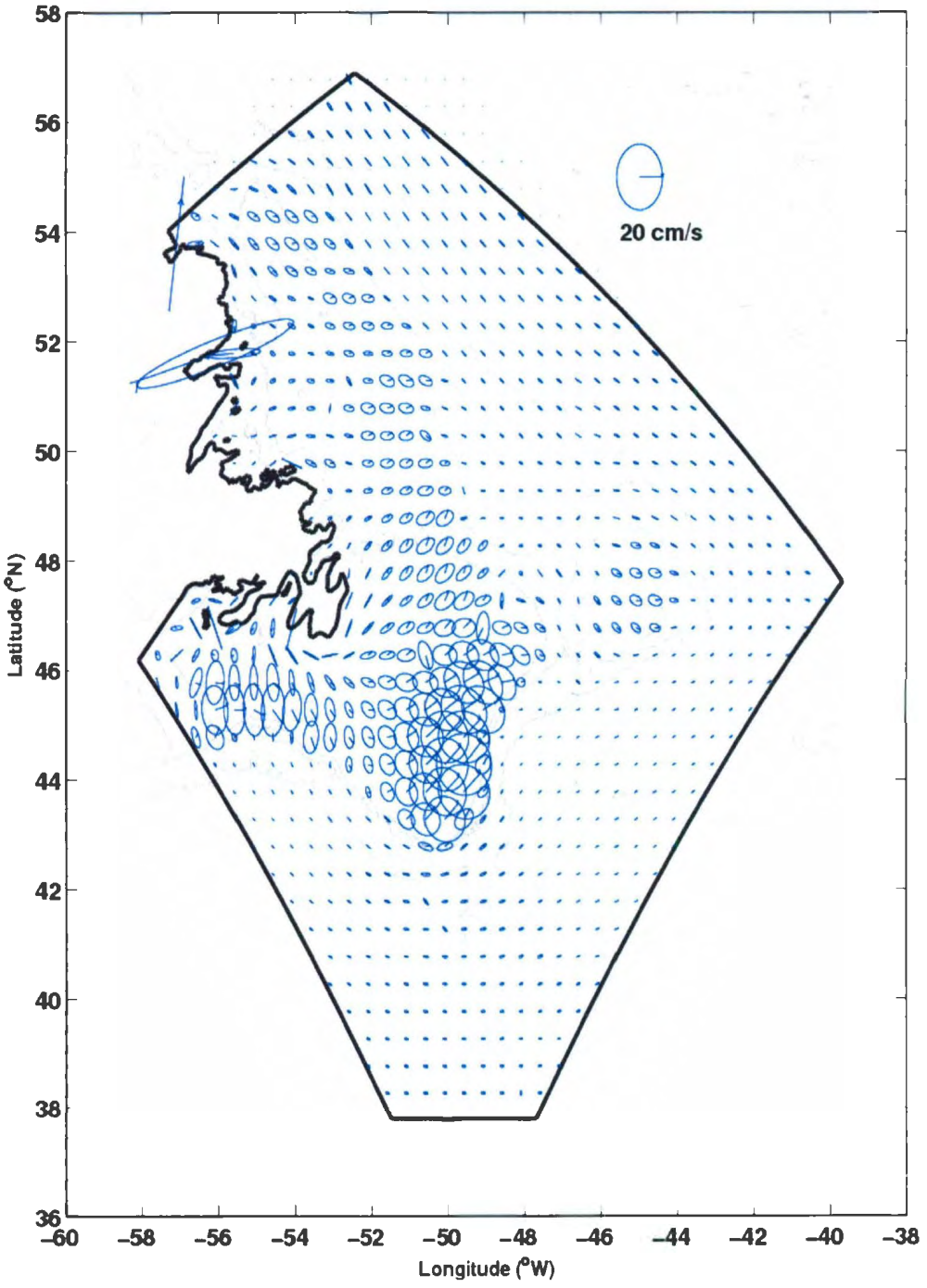

Figure 5.8: Sub-sampled model computed current ellipse M_2 tidal constituent at the surface.

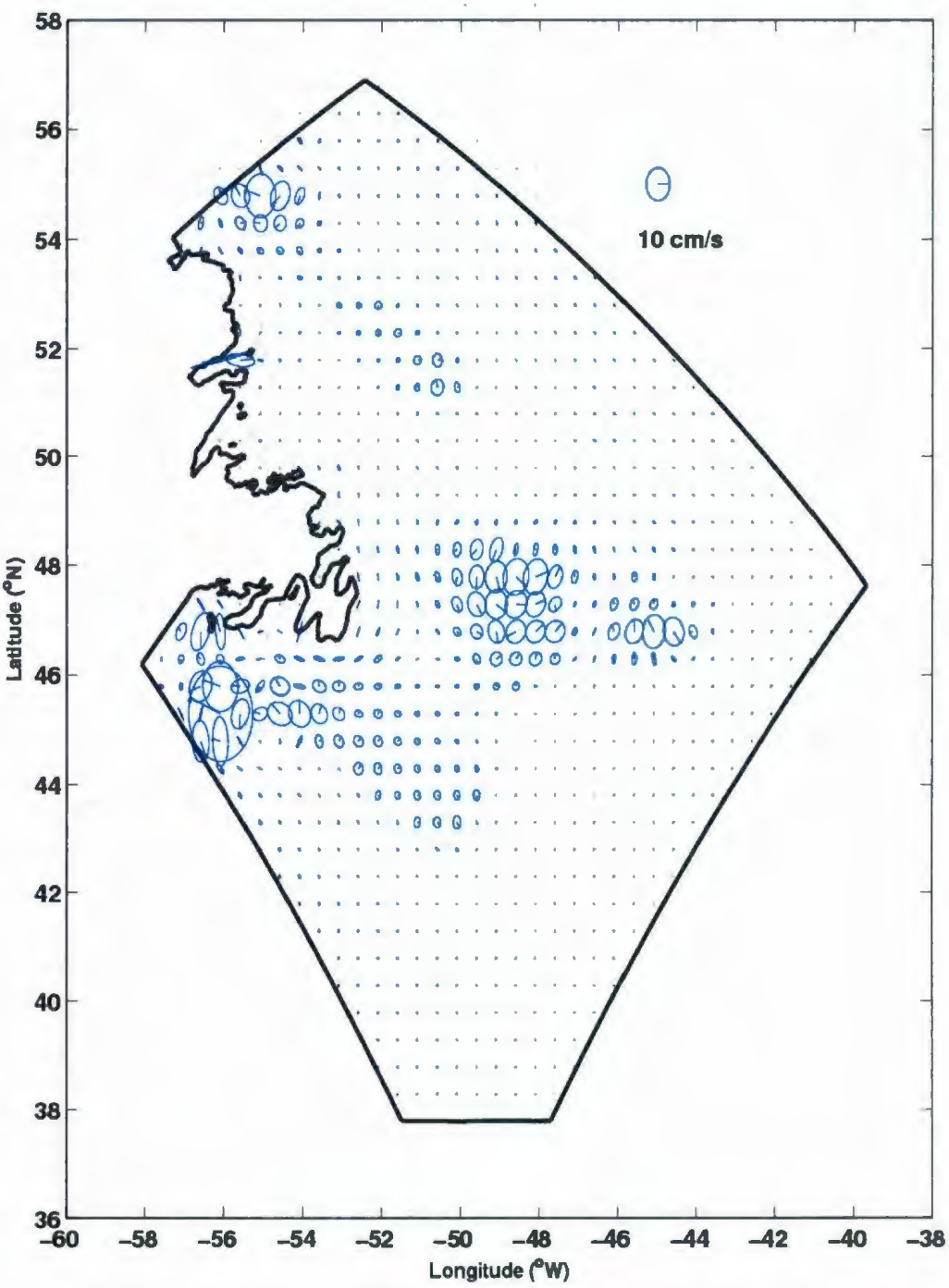

Figure 5.9: Sub-sampled model computed current ellipse K_1 tidal constituent at the surface.

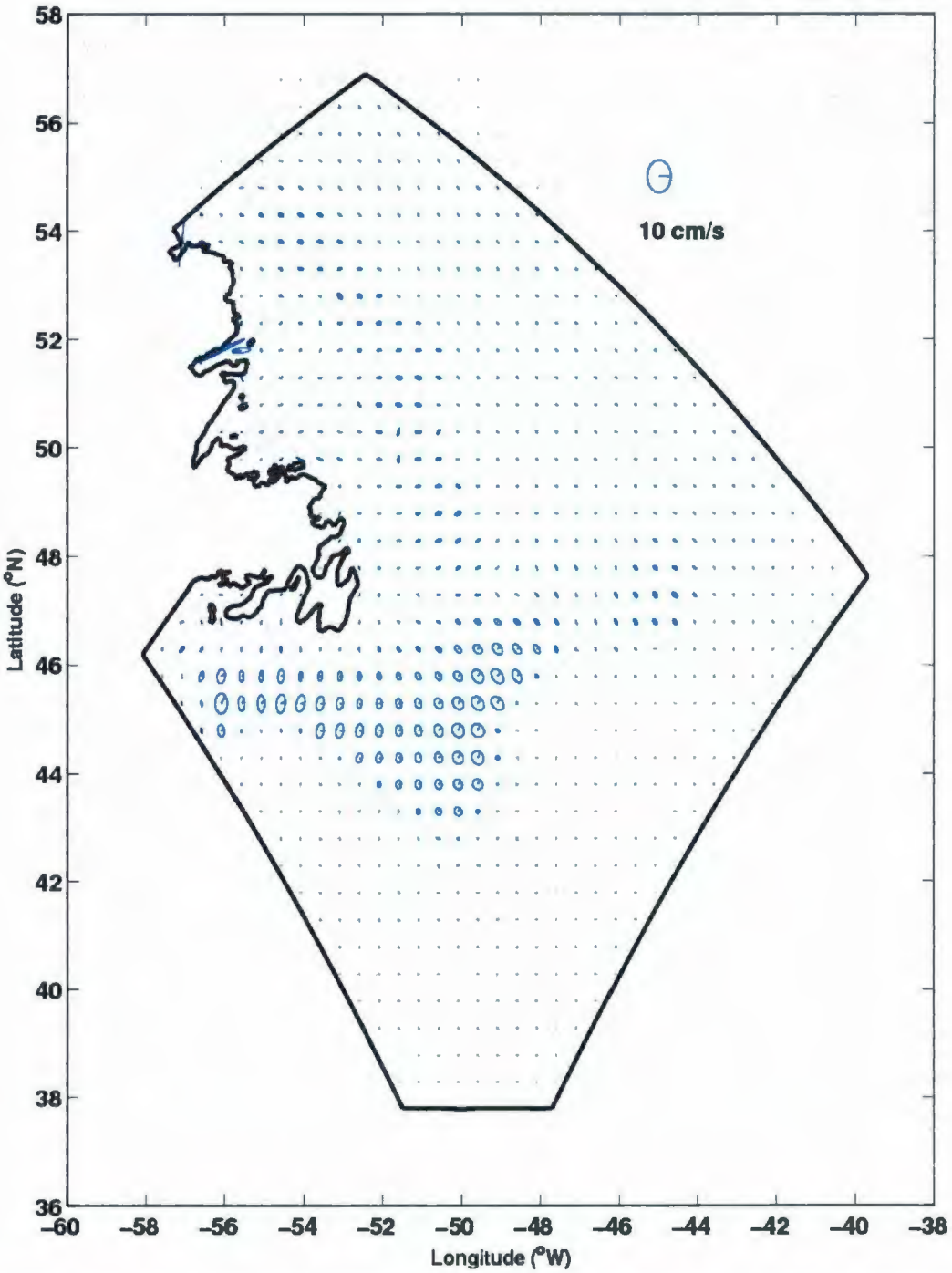

Figure 5.10: Sub-sampled model computed current ellipse S_2 tidal constituent at the surface.

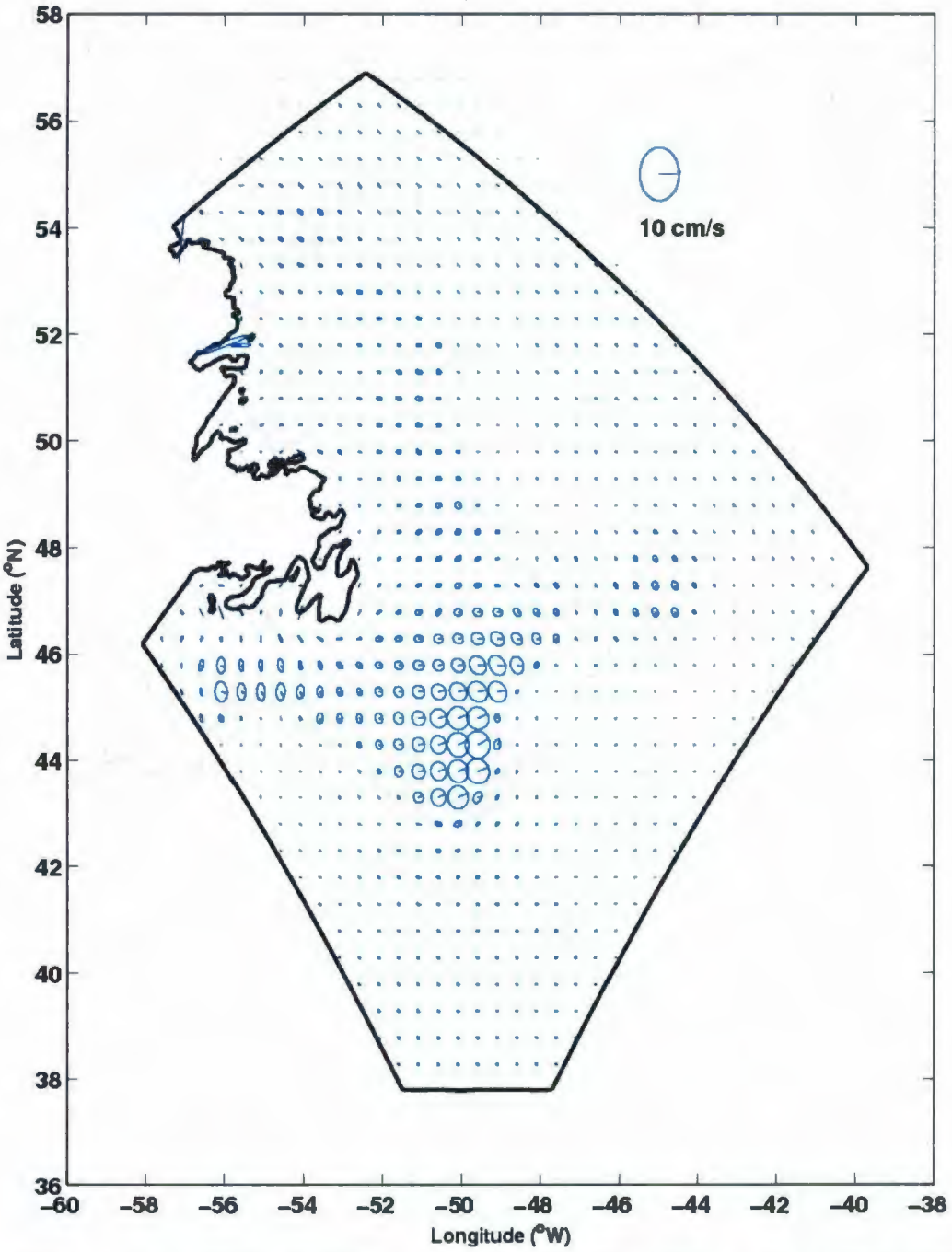

Figure 5.11: Sub-sampled model computed current ellipse N_2 tidal constituent at the surface.

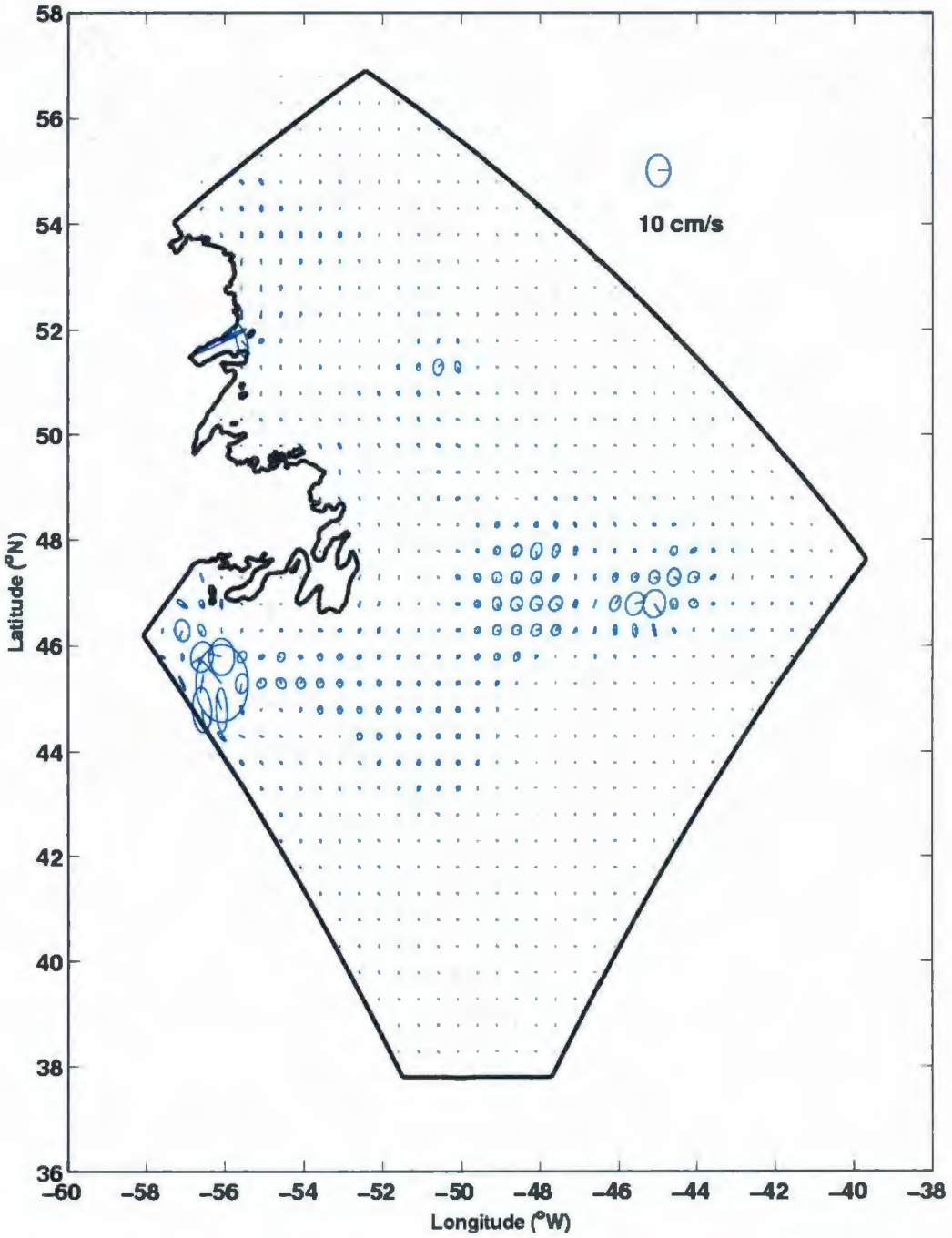

Figure 5.12: Sub-sampled model computed current ellipse O_1 tidal constituent at the surface.

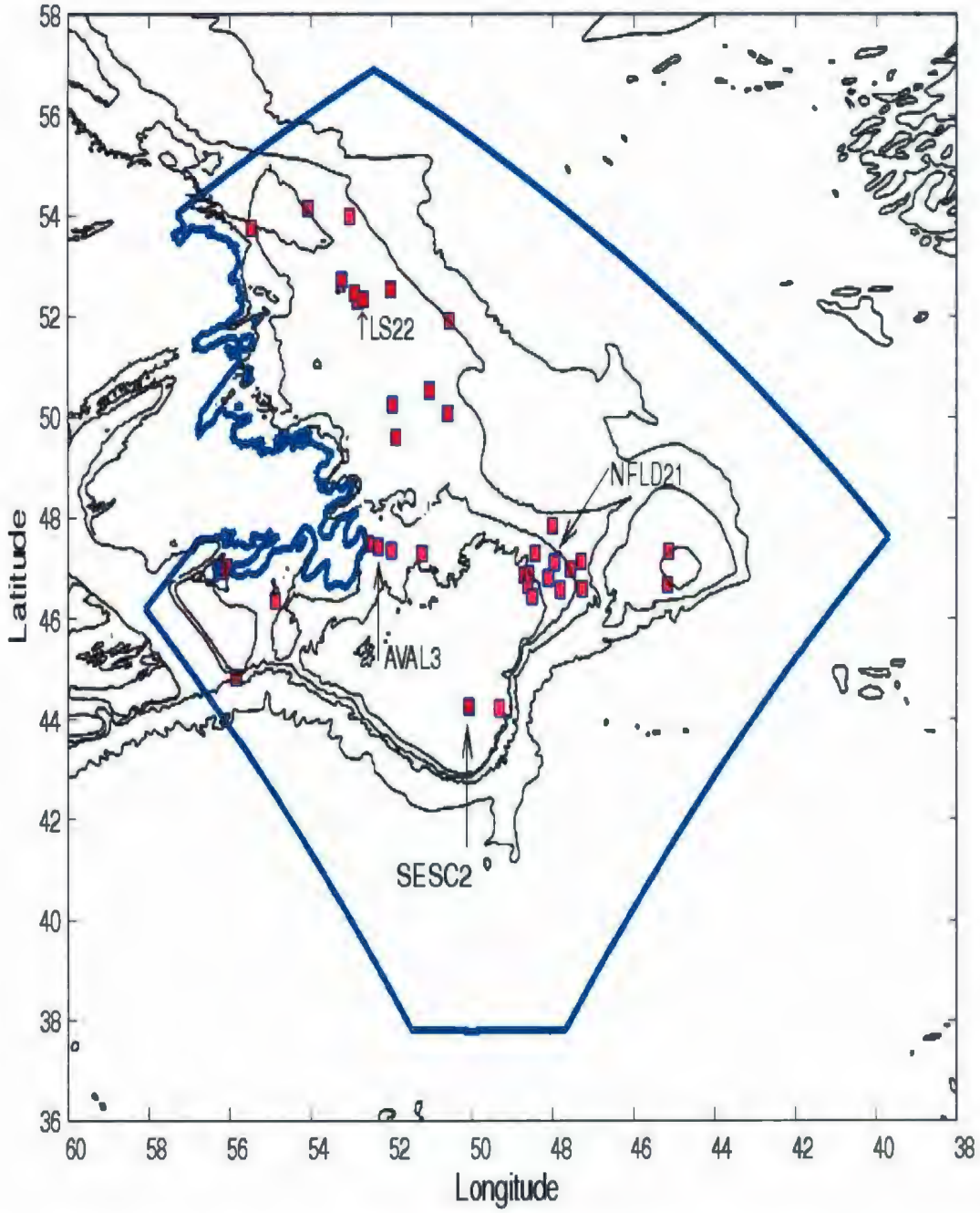

Figure 5.13: Locations of current meter available with isobaths (black lines). The texts inside the figures are the names of locations where the vertical current ellipses structures are examined.

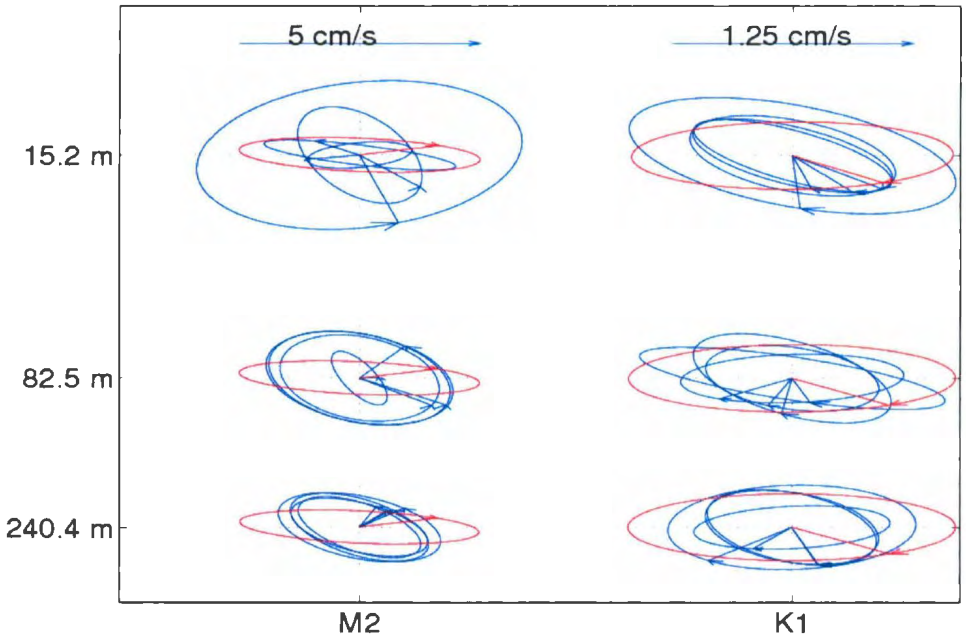

Figure 5.14: Comparison between the observed (blue curves) and modeled ellipses (red curves) for station LS22 in Labrador Sea. The station locations are shown in Figure 5.13.

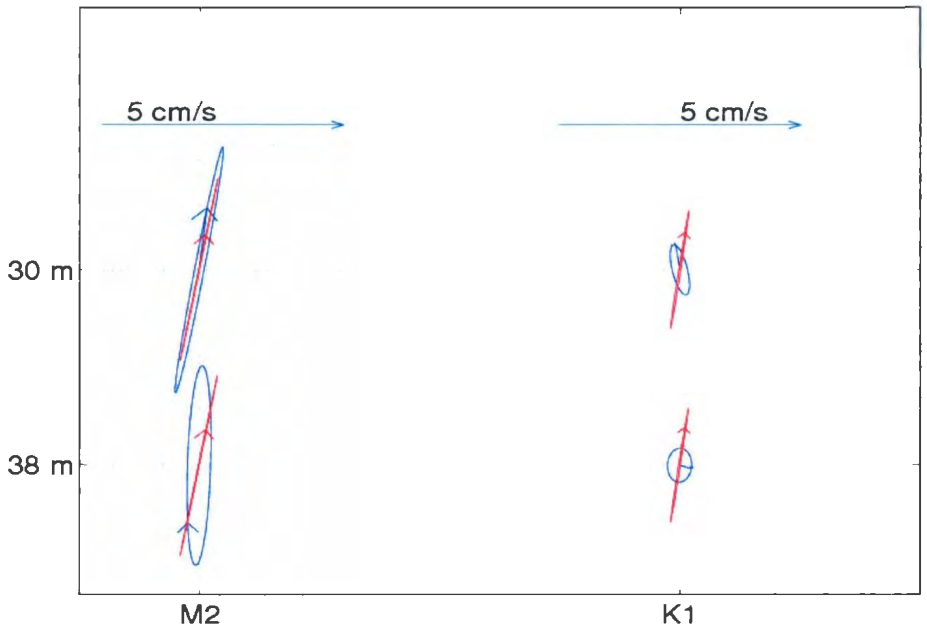

Figure 5.15: Comparison between the observed (blue curves) and modeled ellipses (red curves) for station AVAL3 in Avalon Channel. See Figure 5.13 for station locations.

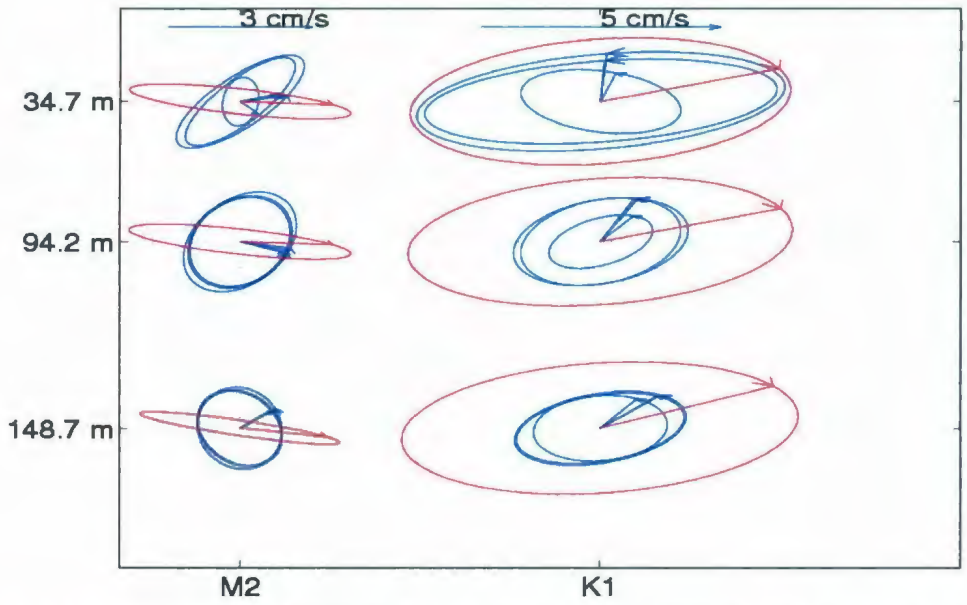

Figure 5.16: Comparison between the observed (blue curves) and modeled ellipses (red curves) for station NFLD21 over Newfoundland Shelf. See Figure 5.13 for station locations.

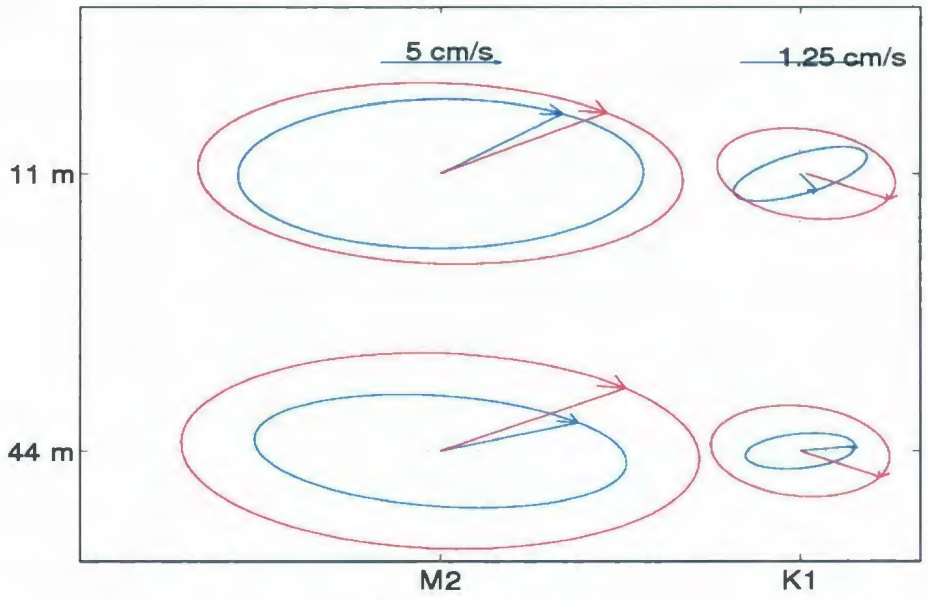

Figure 5.17: Comparison between the observed (blue curves) and modeled ellipses (red curves) for station SESC2 over Southeast Shoal of Grand Banks. See Figure 5.13 for station locations.

Chapter 6

Summary and Conclusions

The objective of this research is to examine effects of different nudging schemes on circulation, temperature and salinity solutions of a three-dimensional finite element model over the Newfoundland and Labrador Shelf. We take two different approaches in this study. One approach is to restore the model temperature and salinity toward their initial values (for the first M_2 cycle) or toward evolving immediately preceding M_2 cycle mean values (for the second and subsequent M2 cycle). The other approach is to fix the density but allow dynamical evolution of temperature and salinity.

From the simulated circulation field, the dominant main branch of the Labrador Current flows equatorward along the shelf edge and the relative weak inshore branch of the Labrador Current flows along the Labrador and Newfoundland coasts. Significant seasonal variations of the circulation can be found in the present simulated circulation results as well. For both the main branch and the inshore branch, the Labrador Current is strong in the fall/winter and weak in the spring/summer.

The current comparison statistics indicate good qualitative agreement and approximate quantitative agreement with moored measurements. The modeled sea level at

St. John's agrees well with tide gauge observations.

Comparison of the two different schemes shows that the nudging T/S approach is conceptually and dynamically more realistic than the pure diagnostic one. Besides allowing local dynamical adjustment within the tidal timescale, the nudging scheme can also effectively prevent the unrealistic model drift. The use of the variable Coriolis parameter eliminates the unrealistic inertial oscillation which otherwise occurred in the solutions with the constant Coriolis parameter, and slightly improves the model agreement with observations.

Tidal analysis results of the run forced by five leading semidiurnal and diurnal tidal constituents on the open boundary are consistent with previous studies in general. Overall, the model agrees well with the observed tidal elevation, but the comparison of the model and observed current ellipses show considerable discrepancies in places. The model shows that the semidiurnal constituents are significantly stronger than the diurnal constituents.

Bibliography

Blumberg, A. F., and B. Galperin (1992), Modeling vertical structure of open-channel flows, *J. Hydraul. Eng*, *118*, 1119 - 1134.

Colboume, E. B., et al. (1997), A Comparison of hydrography and circulation on the Newfoundland Shelf during 1990-1993 to the long term mean, *Can. J. Fish. Aqut. Sci*, *54 (Suppl. 1)*.

Crawford, W. R., and R. E. Thomson (1982), Continental shelf waves of diurnal period along Vancouver Island, *Journal of Geophysical Research*, *87*, 9516-9522.

Drozdowski, A., et al. (2002), The Northwest Atlantic Tidal Current Database, 222: v+235pp .

DuPont, F., et al. (2002), Modeling system for tides, 221: vii +272 pp.

Egbert, G. D., et al. (1994), TOPEX/Poseideon tides estimated using a globe inverse model, *Journal of Geophysical Research.*, *99*, 24 821-824 852.

Gill, A. E., and P. P. Niiler (1973), The theory of the seasonal variability in the ocean, *Deep-Sea Res*, *20*, 141- 177.

Godin, G. (1980), Cotidal chadts for Canada, 55, 93pp , Dept. Fish. And Oceans, Ottawa, Ontario, Canada.

Greatbach, R. J., and A. Goulding (1989), Seasonal variations in a linear barotropic model of the North Atlantic driven by the Hellerman and Rosenstein wind stress field, *Journal of Geophysical Research*, *94*, 572-595.

Greenberg (2004), The semi-prognostic method, *Continental Shelf Research*, 2149-2165.

Greenberg, D. A., and B. D. Petrie (1988), The mean barotropic circulation on the Newfoundland Shelf and Slope, *Journal of Geophysical Research*, *93*, 15541-15550.

Greenberg, D. A., et al. (1998), A diagnostic finite element ocean circulation model in spherical-polar coordinates, *Journal of Atmospheric and Oceanic Technology 15*, 942-958.

Gregory, D. N., and C. Bussard (1996), Current statistics for the Scotian Shelf and Slope, 144, 167 pp. Ocean Sci. Div. of Fish. and Ocean Can., Dartmouth, N. S. Canada.

Han, G. (1995), *Coastal tides and shelf circulation by altimeter*, chap. 4. pp. 45-55, CRC Press, Boca Raton, Fla.

Han, G. (2000), Three-dimensional modeling of tidal currents and mixing quantities over the Newfoundland Shelf, *Journal of Geophysical Research*, *102*, 1011-1025.

Han, G. (2005), Wind-driven barotropic circulation off Newfoundland and Labrador, *Cont. Shelf Res*, *25*, 2084 - 2106.

Han, G., et al. (1993), Annual variation of sea-surface slopes over the Scotian Shelf and Grand Banks form Geosat altimetry, *Atmos. Ocean*, *31*, 591-615.

Han, G., et al. (1996), Oceanic tides over the Newfoundland and Scotian Shelves from Topex/POSEIDON altimetry, *Atmos-Ocean*, *34*, 586-604.

Han, G., et al. (2008), Seasonal variability of the Labrador Current and shelf circulation off Newfoundland, *Journal of Geophysical Research, 113*.
Han, G., and C. L. Tang (1999), Velocity and transport of the Labrador Current determined from altimetric, hydrographic, and wind data, *Journal of Geophysical Research, 104*.
Heywood, K. J., et al. (1994), Eddy kinetic energy of the North Atlantic subpolar gyre from satellite altimetry, *Journal of Geophysical Research, 99*, 22525-22539.
Huthnance, J. M., et al. (1986), *Coastal trapped waves, in Baroclinic Processes on Continental Shelves*, 1-18 pp., AGU, Washington, D. C., 1986.
Kinnmark (1986), *The shallow water equations: Formulation, analysis and application*, 187 pp., Springer-Verlag, Berlin.
Lazier, J. R. N., and D. G. Wright (1993), Annual Velacity variations in the Labrador Current, *Journal of Physical Oceanography, 23*, 659-678.
Loder, J. W., et al. (Eds.) (1998), *The coastal ocean off northeastern North America: A large-scale view, in The Global Coastal Ocean*, 105-133 pp., John Wiley, Hoboken, N. J.
Lynch, D. R., and F. E. Werner (1991), Three-dimensional hydrodynamics on finite elements. Part II: Non-linear time- stepping model, *Int. J. Numer. Methods Fluids, 12*, 507-533.
Lynch, D. R. J. T. C. I., et al. (1996), Comprehensive coastal ciculation model with application to the Gulf of Maine, *Continental Shelf Res, 16*, 875-906.
Mathieu, T., and B. deYoung (1995), Application of a mixed layer model to the inner Newfoundland shelf, *Journal of Geophysical Research, 100*, 921-993.
Mellor, G. L., and T. Yamada (1982), Development of a turbulence closure model for geophysical fluid problems, *Rev. Geophys, 20*, 851-875.
Narayanan, S., et al. (1996), Current meter observations from the Labrador and Newfoundland Shelves and comparisons with barotrophic model predictions and BP surface currents, *Atmosphere-Ocean, 34 (1)* 227-255.
NGDC (1988), Digital relief of the Surface of the Earth. Data Announcement 88-MGG-02, Boulder, Colorado.
Petrie, B., and C. Anderson (1983), Circulation on the Newfoundland continental shelf, *Atmos.Ocean, 21*, 207-226.
Petrie, B., and J. Buckley (1996), Volume and freshwater transport of the Labrador Current in Flemish Pass, *Journal of Geophysical Research.*
Petrie, B., et al. (1987), Tides on the Newfoundland Grand Banks, *Atmosphere-Ocean, 25*, 10-21.
Proctor, R., and A. M. Davies (1996), A three dimensional model of tides off the north-west coast of Scotland, *J. Mari. Syst, 7*, 43-66.
Reynaud, T. H., et al. (1995), Summer mean circulation of the Northwestern Atlantic Ocean, *Journal of Geophysical Research, 100*, 779-816.
Schwiderski, E. W. (1980), On charting globe ocean tides, *Rev. of Grophys, 18*, 243-268.
Sheng, J., and K. R. Thompson (1996), Summer surface circulation on the Newfoundland Shelf and Grand Banks: The roles local density gradients and remote forcing, *Atmosphere-*

Ocean, *34 (2)*, 267-284.
Smagorinsky (1963), General circulation experiments with the primitive equations, I: the basic experiment, *Monthly Weather Review*, *91*, 99-164.
Smith, E. H., et al. (1937), The Marion and General Green expeditions to Davis Strait and the Labrador Sea, *Bull. U.S. Coast Guard*, *19*, 259.
Smith, S. R., et al. (2001), Quantifying uncertainties in NCEP reanalyses using high quality research vessel observations, *Journal of Climate*, *14*, 4062-4072.
Tang, C. L. (1996), Modeling the mean Circulation of the Labrador Sea and the Adjacent Shelves, *Journal of Physical Oceanography*, *26*, 1989-2010.
Thompson, K. R., et al. (1986), Wind-forced changes in Labrador Current transport, *Journal of Geophysical Research*, *91*, 14261-14268.
UNESCO (1981), Tenth report of the joint panel on oceanographic tables and standards.
Wright, D. G., et al. (1988), Moored current and pressure data from the Labrador/Newfoundland Shelf. Tech. rep, P.O box 1006, Dartmouth, NS, Canada, B2Y-4A2.
Z.Xu, and J. W. Loder (2004), Data assimilation and horizontal structure of the barotropic diurnal tides on the Newfoundland and Southern Labrador Shelves, *Atmosphere-Ocean*, *42*, 43-60.